2014

Analysis And Design Of Low Profile Multiband Multifunctional Antenna Arrays

Walker F. Hunsicker
University of Mississippi

ANALYSIS AND DESIGN OF LOW PROFILE MULTIBAND MULTIFUNCTIONAL ANTENNA ARRAYS

A Thesis submitted in partial fulfillment of the
requirements for the degree of Doctor of Philosophy
in Engineering Science
The University of Mississippi

by

WALKER F. HUNSICKER

May 2015

ABSTRACT

Light-weight phased array antennas for aerospace and mobile applications require utilizing the same antenna aperture to provide multiple functions with dissimilar radiation pattern specifications (e.g., multiband operation for communications and tracking). Multi-functional antennas provide advantages over aggregate *antenna clusters* by reducing space requirements, and can aid in the optimal placement of all required apertures to provide adequate isolation between channels. Furthermore, the combination of antenna apertures into a common geometry mitigates co-site installation issues by addressing interference within the integrated radiator design itself as opposed to the extensive analysis which is required to configure multiple radiators in close proximity. The combination of multiple radiators into a single aperture can only be achieved with the proper selection of antenna topology and accompanying feed network design. This research proposes a new technique for the design of multiband arrays in which a common aperture is used. Highlighted by this method is the integration of a tri-band array comprised of an X-band (12 GHz) microstrip patch array on a superstrate above printed dual-band (1 and 2 GHz) slot loop antenna arrays in an octave-spaced lattice. The selection of a ground backing reflector is considered for improved gain and system packaging, but restricts the utility of the design principally due to the $\lambda/4$ depth of the ground plane. Therefore, a novel multiband high impedance surfaces (HIS) is proposed to load the slot apertures for reduced height. The novel techniques proposed here will enable the design of a low profile and conformal single aperture supporting multi-band and multi-functional operations.

LIST OF ABBREVIATIONS AND SYMBOLS

a	Period of the unit cell
Al	Periodic table symbol for the element aluminum
AMC	Artificial magnetic conductor
AUT	Antenna under test
C	Capacitance
Co-Pol	Copolarized Field
E	Electric field
EBG	Electronic band-gap
F/B	Front to back Ratio
g	Gap between patches
GSM	Global system for mobile communications
h	Height of antenna stackup
H	Magnetic field
HIS	High impedance surface
IDC	Interdigitated capacitance
l	Length of slot
L	Inductance
M	Magnetic source
MS	Microstrip

PBC	Periodic boundary condition
PCB	Printed circuit board
PCS	Personal communications service
PEC	Perfect electric conductor
Radar	Radio detection and ranging
RF	Radio frequency
t	Thickness of dielectric board
TE	Transverse electric
TM	Transverse magnetic
UWB	Ultra-wideband
w	Width of patch
X-pol	Cross polarized field
Z	Impedance
Γ, X, and M	Transition points on dispersion diagram
β	Wavenumber
ε	Permittivity
μ	Permeability
ω	Angular frequency

ACKNOWLEDGMENTS

I express my deepest appreciation to my advisor, Dr. Atef Z. Elsherbeni and my committee members, Drs. Ramanarayanan Viswanathan, Laura Sheppardson, and Mustafa Matalgah. I would also like to thank Mr. Roger Hasse of Georgia Institute of Technology and Mr. Rory Grondin of LPKF for their assistance in fabrication and measurement of the low band EBG designs.

TABLE OF CONTENTS

LIST OF FIGURES

CHAPTER 1

INTRODUCTION

1.1 Background and Previous Related Research

In aerospace and wireless communications, there is a pressing need to minimize the size, weight and power requirements of antenna arrays, while simultaneously requiring multiple radiation functions using the same physical aperture. For example, the array may require shared aperture capability to facilitate full-duplex operation with polarization diversity, and multiple isolated frequency bands for communications, telemetry, Radar, etc. One approach for designing multi-band array antennas is to use a single wideband radiating aperture and process the received signals with an integrated front-end comprised of wideband power dividers and feeds to the elements. Thus, ultra-wideband (UWB) antenna elements have been designed and fabricated that can potentially provide a shared aperture capability [1-3]. However, these antennas require expensive, heavy, and bulky front-ends to channelize the signals into multiple frequency bands required for communications and radar signal processing, where narrow bandwidths are typically allocated for each function. The associated complexity of receiver design escalates considerably if UWB operation is required in an array configuration.

The concept of array antennas with widely separated frequency bands (e.g. PCS, GSM communications bands, L and S radar bands) which share the same physical aperture, is a challenging problem, and has been largely unexplored. A novel design of dual-band, dual-

linearly polarized microstrip antenna arrays for synthetic aperture Radar applications, with a frequency ratio of about 1:3, has been presented in [4], utilizing stacked microstrip dipoles and square patches as the radiating elements at S- and X-bands, respectively. Another novel antenna element design for dual-band *shared-aperture* array configuration uses interleaved printed dipoles with balanced individual feeds for each band [5]. The folded dipoles are resonant at octave-separated frequency bands, and printed on photographic paper using low-cost photolithography and ink-jet printing technology. This work was extended to the design of a dual-band printed slot array consisting of isolated square slot loops covering each band. Each slot element is fed through coupling to a microstrip line on the other side of the slot substrate, as described in [6]. The integration of a X-band patch array and beamformer conforming to the specific topology allowed by the lower frequency elements to create a single *multi-band, multi-functional aperture* was proposed in [7].

1.2 Major Challenges

1.2.1 Integrated Multiband Arrays with a Common Aperture

The techniques for the integration of three antenna arrays into a basic unit structures is proposed. Contrasting printed and slot antenna technologies, a method will be proposed to enable the use of a shared ground structure for the integration of multiple antenna types. Through a combination of topology assessment, material parameters, and novel feed design approach, a new multiband design technique is contributed.

1.2.2 Low Frequency EBG Ground Plane for Slot Antennas

The introduction of the artificial magnetic surface in [8,9] can reduce the profile of reflector backed antennas [10]. However, the design of these surfaces for low frequency applications is a complex process due to material properties, bandwidth reduction, and the large size of the periodic cells relative to the antenna dimensions. To achieve bulk magnetic characteristics the size of the unit cell in proportion to resonant wavelength must be small. Further complexities arise in the need to populate full surfaces with all the geometric intricacies for full wave analysis. However, the benefit from such implementation is size reduction of the aperture for potential conformal applications. The multiband system proposed here will use an artificial magnetic conductor (AMC) ground plane developed in this research to operate in two different bands with one octave of separation as a contribution to shared aperture antenna technologies.

1.3 Summary of Proposed Research

The goal of this research is to provide the necessary techniques for the integration of multi-band multi-functional antenna array systems through the selection of antenna topologies to provide a single common aperture. Chapter 2 will focus on the topology of the antenna and how partitioning of the aperture can provide multiband capacity. Chapter 3 describes the radiation mechanism of the slot loop antenna and how it is functionally used in the design. Chapter 4 will develop the low band high impedance surface needed to reduce the antenna thickness and demonstrate the capability to operate at two resonances. Chapter 5 will present the high frequency array that is superficially installed on the loop antennas and the analysis of measured performance.

CHAPTER 2

MULTIBAND MULTIFUNCTIONAL ANTENNA DESIGN

2.1 Practical Limitations of Antenna Installation

For antenna installations where volume and area are limited, special techniques are required to achieve both multiband and multifunction operations. One such concept is a *shared aperture* in which a common surface is partitioned to support multiple antenna types and modalities. The first condition is the geometry of the aperture must accommodate the lattice structure of each array such that none of the node positions of adjacent arrays will intersect with antennas of the neighboring band. The second consideration is enforcing geometric symmetry throughout the partition comprised by the unit cell of greatest size. Such a condition allows the concatenation of sub-array panels to produce the complete antenna. Commonly, antennas are located on the exposed exterior surface of a vehicle or device that is metallic, plastic, or of some form of composite material. Future discussion will assume some form of metallic ground plane is available for practical implementation. Given a metallic surface and functional antenna need, the challenge would be the selection or design of the optimal topology of the array elements to provide the desired performance. Furthermore, these elements should be arranged such that grating lobes and other undesirable effects from sparsely populated elements are avoided. The common approach to the given design paradigm is to select an array element capable of

supporting all the necessary frequencies of operation using wideband radiators. The complexity of the array integration becomes packaging the element with the requirement to conform to λ/2 spacing at the highest frequency of interest. At this spacing the wavelength corresponds to the minimum physical separation so element overlap is of great concern. Finally, with a fully populated array the issue of mutual coupling is significant which can lead to poor scanning performance.

2.2 Multiband Aperture Design Approach

The concept of array antennas with widely separated frequency bands (e.g. PCS, GSM communications bands, L, S, and X radar bands) which share the same physical aperture, is a challenging problem, and has been largely unexplored. The intent of this research is to provide design guidance on the implementation of the high frequency array within the space constraints imposed by the low frequency sub-arrays, while simultaneously satisfying the periodicity required for grating lobe-free operation. In this design paradigm, the high frequency element must conform to a specific topology allowed by the lower frequency elements. Therefore, the shape, orientation, and dimensions of the low frequency elements will ultimately influence the possible design frequency of the high frequency array, due to the requirement of λ/2 free space grid spacing on the latter array to avoid grating lobes.

2.3 Geometry of the Unit Cell

The overall goal is to design a multifunctional antenna array with dual-band printed slot antenna arrays for the two lower most frequencies along with an integrated high frequency array with its own planar beamformer on the same physical aperture. The selection of the lower

frequencies must be made such that they are approximately one octave of separation. The choice of f_L = 1GHz and 2 f_L = 2GHz will serve as a sample case. From the wavelength λ_L at the lowest frequency corresponding to f_L of 1GHz, the unit cell size $ux = \lambda_L/2$ can be determined. By comparison the next largest cell corresponds to frequency $2f_L$ which is 2 GHz and has a unit cell size of $\lambda_L/4$ and is one half that of the 1 GHz array. Figure 2-1 illustrates the 1 GHz unit cell and the unit cell for the 2 GHz cell superimposed with both odd and even symmetry. Notice the odd spacing will co-locate the center position of both the 1 GHz and 2 GHz element for this reason a green "X" has been placed at the point of coincidence.

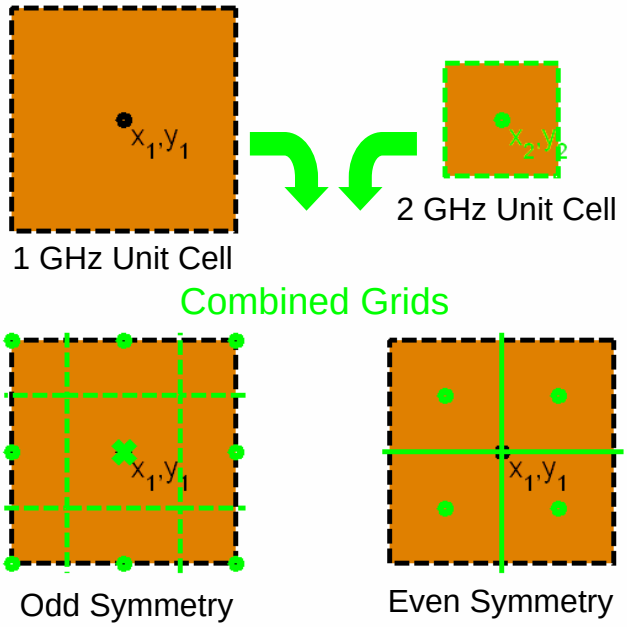

Fig. 2-1 The 1 GHz unit cell and the odd (left) and even (right) symmetry of the 2 GHz lattice.

For some antenna geometries the coincident condition of the grid nodes would represent an issue; however, for loop antennas with differing outer dimensional sizes the layout is still a valid option. It should be noted that future discussions will show why two concentric loops should not

be placed within each other to ease the integration of the higher band array. The concatenation of multiple arrays is also complicated by the need to extend the terminating panel by an addition quarter of a cell to fully populate the 2 GHz array. Figure 2-2 shows the two possible orientations for the 2 GHz lattice with elements shown in the unit cell layout.

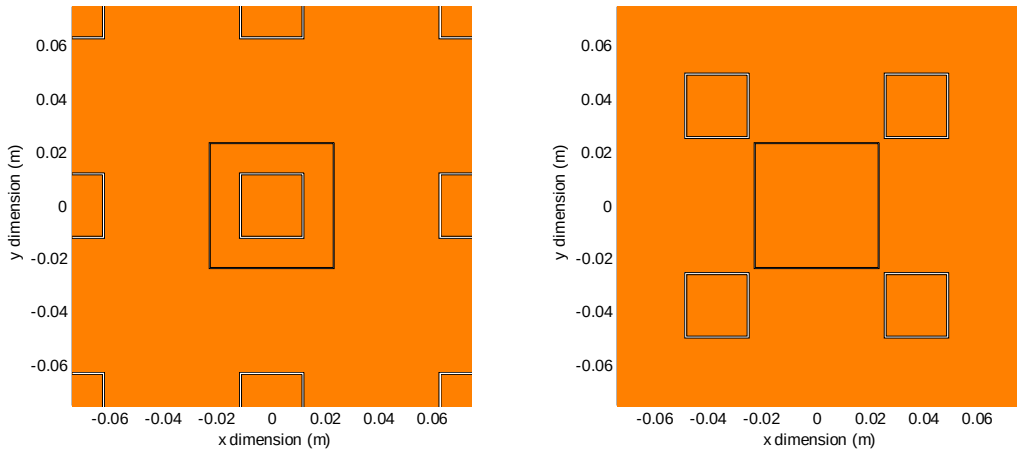

Fig. 2-2 Unit cell with dual band slot layout shown with odd (left) and even (right) symmetry.

2.4 Design of the Slot Loop Antennas

The design shown in Fig. 2-2 illustrates two antennas that are approximately one octave of separation in frequency. The even symmetry condition best illustrates when the elements are contained within the unit cell capable of independent replication. The perimeter of each of the loops is roughly the free space wavelength at resonance. In the case of the 1 GHz loop it is approximately 300mm and for the 2 GHz loop it is 150mm. By geometric inspection the slot loops are then a quarter of a wavelength on each side. Figure 2-3 shows the actual size of the loops that when formed would resonate on the ground plane surrounded by free space. When the two structures are combined it is apparent that the slot loops intersect rendering the design inoperable.

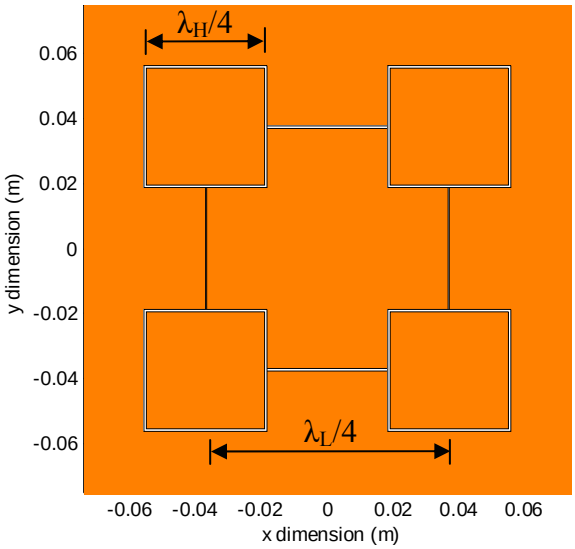

Fig. 2-3 Overlapping of slot loop antenna arrays with each operating at its own resonance.

A solution proposed is to use PCB to feed the antenna which has higher permittivity than free space to reduce the loop sizes until no overlap is observed. Figure 2-4 is a notional illustration of the effective loading with the PCB dielectric and how material permittivity can be used to reduce the physical size while keeping the electrical length of the perimeter the same. The design proposed incorporates a second dielectric adding a superstrate to the adjoining side of the slot that will fully enclose the loop. The use of two identical dielectric boards will not only improve the balance of the field distribution in the slot due to symmetry but will also become part of the stackup utilized by the multiband design. Figure 2-5 illustrates the material stackup of the slot loop antenna that is embedded within the shared ground plane of the two dielectrics. For clarity the dielectric boards have been omitted to show the top layout view. Since slot antennas support an electric field distribution in the gap opening, an interface is required to provide connection to the system. This can be accomplished using a balun to provide a differential feed or through induction by proximity coupling to a microstrip line. The coaxial transmission

connection terminating at layer 2 uses a microstrip stub and has a center conductor that is soldered to it on layer 1. Two feed arrangements are proposed for this stub fed design which allow connection from the edge with microstrip line or from below with a coaxial transition to the inductive stub.

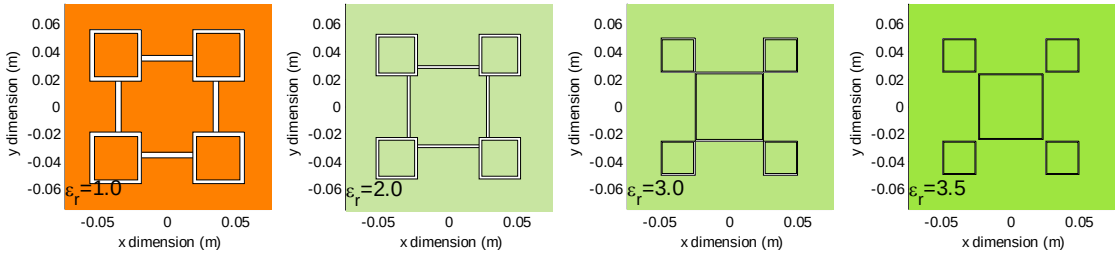

Fig. 2-4 Dielectric loading of resonant slot loop to reduce the physical size.

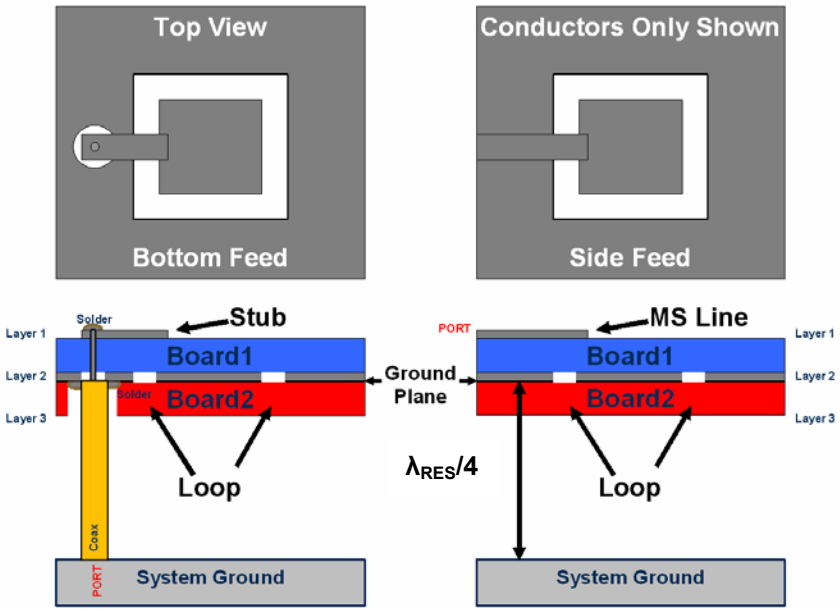

Fig. 2-5 Material stackup and layout for a resonant slot loop antenna over a ground plane.

2.5 Partition Assessment for Tri-band Capacity

Assessing the relative proportion of the slot area to the expanse of ground plane available in the even layout of Fig. 2-2 it is clear that there is a capacity to introduce the additional high frequency array elements as proposed. The exact area available for each element is to be considered prior to element selection and design. The principal consideration is no high frequency array element should be overlapping either with the 1 GHz or the 2 GHz slot. The useable area is therefore contained by the edges formed by the innermost loop boundary of the two elements, respectively shown in Figs. 2-6 and 2-7.

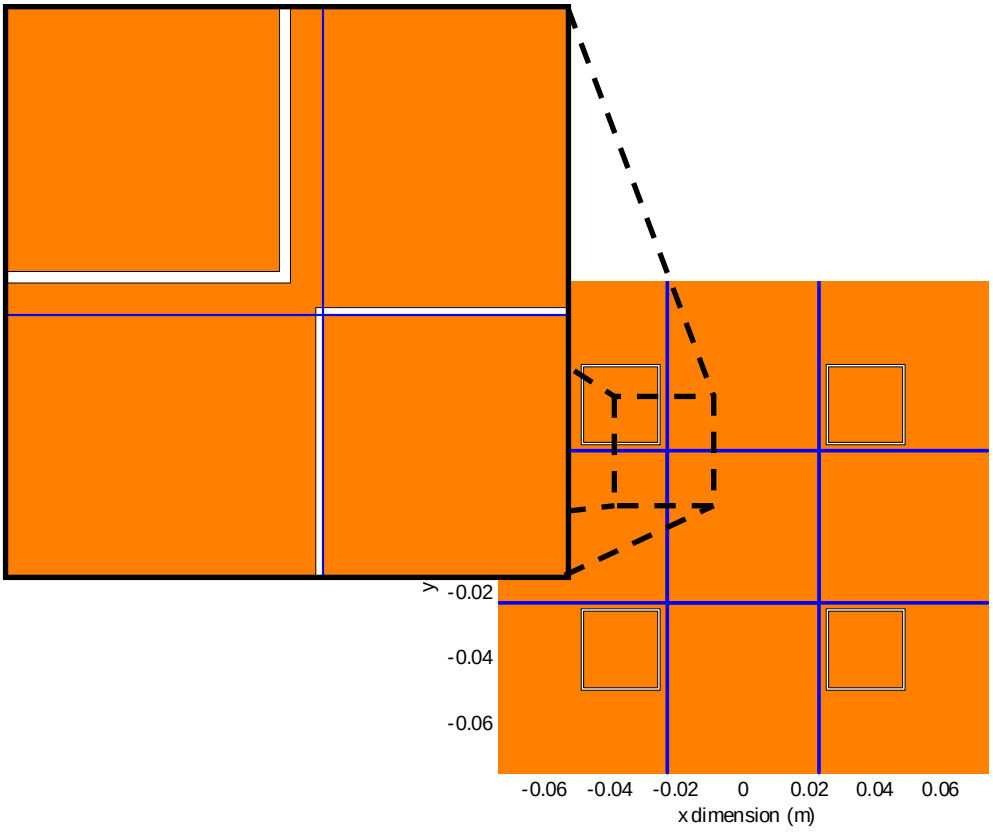

Fig. 2-6 Surface partition line formed by the inner loop of the 1 GHz array.

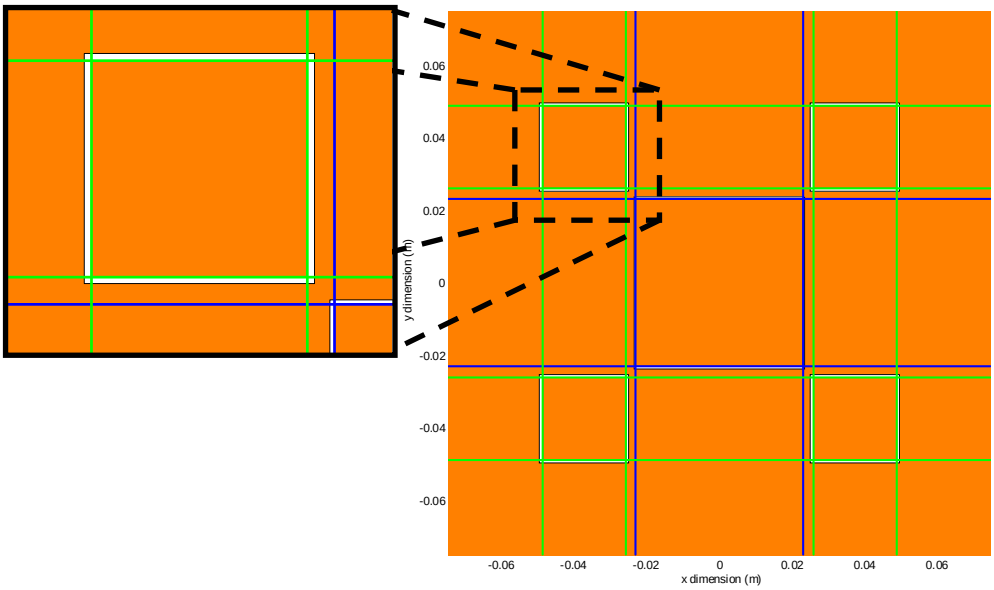

Fig. 2-7 Surface partition line formed by the interior edge of the 2 GHz arrays.

The small areas between the partition lines in the plots represent the forbidden regions for which the high frequency elements are restricted. If geometric symmetry is to be preserved within the 2 GHz lattice then each line must be mirrored to form the complete set of restriction boundaries as shown in Fig. 2-8. This set of small square and rectangular regions which are formed between these edges govern the design of the higher frequency array.

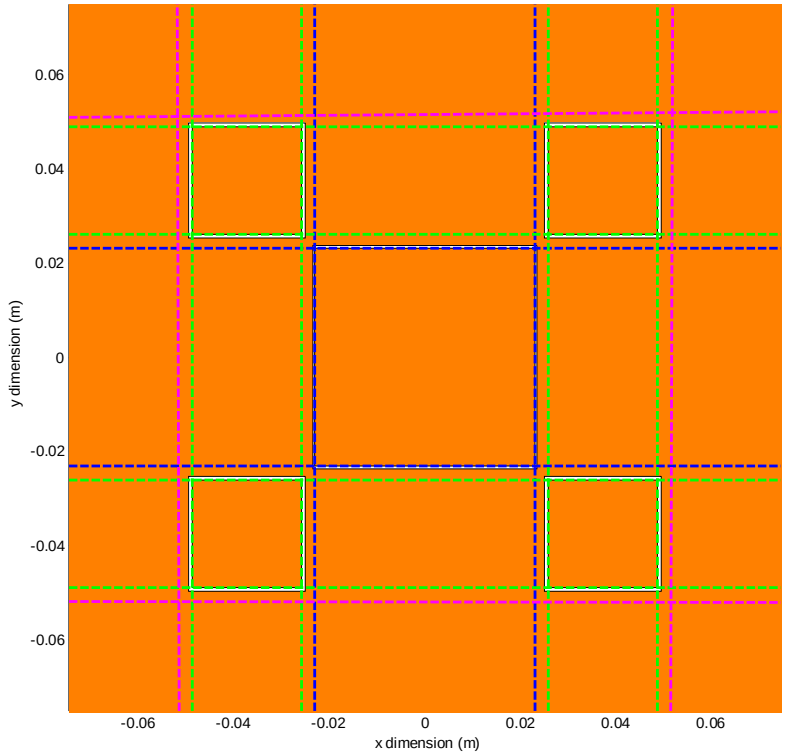

Fig. 2-8 Implied symmetry projected from the 2 GHz lattice.

From the given parameters the tabulation of maximum element extent can be computed and aid in the selection of possible elements types. Figure 2-9 illustrates how the relative orientation of a patch antenna changes with frequency and lattice position. Only those elements that do not overlap are considered valid candidates. Examination of the 12 GHz lattice shows the patches maintain adequate clearance to the slot loop antenna using the even layout hence it is chosen to populate the high frequency array as shown in Fig. 2-10. The symmetry of the unit cell sub-array can then be exploited to create a full array without violation of the periodicity of any of the internal bands. A representative 3 x 3 array is shown in Fig. 2-11 to illustrate the concept.

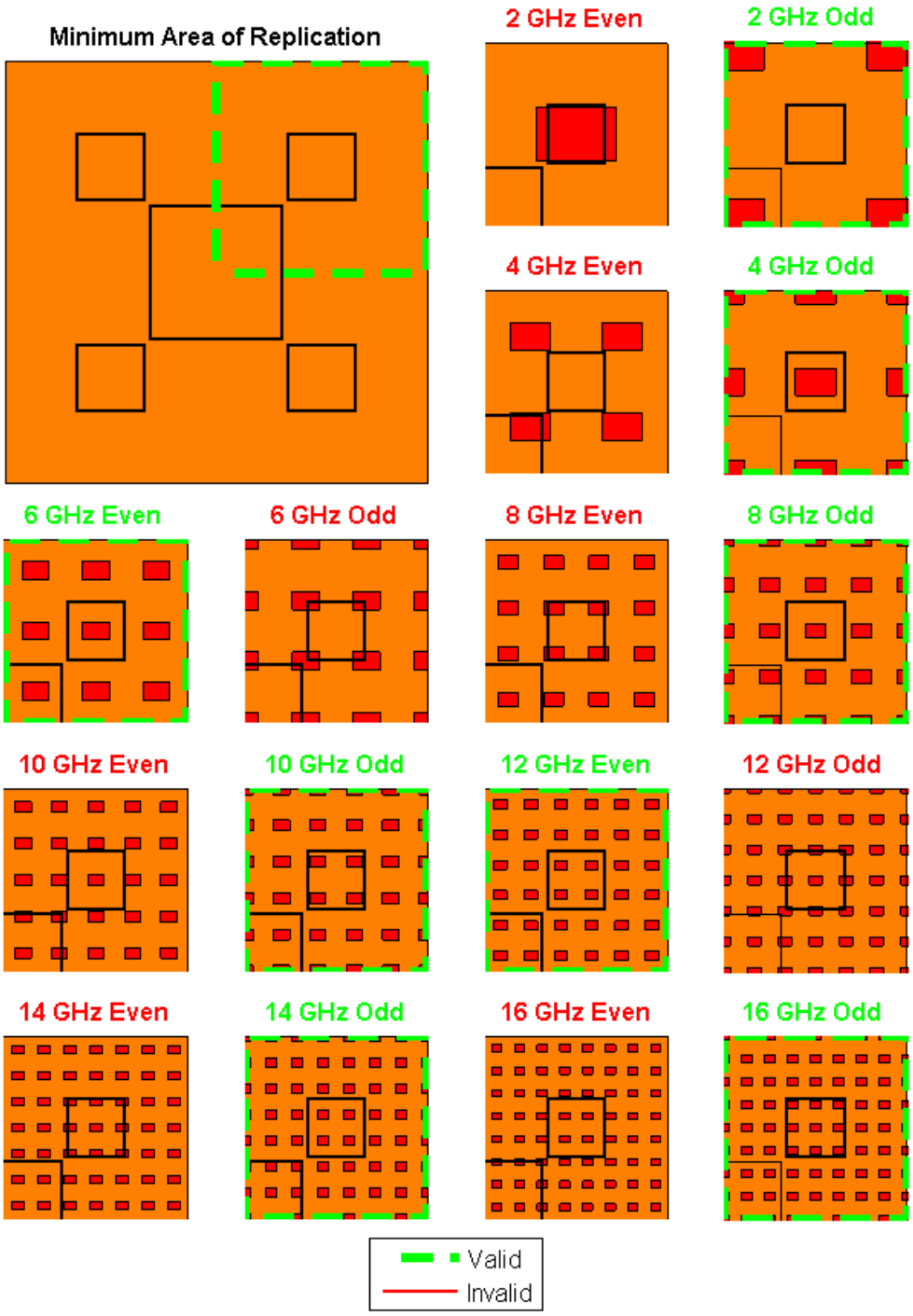

Fig. 2-9 Geometric analysis of the high frequency array options showing that the 12 GHz even case is a valid configuration.

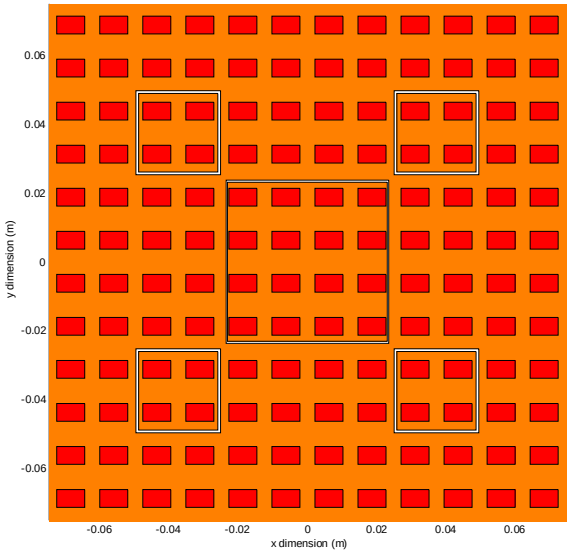

Fig. 2-10 Unit cell layout of tri-band array using the 12 GHz array and even symmetry.

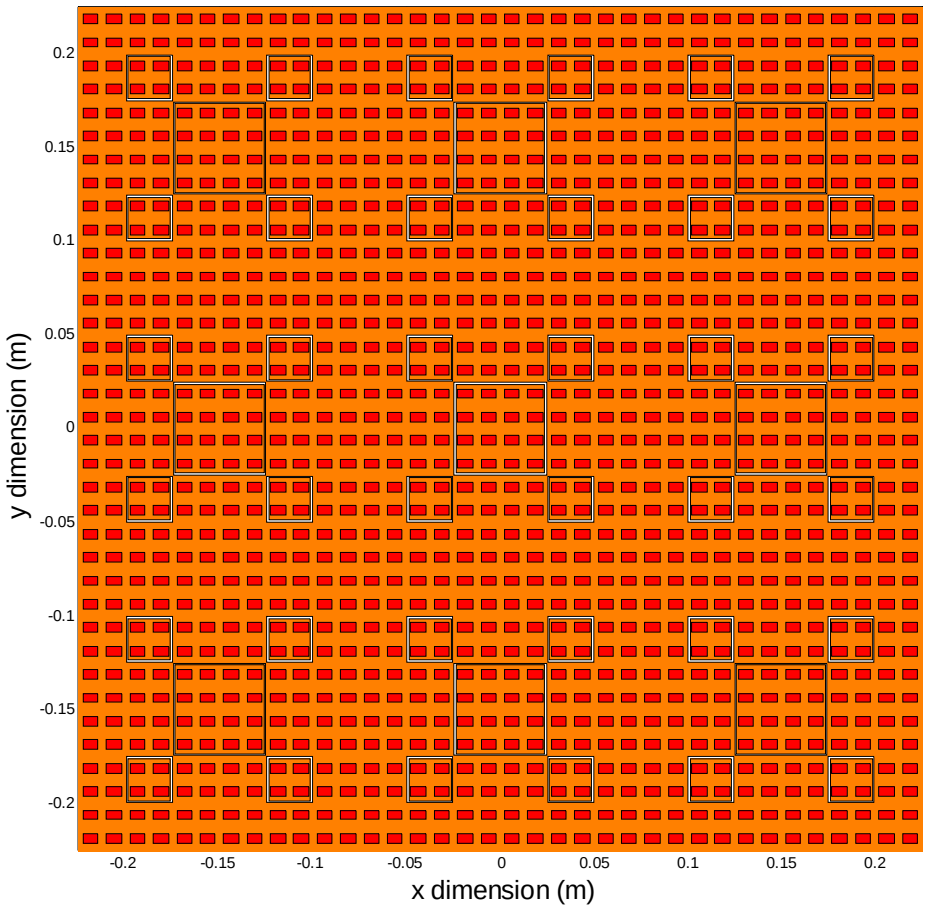

Fig. 2-11 Concatenation of 3 x 3 unit cells to form a tri-band array layout (1 GHz, 2 GHz, and 12 GHz).

2.6 Design Flow

The design process for integration of the three antenna arrays is summarized in Fig. 2-12. The resonances of two lowest frequencies can be approximately multiples but it is critical to emphasize that to ensure lattice alignment they are exactly the octave spacing. The initial step is to determine the resonant size of the loop constructed using the PCB materials for both of the lowest frequencies. The calculation of the overlap can then be determined. If overlap does exist, then the loop size is reduced iteratively by increasing the permittivity which influences the physical size at resonance. The process is then repeated until both designs can be placed on the same ground plane and achieve an acceptable mutual coupling value. Finally, the arrangement of the high frequency array can be analyzed to determine the maximum extent of the element size. It is at this point the antenna type should be chosen to minimize impact of the low frequency array through undesired blockage.

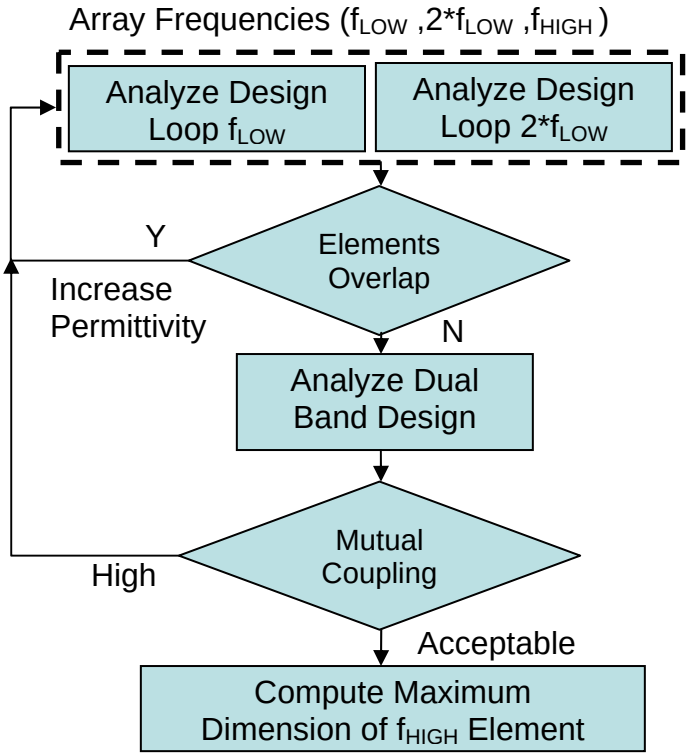

Fig. 2-12 Tri-band array design process.

2.7 Array Feed Structure

The aperture arrangement techniques developed in previous sections demonstrate the initial steps in the design of a tri-band array. The next consideration is the microwave feeds which are required to facilitate connection between the system and individual elements. For the antenna to be multifunctional it must have the ability to scan each array independently. This requires channelized feeds to each of the elements and distribution from three separate beamformers. The slot loop antenna described in Section 2.4 requires an additional system ground plane behind the slot loop to provide shielding for the system as well as to increase forward gain. The forced separation between the two ground planes not only increases the overall thickness of the structure but also increases the design complexity of the feed networks since all of the RF distribution must span this void. The coaxial transmission line solution introduced in Section 2.4 and shown in Fig. 2-5 was again used for the high frequency array but modified to interface a stripline feed network. Figure 2-13 is a notional representation of the material stackup required for RF distribution. The stripline feed network can be incorporated when board 3 is added to the original loop design. The combination of boards 2 and 3 then form the two symmetric dielectric and grounding structures supporting the stripline feed network. The additional ground plane requires a second loop profile be removed from Layer 4 to prevent shorting of the 1 and 2 GHz antennas. The two stripline ground planes on layers 2 & 4 are connected with a via fence that surrounds the trace paths. The use of a via wall with sufficient density (~λ/10) should provide isolation between adjacent channels and decrease mutual coupling. The system connection consists of a coaxial feed line that shares a common ground with layer 4 when soldered. The center pin of this coax is connected to the stripline on layer 3 by soldering through an access hole on top of the board to feed a corporate distribution network on

the same layer. Each of the patch antennas on layer 1 is then fed by a coaxial pin originating on layer 3 at each of the terminating branches of the divider.

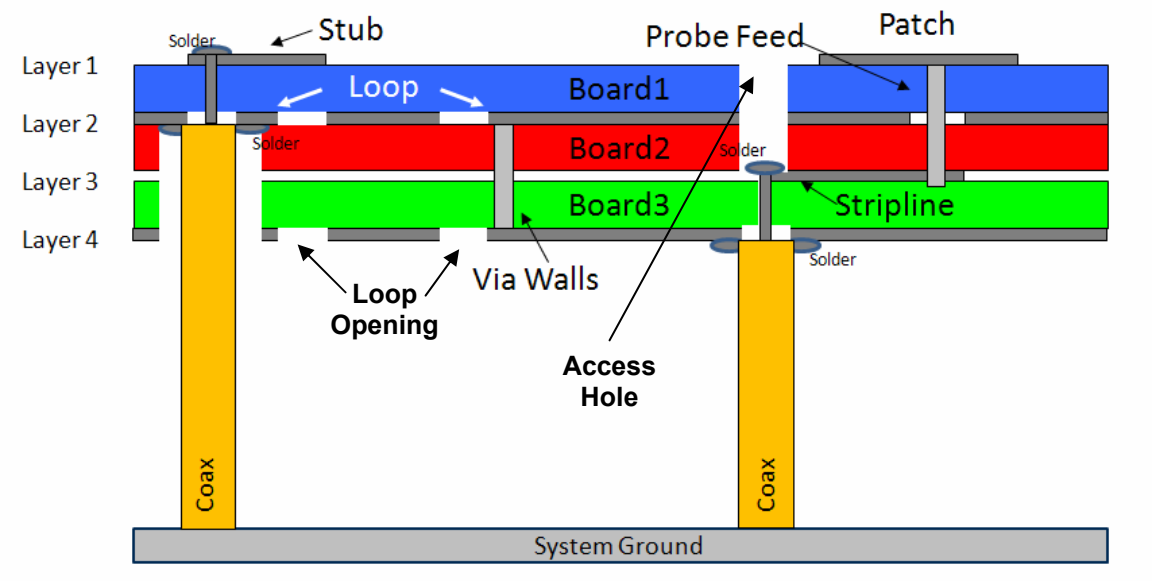

Fig. 2-13 Material stackup for RF signal distribution (not-to-scale).

The feed network for the high band array is complicated further by the total number of elements requiring an individual coaxial connection to be made. To reduce the total number of coax feeds required, the high frequency elements will be fed using a stripline 2 x 2 corporate feed network integrated into the stackup. Although this will widen the phase center distribution for the sub-array and lead to grating lobe onset at lower scan angles, the scope of this work will focus on a fixed beam without allowance for electronic scanning. Figure 2-14 shows the stripline feed network. The attachment of the coaxial transmission line is made at the input port. The distribution points are attached to a probe feed pin that is used to excite the patch antenna on layer 1 and shown in Fig. 2-15. The isolation of the feed and the slots is improved by adding a via fence between layers 2 and 4. The via fence was created by generating a contour offset by 2mm from the stripline network then populating the vias along it at 2mm spacing. In Chapter 4,

the focus will be on the reduction of the separation distance between the slot plane and system ground by incorporation of an artificial magnetic conducting material.

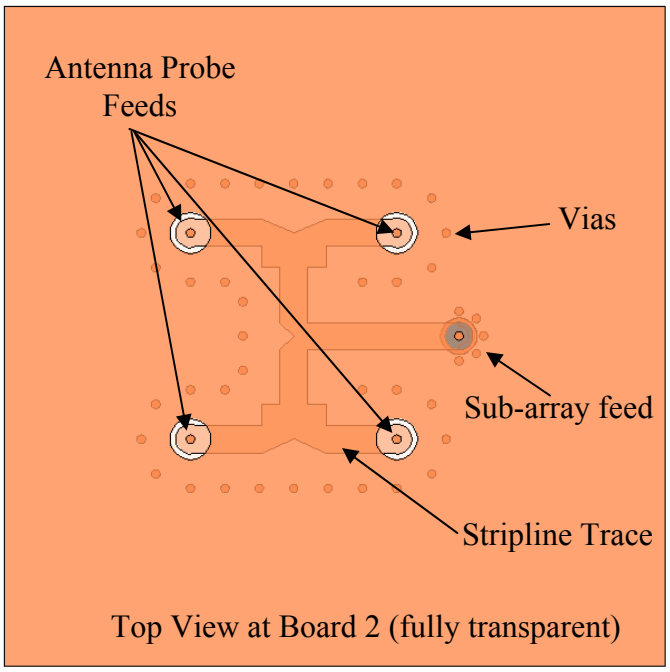

Fig. 2-14 Stripline corporate feed network for the high frequency array.

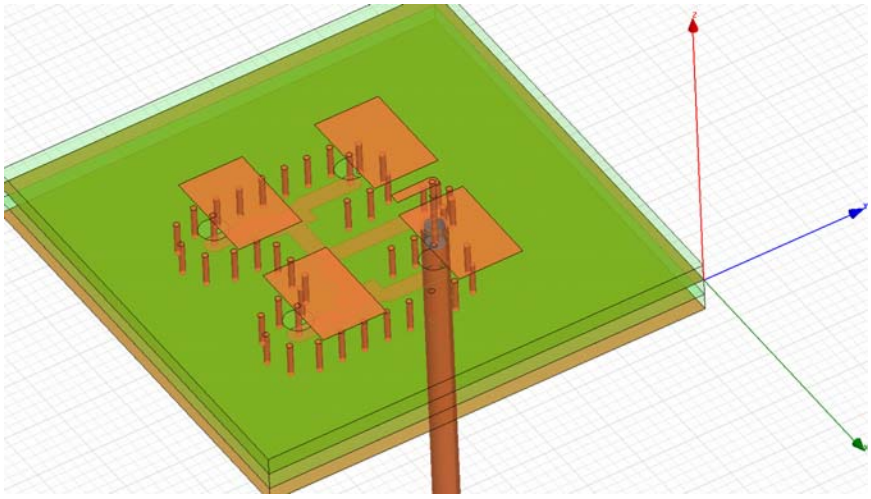

Fig. 2-15 Stripline corporate feed network for the 2 x 2 X-band patch array.

CHAPTER 3

INTEGRATION OF CAVITY BACKED SLOT ANTENNAS

3.1 Slot Antennas Integration

Slot antennas are unique in that they can be integrated into a metallic ground medium to form an aperture making them both structurally stable and conformal to a variety of installations. The partitioning of the ground plane to support arrays of multiple antenna topologies discussed in Chapter 2 further increases their utility. One consequence of the slot antenna extending through the ground plane is that it behaves as a bi-directional radiator and produces a main beam in both directions normal to the ground surface. The undesired radiation which propagates in the backward direction must be attenuated or reflected to prevent electromagnetic interference within the system. By inserting a metal ground plane below the slot, the back lobe will be reflected and hence increase the forward gain if constructive addition with forward radiation is achieved. Chapter 3 will focus on the design of slot loop antenna, placement of the reflector, and integration of the two bands into the unit cell.

3.2 Linear Slot Antenna

A slot antenna is formed when a specific shape of metallization is removed from the ground plane to support a resonant mode and radiation. The linear slot antenna located in an

infinite PEC ground plane represents the simplest case of this type of radiator. The radiated fields from the linear slot antenna shown in Fig. 3.1 are produced by an impressed *x*- directed electric field in the aperture of the form:

$$\mathbf{E} = E_g \sin k_0\left(l - |z|\right)\hat{x} \tag{3-1}$$

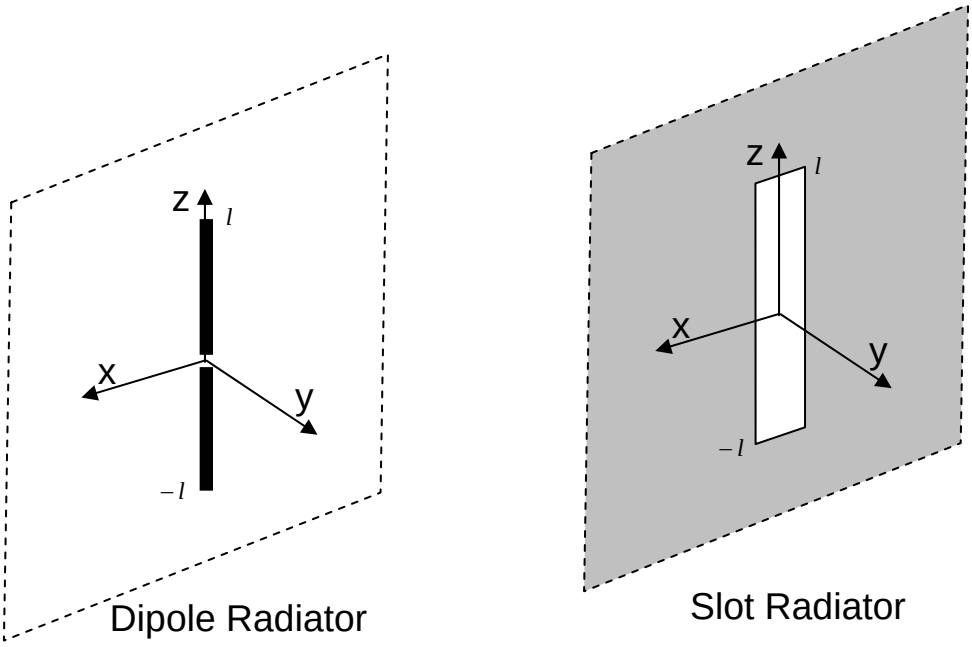

Fig. 3-1 Electric and magnetic radiators.

Mathematically, the slot in an infinite PEC ground plane is equivalent to a magnetic dipole radiating into both half spaces [11]. In fact, the dipole antenna shown in the left of Fig. 3-1 is the dual of the magnetic dipole (slot). The derived field components subject to the boundary conditions provides some additional insight into radiation mechanism of the half wavelength slot where the radiated electric field is specified as:

$$E_\phi = -j\frac{2aE_0}{\pi}\frac{e^{-jk_0 r}}{r}\frac{\cos\left(\pi/2 \sin\theta\right)}{\cos\theta}. \tag{3-2}$$

For the magnetic dipole the E_ϕ directed fields are constant in the *xy* plane; however, the electric fields produced in the two half spaces $y < 0$ and $y > 0$ are reversed in relation to each other as a result of satisfying the boundary conditions at $y = 0$ crossing the slot antenna interface. The plots shown in Fig. 3-2 indicate the magnetic dipole (slot in a PEC) has E field symmetry due to this boundary.

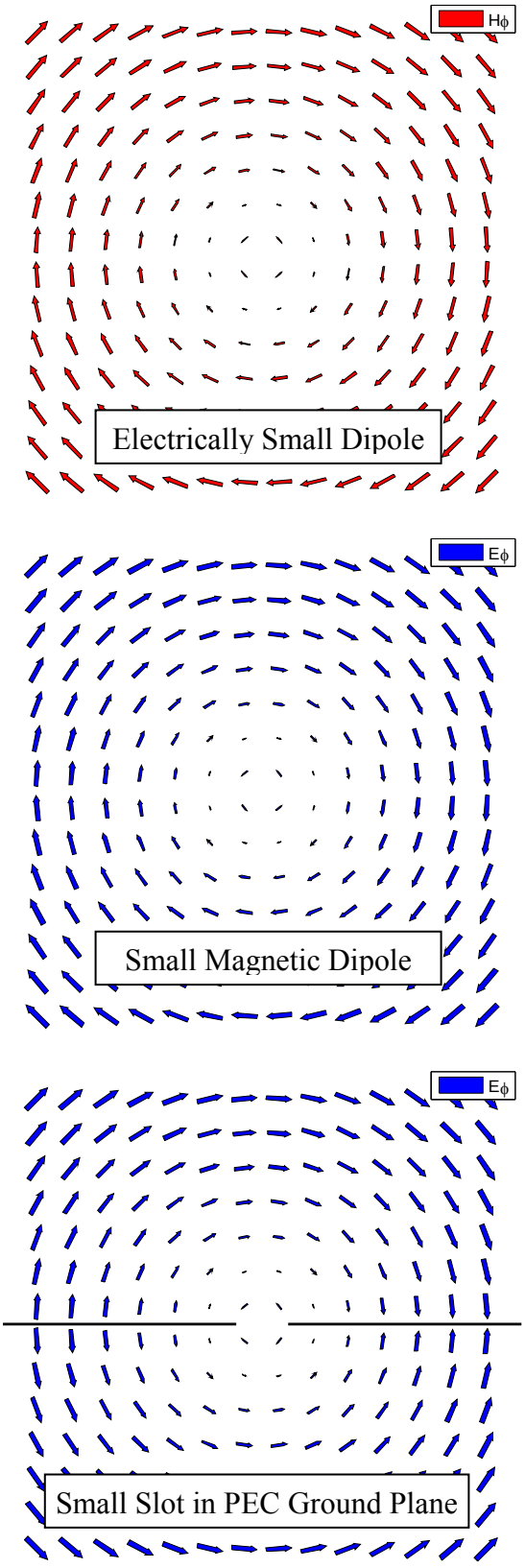

Fig. 3-2 Fields for the electric dipole, magnetic dipole, and slot in PEC ground plane.

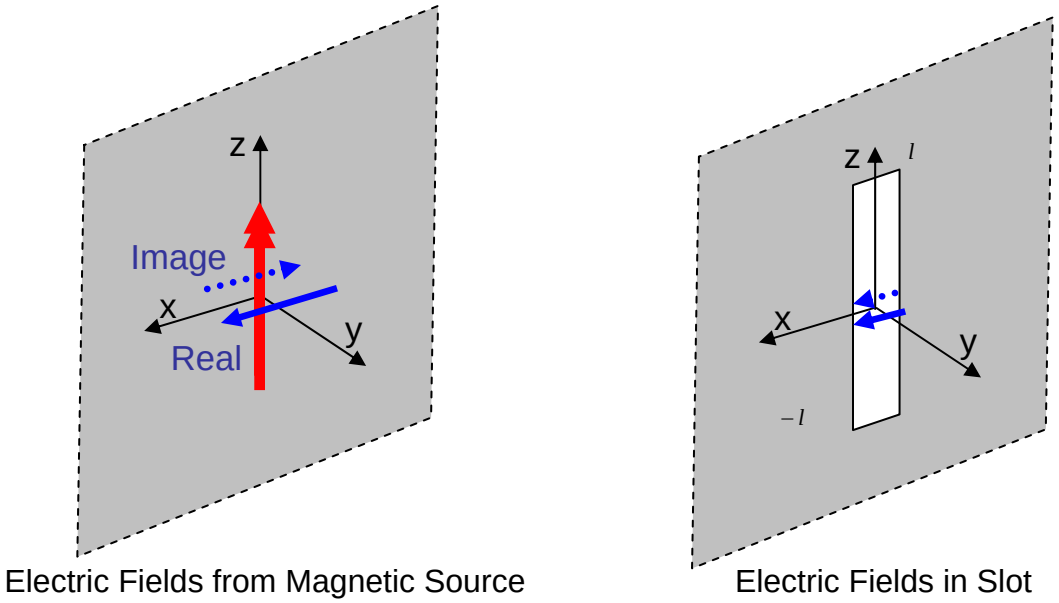

Fig. 3-3 Magnetic source and electric fields at the slot interface.

Figure 3-3 illustrates the electrically small magnetic dipole source embedded in the PEC ground plane. For each half space the real and image electric fields are shown. The imaged electric field produced by a magnetic source is therefore equal to the real field but is opposite in amplitude. It is clear from the right side of the figure that the electric field should be continuous across the slot such that both electric fields are the same. Therefore for each half space a magnetic source of equal magnitude but opposite polarity is required to construct the radiated field of an equivalent slot.

3.3 Slot Loop Antennas

The previous formulation is now considered for the slot loop antenna which is formed by the distribution of four magnetic sources [12]. Since phase variation must be considered vectors are required to describe the source coordinates.

$$\mathbf{M}_1 = \mathbf{M}_2 = -\hat{\mathbf{x}} M_0 \cos(\beta x'), |x'| \le \lambda/8 \tag{3-3}$$

$$\mathbf{M}_4 = -\mathbf{M}_3 = \hat{\mathbf{y}} M_0 \sin(\beta y'), |y'| \le \lambda/8 \tag{3-4}$$

The arrangement of the sources is shown in Fig. 3-4, and has been re-oriented to match the subsequent simulations and measurements.

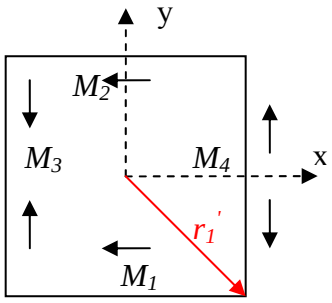

Fig. 3-4 Distribution of magnetic sources used to construct the slot loop radiated fields.

Since the analytical form is based upon four equally impressed sources, some variation can be expected when the antenna is excited using an inductive stub feed. To determine the effect a simulation of the magnetic current distribution was performed in FEKO. Figure 3-5 shows the square slot loop geometry formed into the surface of a finite electric ground plane with a 50Ω air-suspended microstrip line used as the source. The equivalent magnetic currents within the slot can be seen in Fig. 3-5 superimposed on the 3D rendering. Figure 3-6 is a plot of the simulated electric fields within the gap for each of the loop edges. The two complementary plots show the magnetic distribution is sinusoidal as predicted and consistent with the resonance of a one wavelength slot loop antenna.

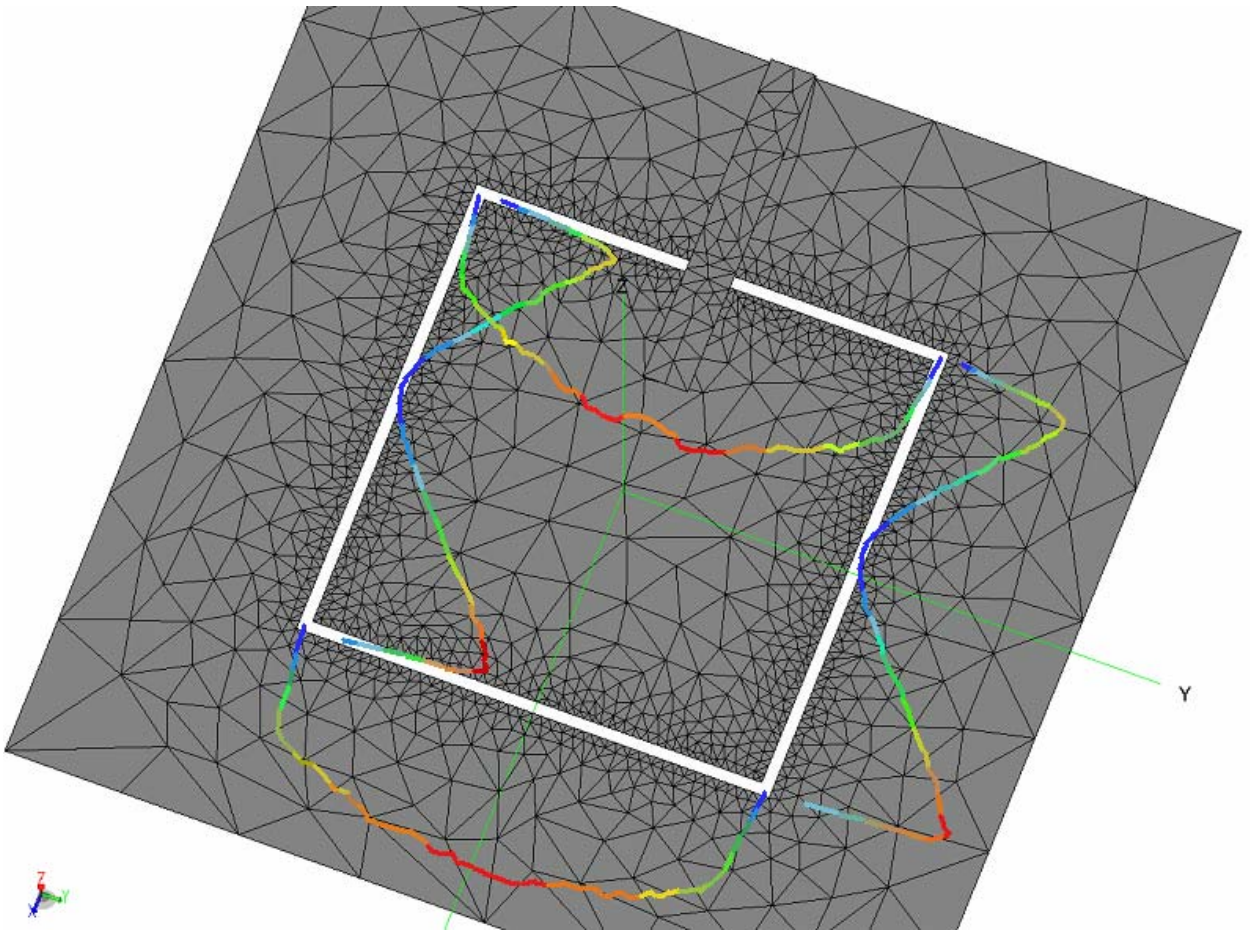

Fig. 3-5 Magnetic currents superimposed on the slot loop antenna.

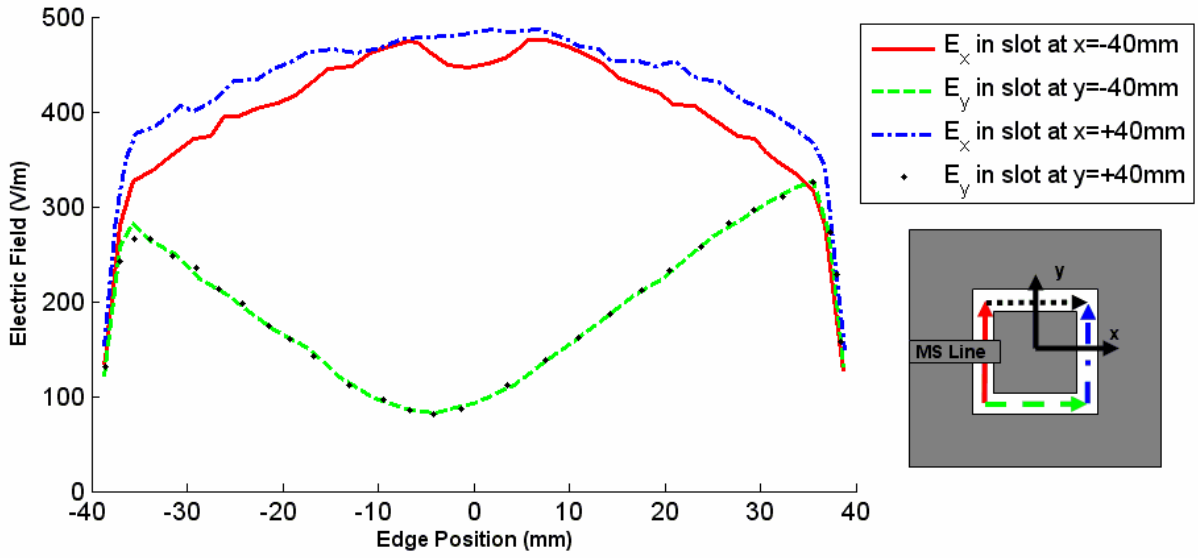

Fig. 3-6 Simulated magnitude of electric field in the slot loop.

3.4 Slot Loop Antenna Measurements

A dual band slot antenna was constructed as a test article for measurements. The smallest size capable of preserving all the features is based on the half wavelength dimension of the unit cell at the lowest operating frequency at 1 GHz. A secondary grid comprised of a sub-array of four 2 GHz elements was also created in a symmetric configuration. The slot antennas are formed in a common ground plane by etching the copper that lies between two 60mil Rogers Corp RO3035 dielectric boards. The upper dielectric board referred to as the superstrate supports the antenna feed lines which are 50Ω microstrip. These transmission lines use the same copper ground plane as loop geometries and are terminated along the board edge into end launch 3.5mm coaxial connectors for each antenna. By locating these five ports along the edge rather than from below as illustrated in Fig. 2-11, the interference from the test cable is reduced for the bi-directional and experimental cases to follow. The antenna was designed and simulated in HFSS to refine the dimensions in Fig. 3-7.

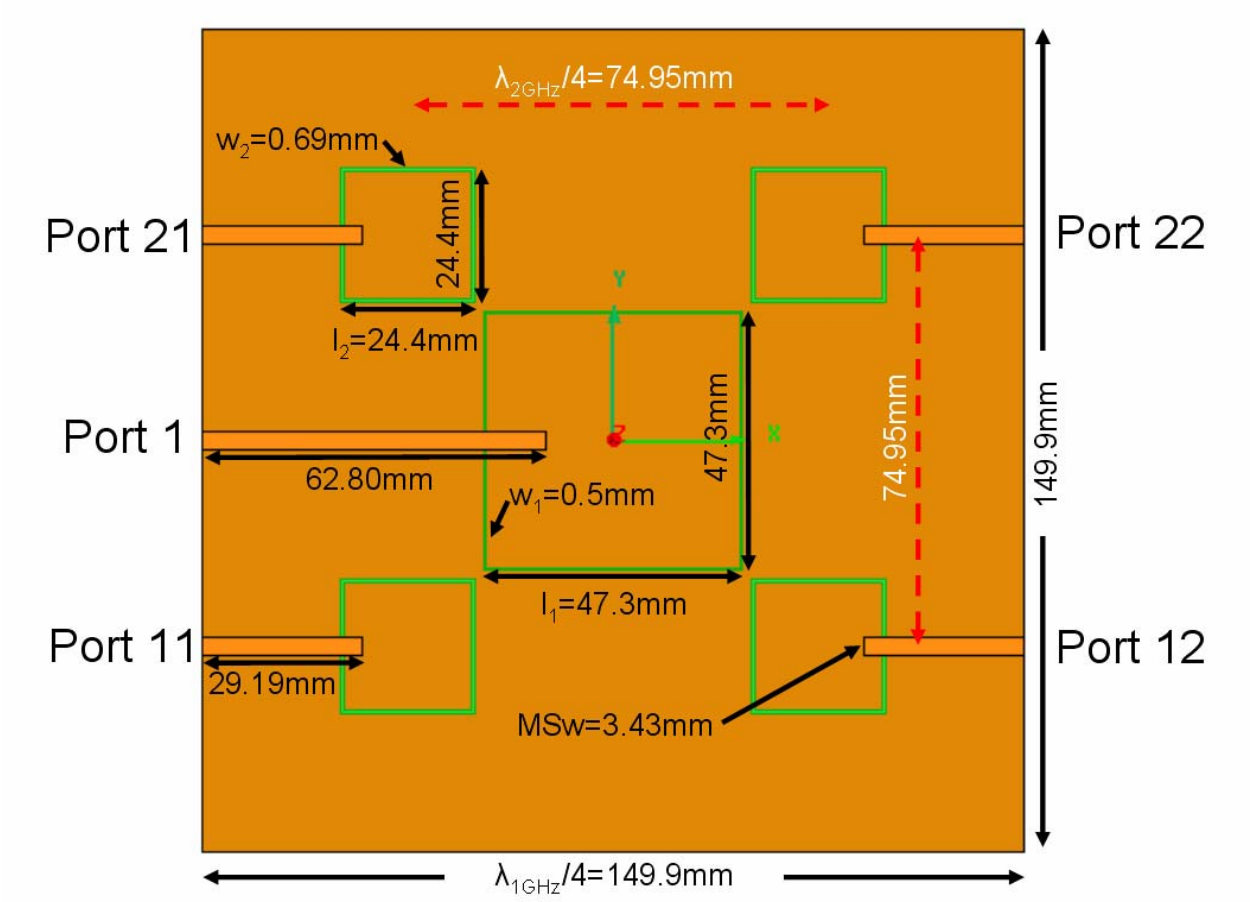

Fig. 3-7 Unit cell of dual band antenna optimized in HFSS simulation.

The reflection coefficient comparison of the measured versus simulated antenna design is shown in Fig. 3-8. The bandwidth of the measured antenna is 39.36 MHz centered at 0.984 GHz. The corresponding simulated bandwidth of the antenna is 44.00 MHz centered at 1.008 GHz. The performance difference between the measured and simulation data is minor but does show manufacturing variation which can detune the design from the intended resonant frequency. The slight shift of the two reflection curves is likely due to the etch process creating a larger loop than modeled. This increase in dimension would lower the resonance frequency at each band. Since the loop geometry is embedded in the ground plane between the two laminated dielectric slabs, inspection of the loop dimensions and slot opening could not be verified with any non-

destructive techniques. An additional observation of the reflection coefficient shows that a second resonance centered around 2GHz is well matched producing another radiating mode of the slot loop at the next octave, however the presence of this band is unintended. The presence of this second resonance is undesired since it will be parasitic of the 2 GHz antenna array and receive that interference at the 1GHz port. One solution is to include a filter at the 1GHz elements to reject this power. However, the preferred method is an improved design of the loops such that coupling is mitigated in the design itself. Such studies will be the subject of future efforts where more defined frequencies, bandwidth, and gain performance are specified.

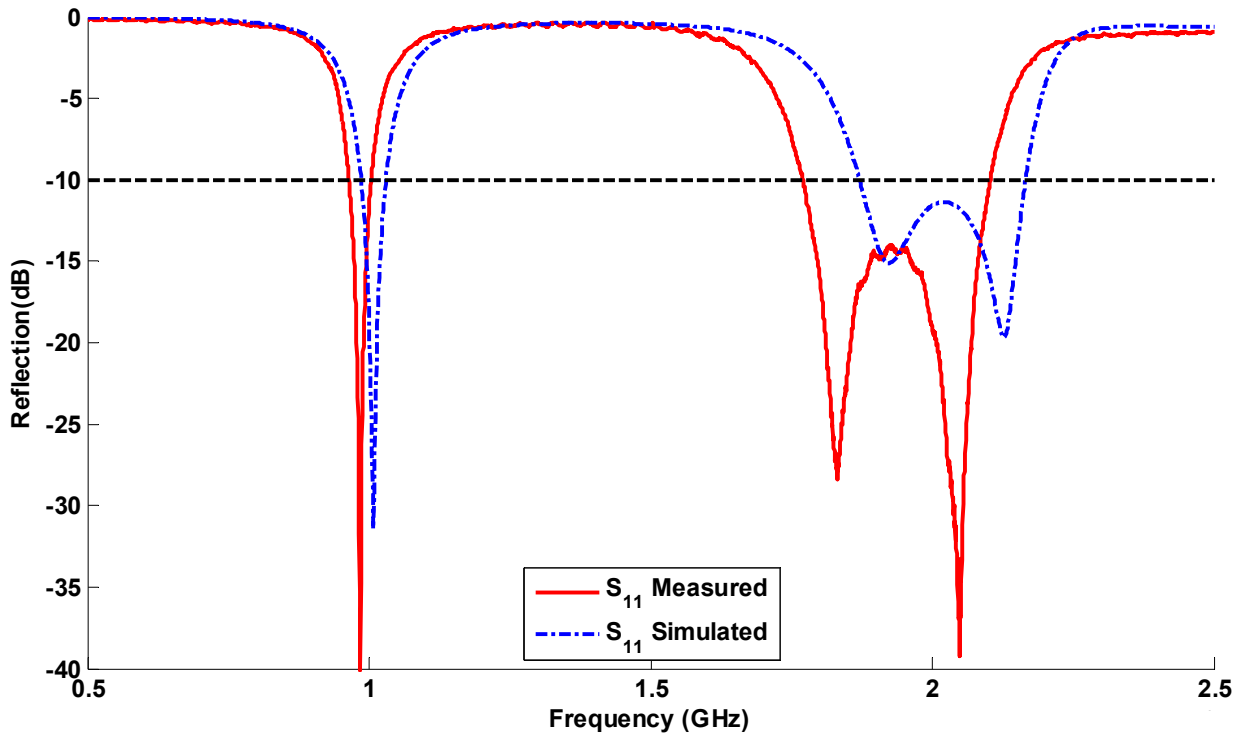

Fig. 3-8 Reflection coefficient comparison of horizontal polarized loop.

The antenna pattern measurements were performed using a cylindrical near field scanner which rotates the AUT on a fixed pedestal as vertical raster scans are collected on the circumference of a virtual cylindrical volume. The near field probe measurements collected along this grid are then processed into far field patterns using a spatial Fourier transform [13]. The advantage of this technique is that the measurements are automated and can be collected over a full rotation of the antenna. The limited extent of measurement in the vertical plane requires a second measurement to be performed to determine the full pattern of the elevation plane. To improve the consistency in the pattern measurements a special polyethylene mounting fixture was fabricated and attached to a rigid dielectric pole to maintain a repeatable spatial reference of the slot loop antenna throughout the experiment. Furthermore, the special fixture was designed with two attachment holes capable of orienting the antenna in a horizontal polarization to perform the ±180° azimuth pattern measurements as well as rotation by 90° to perform the ±180° elevation pattern measurements. The fixture was aligned such that the ground plane containing the slot loops was aligned directly over the center of rotation of the cylindrical pedestal axis. The fixture was attached to a plastic post approximately 3 feet in height to allow for an extended vertical scan. Horizontal polarization was only necessary and was used consistently throughout the following series of measurements.

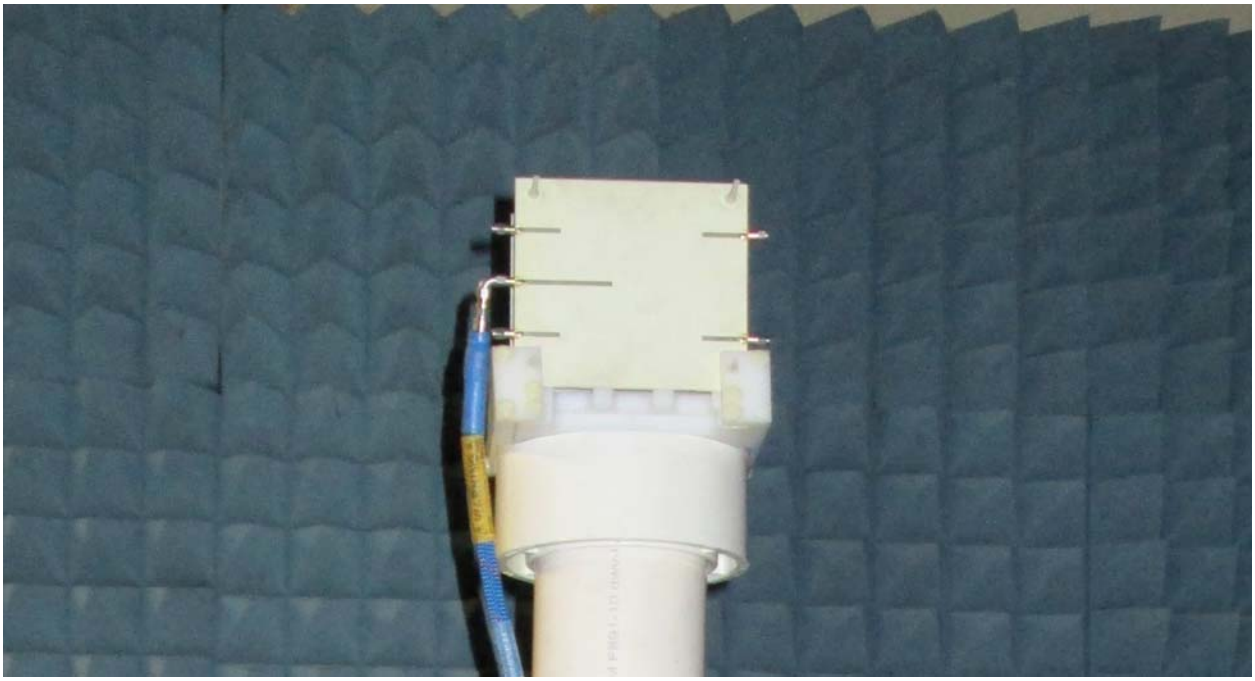

Fig. 3-9 Measurement setup for the 1 GHz linear horizontally polarized antenna in cylindrical near field scanner.

The slot loop within the ground structure has bi-directional radiation so the gain in both directions is comparable based on the simulation and measured data as shown in Figs. 3-10 and 3-11.

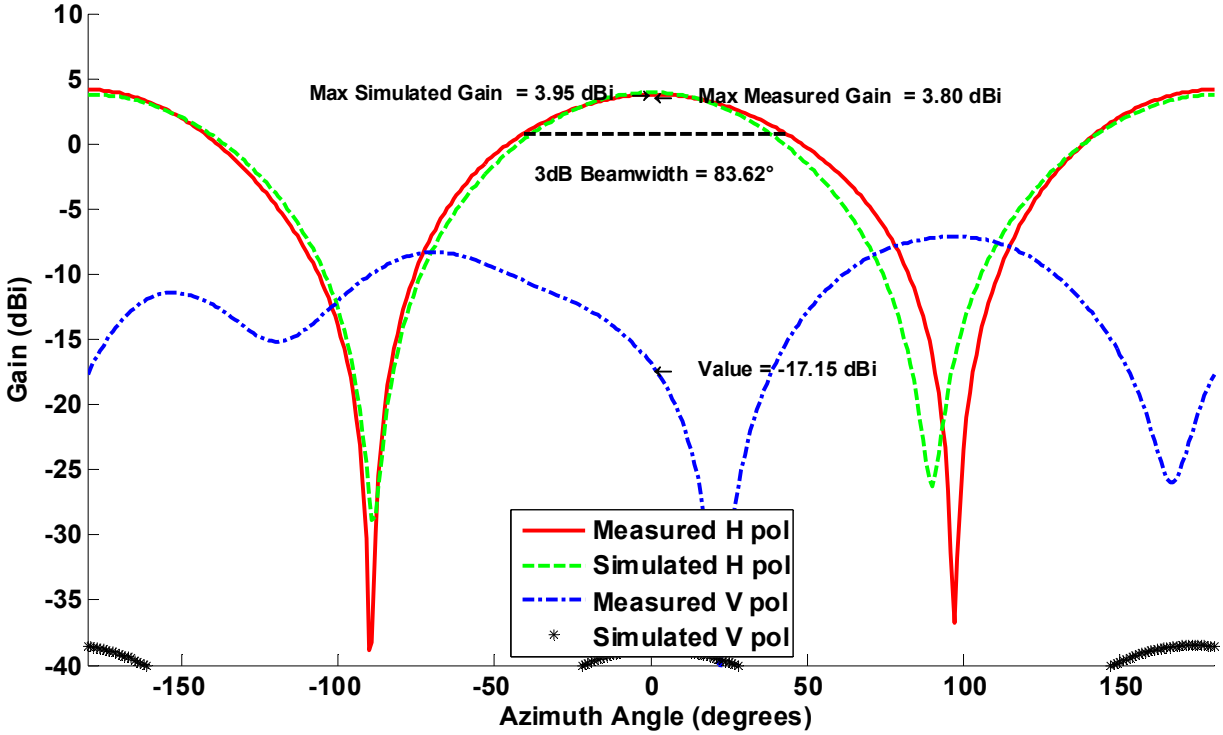

Fig. 3-10 Azimuth (E plane) pattern of the horizontal polarized loop alone at 1 GHz.

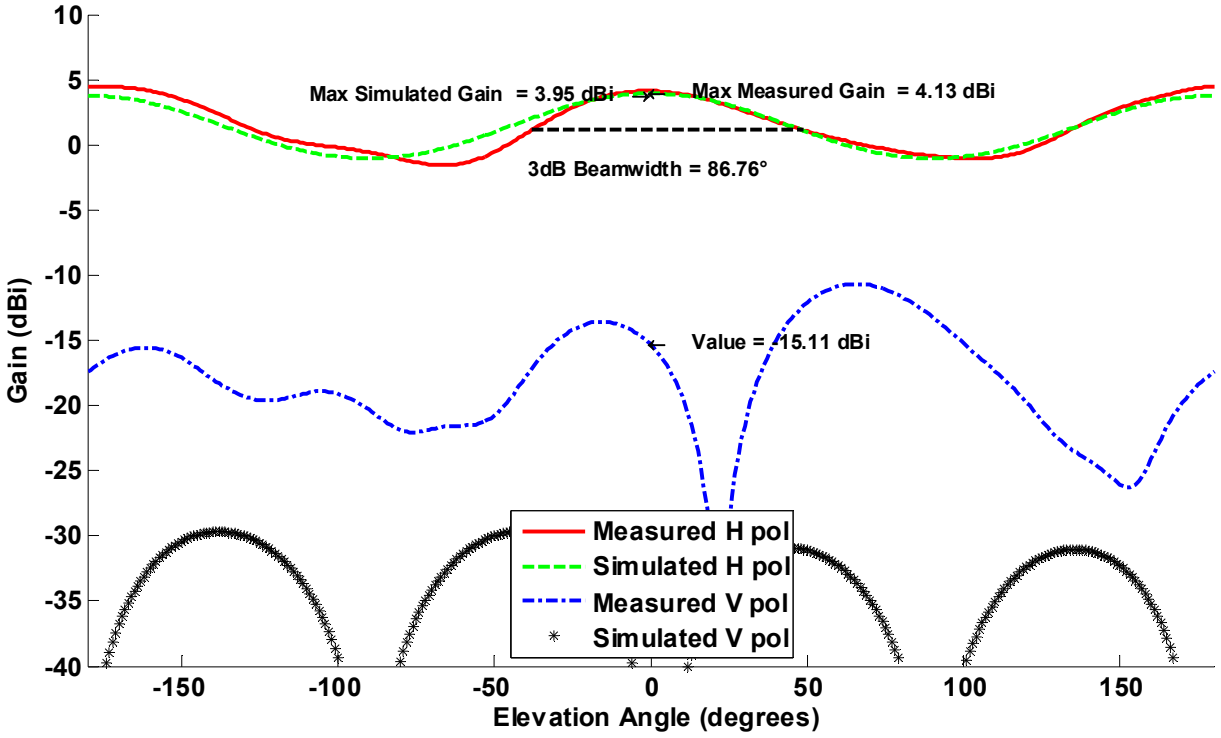

Fig. 3-11 Elevation (H plane) pattern of the horizontal polarized loop alone at 1 GHz.

The maximum gain predicted by the simulation was 3.95dBi versus the 4.13dB measured peak of the elevation pattern. The measured beamwidth of the azimuth pattern is 83.6° with an elevation beamwidth of 86.8°. The measured data processed from cylindrical near field measurement of the elevation pattern shows some deviation in the pattern beyond -50° so the predicted simulation beamwidth of 100.8° was not achieved likely due to some measurement or processing error that led to increased pattern loss in that region.

3.5 Reflector Backed Slot Antenna Measurements

To reduce the undesired effects of the radiation in the backward direction, a system ground plane should be added to shield electronics and increase the forward gain. The spacing between the plane containing the slots and the ground plane should be established at $\lambda/4$ of the resonant frequency. However, this is difficult due to the presence of both the 1GHz and 2GHz slot arrays. One option shown in Fig. 3-12 is to locate the reflecting plate at one quarter wavelength below the loop at the lowest frequency 1GHz. The resulting separation would be equivalent to one half wavelength separation at 2GHz a condition that leads to destructive interference, poor performance, and increased overall depth of the antenna system. The second option is to set the design overall thickness to one quarter wavelength height at 2 GHz. The following experimental measurements detail the impact of the aluminum ground reflector on the performance of the single 1 GHz elements reflection coefficient, radiation patterns, and maximum gain.

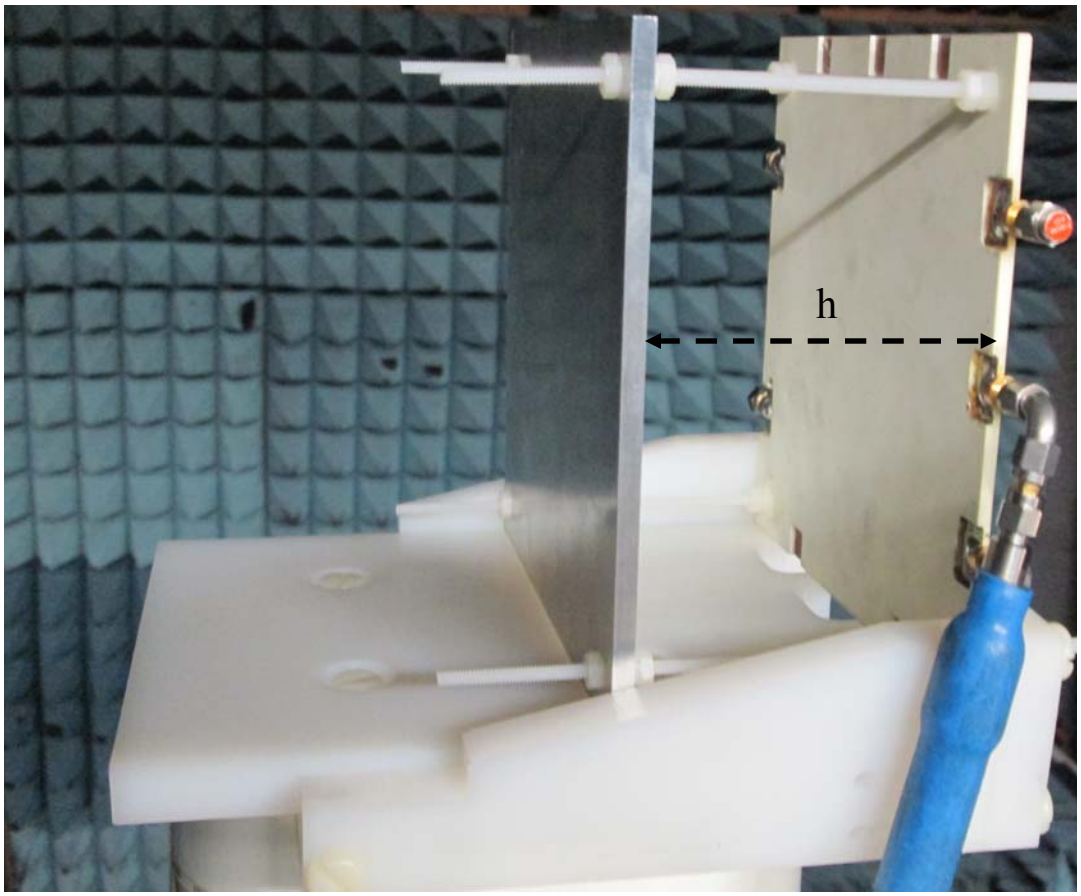

Fig. 3-12 Measurement setup for the reflector backed antenna at plate height h=$\lambda_{1GHz}/4$.

The inspection of the reflection coefficient data in Fig. 3-13 shows the loop antenna radiating bi-directionally with no reflector structure has the strongest resonance and widest bandwidth. The reflector plate was then assembled on the test stand with the antenna as shown in Fig. 3-12. The measured input reflection was measured for three heights of the reflector: λ/30, λ/8, and λ/4 at 1 GHz. When the reflector is located at the height of λ/30, the close proximity creates a shorting condition that not only detunes the resonance but also limits the radiation bandwidth. The λ/8 height case which reduces the overall height maintains a radiation bandwidth of 31 MHz however the center frequency of that resonance has been shifted up to 1.02 GHz. Finally, the

case with the reflector located at a height of λ/4 decreases the bandwidth slightly to 30 MHz but maintains the desired resonance at 0.99 GHz.

The impact of the reflecting ground plane on azimuth radiation patterns is shown in Fig. 3-14 for the four cases measured at 1.0 GHz. When the reflector is positioned at the height of λ/30 below slot, the close proximity of the electrically conducting plate effectively shorts out the slot resulting in very little radiation. Thus the poor impedance match for this condition and detuning results in a maximum gain of only -1.37 dBi at 1 GHz. The optimal physical position of the reflector in relation to the loop antenna is theoretically at λ/4. The measured gain at this spacing shows that a maximum gain of 7.55 dBi is greater than that of the loop alone while the resonant frequency is slightly detuned but still matched at 1GHz. The backlobe radiation from this case is also reduced by 6.05 dBi when compared with the loop antenna alone.

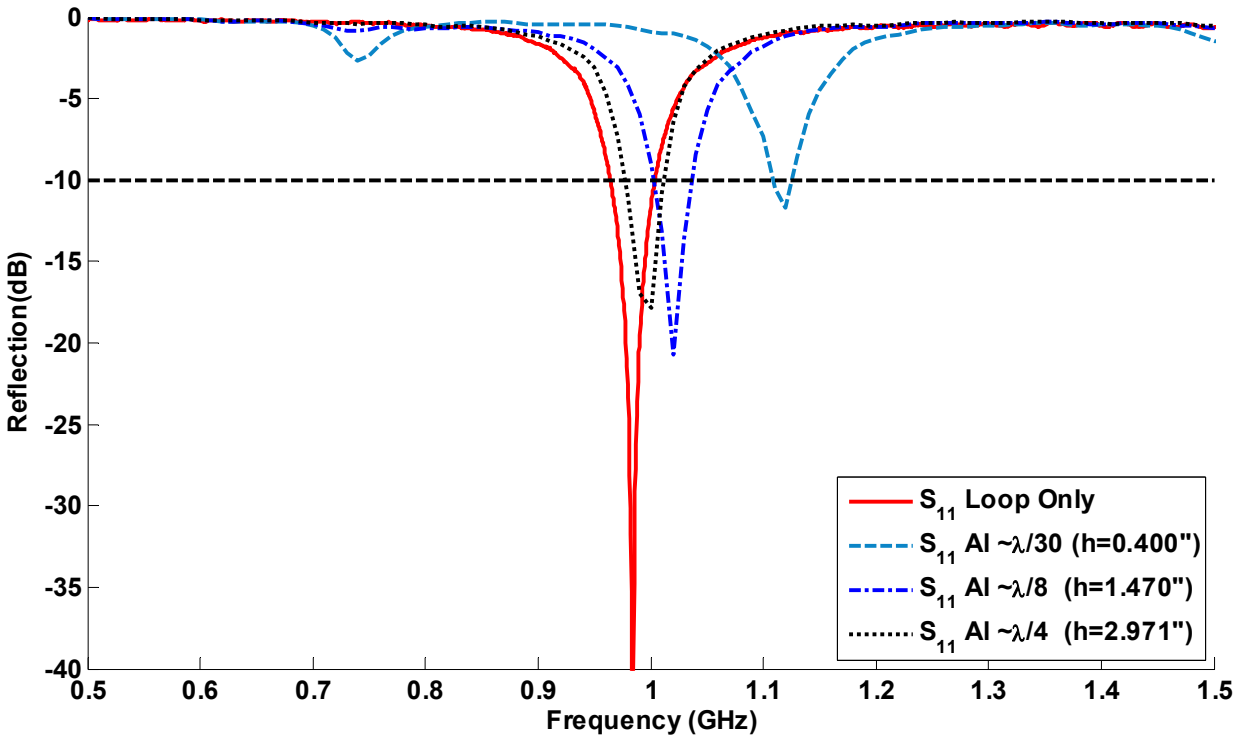

Fig. 3-13 Measured input reflection for the reflector backed antenna versus plate height.

In the third case the plate was repositioned to a height of λ/8 to determine its impact on the radiation patterns and maximum gain. For reasons expressed in the previous discussion, this height was considered as a compromise to provide a reflector at λ/4 for the 2 GHz slot loop array with reduced design height. The measurements of the azimuth radiation patterns show that the beamwidth of the λ/4 reflector compared to λ/8 is decreased from 70.0° to 66.4° although the maximum gains are numerically equivalent. The asymmetry of the azimuth patterns in Fig. 3-14 is due to the antenna being horizontally polarized and test cable with swept elbow scattering in the -90° angular range. It is evident from Figs. 3-14 and 3-15 that the backlobe radiation is reduced in all of the cases with a ground plane (plate), but the forward gain can only be increased when the reflected wave adds constructively. The measured data was then verified using an HFSS simulation of the dual band antenna with reflector located at λ/8. The resulting simulation required mesh containing 1.47M tetrahedra and used 62.1GB of system RAM to converge to a Δs=0.007 in 21 adaptive passes. Figure 3-16 is a comparison of the measured and simulated reflection at the 1 GHz element input. The azimuth and elevation plots for this case are shown in Figs. 3-17 and 3-18.

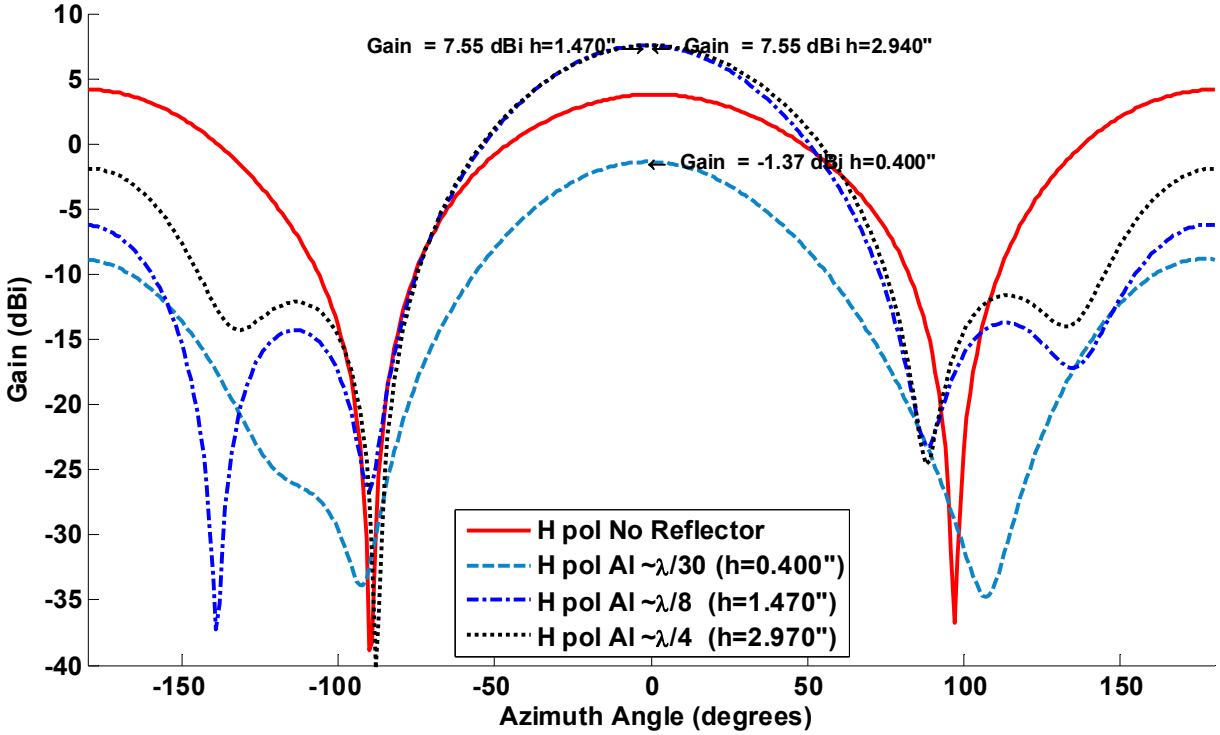

Fig. 3-14 Measured azimuth (E plane) patterns of the horizontal polarized antenna at 1 GHz.

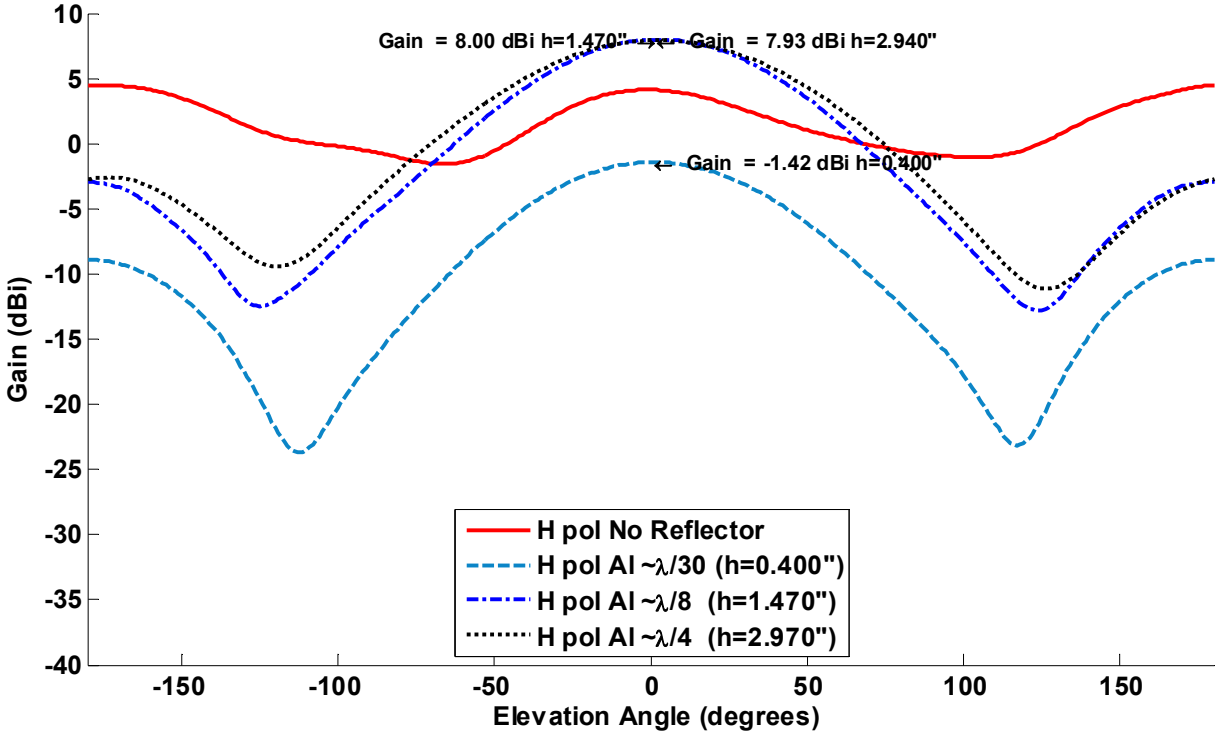

Fig. 3-15 Measured elevation (H plane) patterns of the horizontal polarized antenna at 1 GHz.

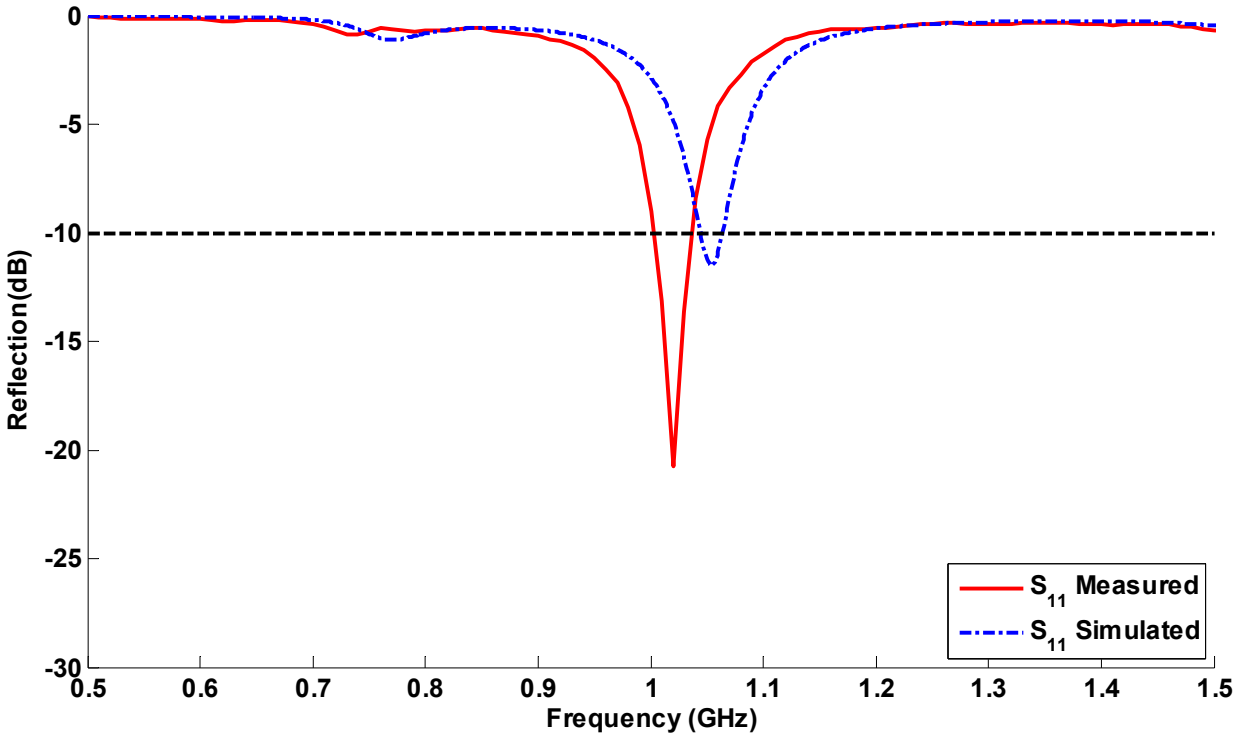

Fig. 3-16 Comparison of the antenna reflection coefficient with λ/8 reflector heights.

The variation in the two reflection curves is likely due to the low number of adaptive (iterative) passes (runs) in HFSS. Since the mesh is adaptively refined, a significant focus is dedicated to the loop antennas and their inductive feeds. If significant RAM had been available it is conceivable that increasing the mesh density would converge to a closer match. Moreover, the same resonance shift between the simulation and measurement was observed since the identical antenna was used for the reflector backed experiment.

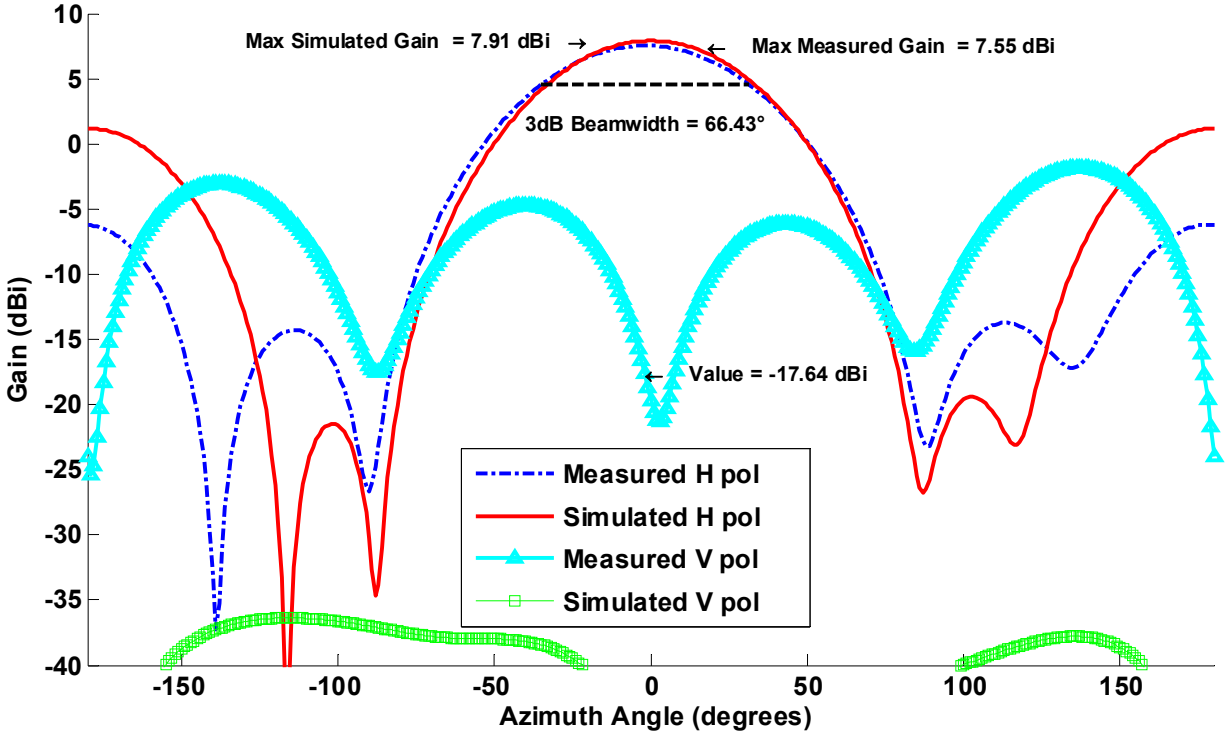

Fig. 3-17 Azimuth pattern of the horizontally polarized 1 GHz antenna with ground reflector at λ/8.

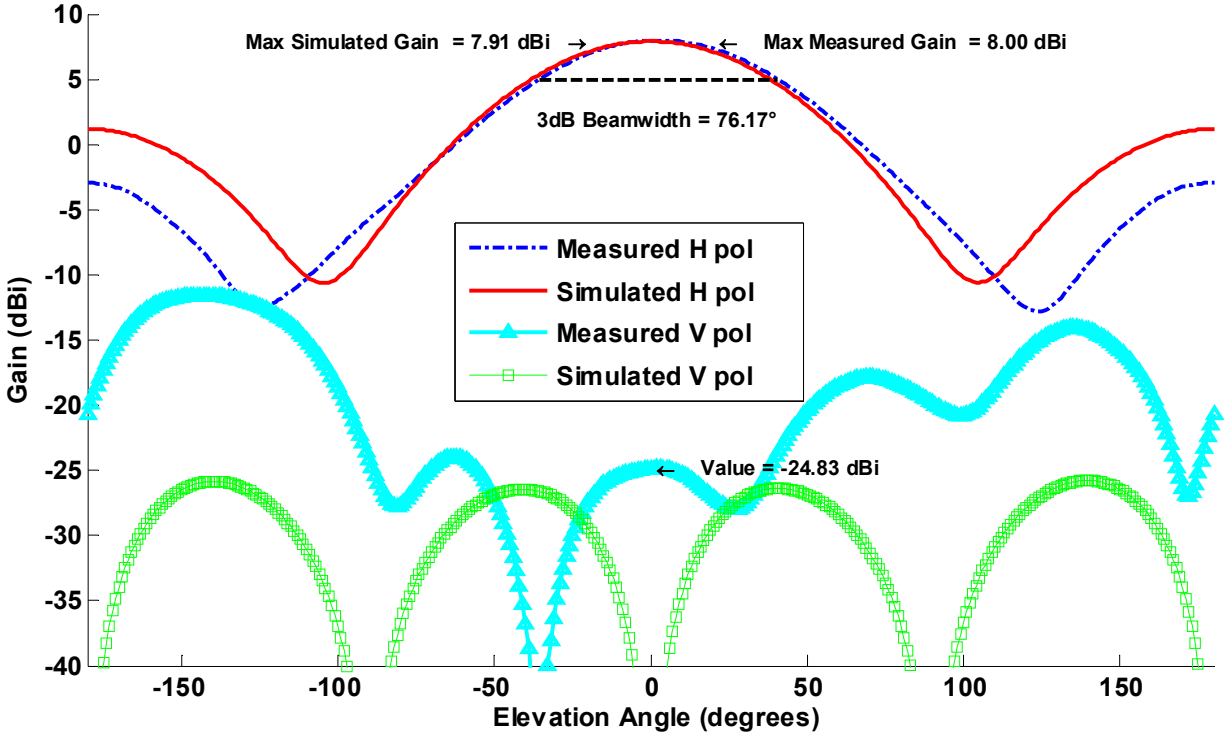

Fig. 3-18 Elevation pattern of the horizontally polarized 1 GHz antenna with ground reflector at λ/8.

The measurement of the 2 GHz array was also performed to determine the effect of the aluminum reflector on the pattern gain. Since the 2 GHz array is comprised of 4 elements, all of the ports must be tested. One solution is using a four way power divider to determine the combined pattern with unity excitation. Upon review of data from this exercise it was concluded that the 4 test cables driving each port were poorly matched leading to an irregular main beam pattern. The alternative was to measure each of the 2 GHz antenna array elements independently and preserve the coherent pattern data for synthesis in post processing. The exercise required four measurements on two polarizations for the antenna alone and with the reflecting ground plane. Due to the amount of collection required only the azimuth axis was scanned on the cylindrical pedestal limiting the available elevation data to ±60°. The azimuth and elevation pattern measurements for the loop alone and with the aluminum reflector at λ/4 (2 GHz) height are shown in Figs. 3-19 and 3-20 respectively. A gain increase of 2.2dB was realized by including the reflector and the backlobe has been reduced by more than 10dB. The presence of the large second lobe in the elevation scan is principally due to the test stand beneath the antenna. Since the vertical raster of the cylindrical scan is limited, this truncation of the data leads to greater inaccuracy as the pattern approaches -60° and +60°.

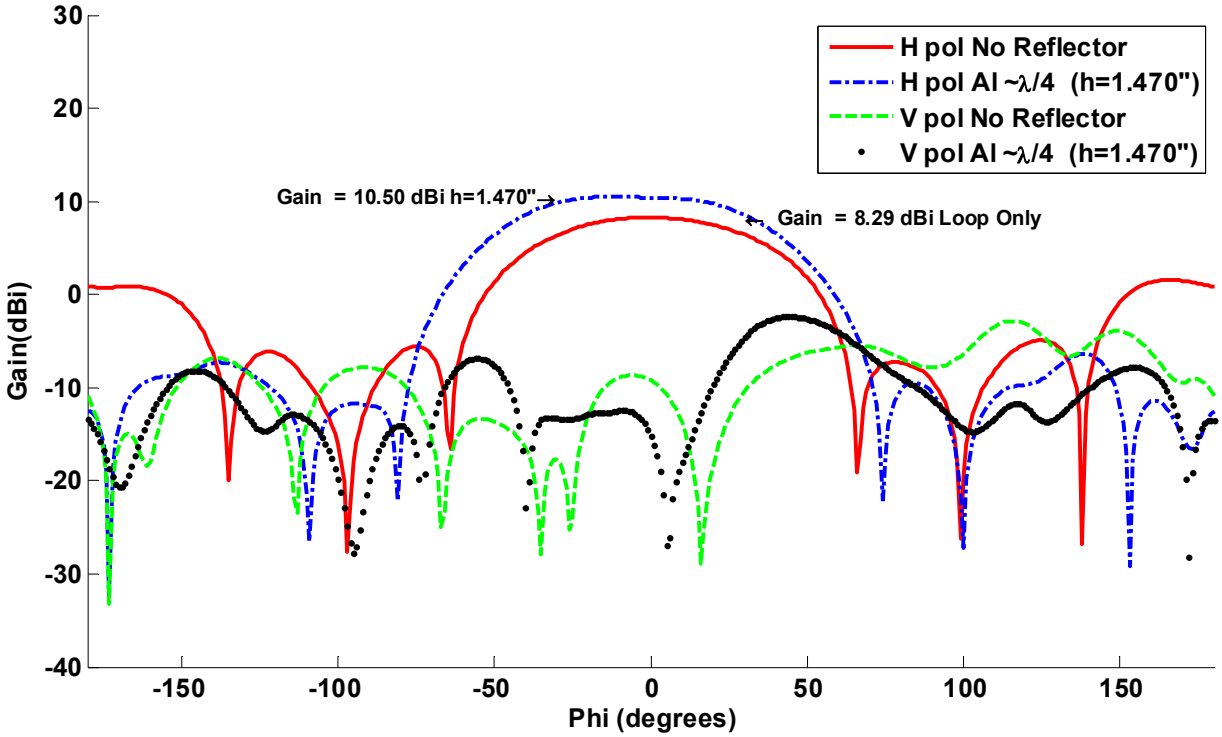

Fig. 3-19 Azimuth pattern of the 2 GHz array with and without ground reflector at λ/4.

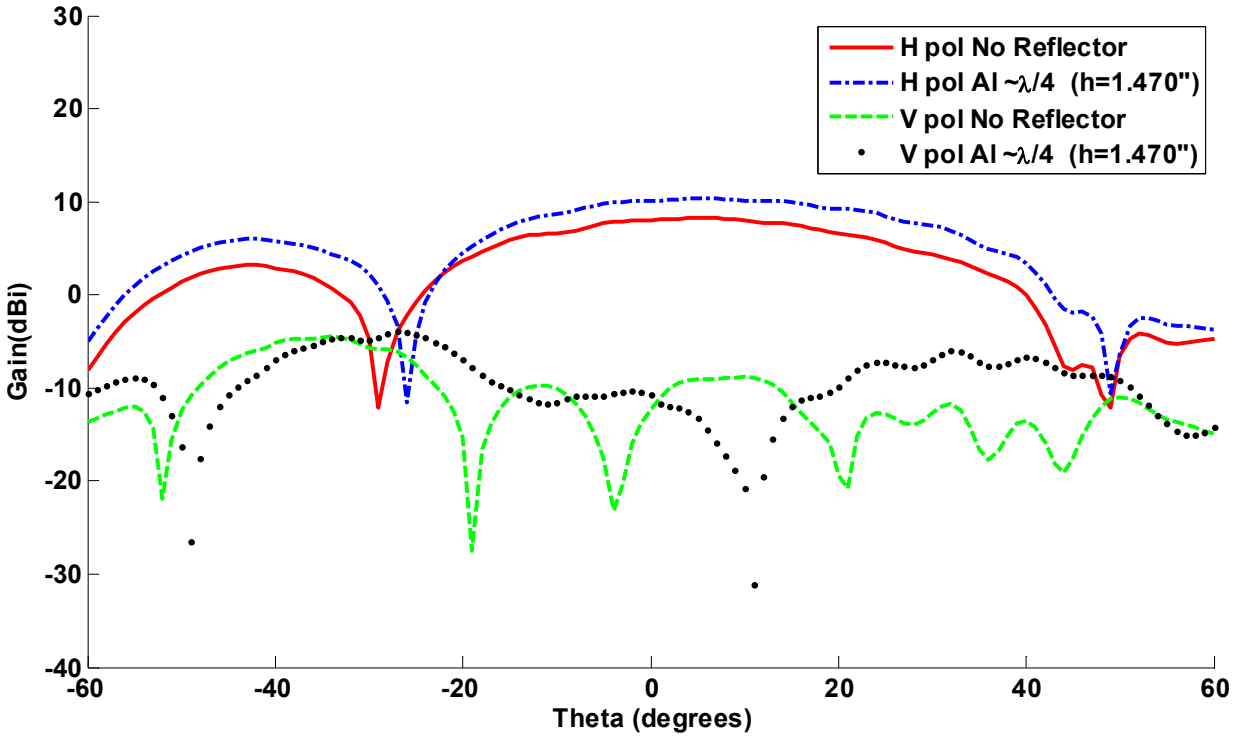

Fig. 3-20 Elevation pattern of the 2 GHz array with and without ground reflector at λ/4.

The pattern gain enhancement as a result of the reflecting plate has been shown to improve the antenna performance albeit at the cost of increased overall thickness. The fact that the reflecting surface must be placed a fractional distance proportional to two different wavelength requires special design consideration. The small shift in resonant frequency of the $\lambda/8$ case along with minimal decrease in bandwidth and beamwidth are acceptable tradeoffs for the 75mm of height reduction in the overall design. The study of the $\lambda/8$ case will be continued as a comparison case with the low profile design developed in Chapter 4.

CHAPTER 4

LOW PROFILE ANTENNA DESIGNS USING HIGH IMPEDANCE SURFACES

4.1 Artificial Ground Planes

Magnetic conductors do not exist in nature but their characteristic behavior can be artificially created when electrical conductors and dielectric bodies resonate under special conditions. The use of mushroom or thumbtack shaped structures over a substrate material with ground backing is a common example [8-10]. These structures use the parallel capacitance and inductance within the lattice to produce an LC resonance. The principal advantage of this design over corrugated surfaces is that they are much thinner than the λ/4 needed for resonance, thus reducing weight and bulk as well as providing high wave impedance in all directions. The scattering properties of the surface are also significant. Electric conductors reflect incident waves with a polarization inversion so the phase of the reflection is shifted by 180 degrees. When an antenna is placed close enough to an electric conductor, the boundary condition at the surface forces tangential electric fields to be zero and effectively shorts out the slot antenna. A tuned artificial magnetic conductor (AMC) has the same properties as the magnetic conductor so it produces in-phase surface reflections. The significance of this property is that the antenna can be placed adjacent to the AMC without shorting the electric field and any reflected power combines constructively with the incident radiation to increase the gain. For the loop antenna with tangential electric field, the overall height of the radiating structure that would be λ/4 over an

electric ground plane or corrugated surface can now be placed only several hundredths of a wavelength over the AMC surface.

4.2 Surface Wave Propagation

The high impedance surface (HIS) is characterized by a bandgap in which both TM and TE bound surface waves are suppressed [9]. For inductive materials such as metals the TM propagation mode has an infinite cutoff frequency and propagates at the velocity of light. The propagation of TE polarized surface waves are limited to only capacitive surfaces and therefore are not supported on bare metals. However, the addition of a dielectric layer over the metal will support TE propagation modes above a cutoff frequency which depends on both the permittivity and thickness of dielectric medium. For the electronic band gap (EBG) structure the infinite cutoff of the TM propagation over metal follows the light line until it reaches resonance. The light line refers to the group velocity of propagation in the medium and will be later explained in the context of the dispersion diagram. Attenuated propagation is indicated when the slope diverges from the speed of light. Upon reaching the resonance of the TM cutoff, the surface waves become trapped in the LC resonators resulting in a very low group velocity. The TE propagation continues to be supported, however, the cutoff frequency of this mode is beyond the lower cutoff of the TM suppression. The suppression of propagation that occurs in this frequency region is referred to as an electronic bandgap. The TM and TE polarizations form the first two propagating modes for the HIS structure and will be the subject of subsequent numerical studies.

4.3 Analysis Techniques

A variety of analytical and numerical techniques exist to analyze the surface wave propagation over the high impedance surface each with unique benefits. Analytical formulations based on the equivalent surface impedance provide additional insight into the electrical behavior

of a structure. Numerical solutions based on full wave electromagnetic solvers can provide greater accuracy and are adaptable to many complex geometries. The approximation of the surface resonance is a critical first step in the design process and many derivations for simple geometries can be found. The HIS geometry presented in Fig. 4-1 consists of a single board with two metalized layers. The top layer contains a periodic grid of metallic patches attached by vias to a ground plane on the lower layer. The gap between the patches is capacitive while the metallic path length through the structure between them is inductive.

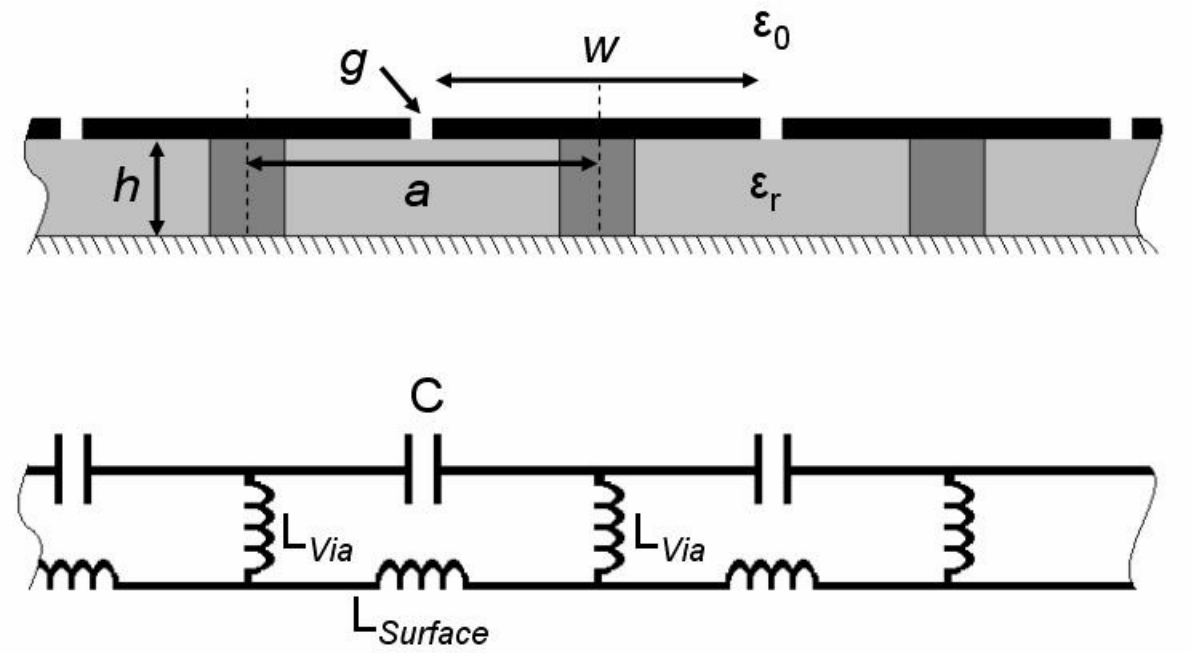

Fig. 4-1 Geometry of thumbtack EBG surface with equivalent circuit.

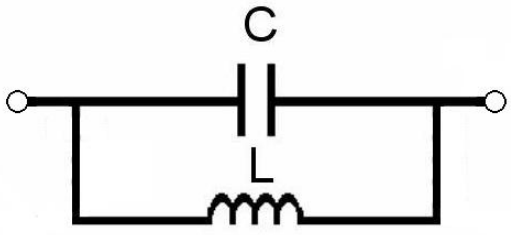

Fig. 4-2 Equivalent circuit for surface resonance.

The effective surface impedance model [9] uses the bulk capacitance and inductance of the media to determine surface impedance at resonant frequency as

$$Z_s = \frac{j\omega L}{1-\omega^2 LC} \tag{4-1}$$

$$\omega = 2\pi f = \frac{1}{\sqrt{LC}} \tag{4-2}$$

The approximation of L and C in Fig. 4-2 can be made using

$$C_{fringe} \approx \frac{w(\varepsilon_0 + \varepsilon_r)}{\pi} \cosh^{-1}\left(\frac{a}{g}\right) \tag{4-3}$$

$$L = \mu t \tag{4-4}$$

where the width w, gap g, and lattice constant a along with the permittivity dominate the capacitive parameter. The C_{fringe} term proposed was derived using analytical techniques and therefore only serves as a first order (quasi-static) approximation of the capacitance in the initial design. The only parameter that remains is the thickness t of the board to influence the inductance. While this model is useful for establishing an initial design operating at a specific resonance, it is not capable of predicting the actual bandgap for the structure. Furthermore, the need to explore more sophisticated geometries requires numerical full wave solvers. Another modeling technique is based on using the reflection phase of the surface [10]. The HIS at resonance produces no phase shift in the reflected wave. Therefore, a study of reflection coefficient of the material can be an aid in bandgap prediction. Ansys HFSS [14] a commercial finite element solver can perform Floquet port analysis of a unit cell of the material. This allows the surface impedance and reflection parameter to be de-embedded at the material surface. At normal incidence a PEC surface will result in 180 degrees reflected phase and for the HIS at resonance the reflection will be 0 degrees. Consequently, the edges of the TM and TE band gaps

correspond to phase reflection between -90° and +90°. This can be an effective predictor of the unit cell bandwidth for a wide range of geometries [15]. Experimental procedures can also be used to determine the transmission characteristics over the surface. In the absence of computational resources, the transmission for both TE and TM propagation can be made by creating two samples. One will be entirely PEC and serves as a base line, while a second structure with HIS is measured to determine the suppression compared to the PEC case. Another experimental method is to use suspended microstrip that uses the HIS surface as ground medium [16], although this technique only predicts the bandgap and not the behavior of TM nor TE independently. The only technique capable of determining the surface wave modes is the eigenmode analysis within a full-wave solver. Using HFSS to analyze a unit cell with periodic boundary conditions, the first two modes of propagation within a Brillouin zone [17] can be determined. In a periodic medium the Brillouin zone represents the minimum region in which characteristic properties of the wave exist. The eigenmodes computed by this solution are harmonic and represented in terms of their phase velocity. By varying the phase gradient of the Bloch boundary conditions from 0° to 180° phase along the three axes of the Brillouin zone a complete characterization can be made. Figure 4-3 describes the orientation of the vectors. The dispersion diagram will combine the resulting eigenvalues by concatenating the results from $\Gamma \rightarrow X$, $X \rightarrow M$, and $M \rightarrow \Gamma$.

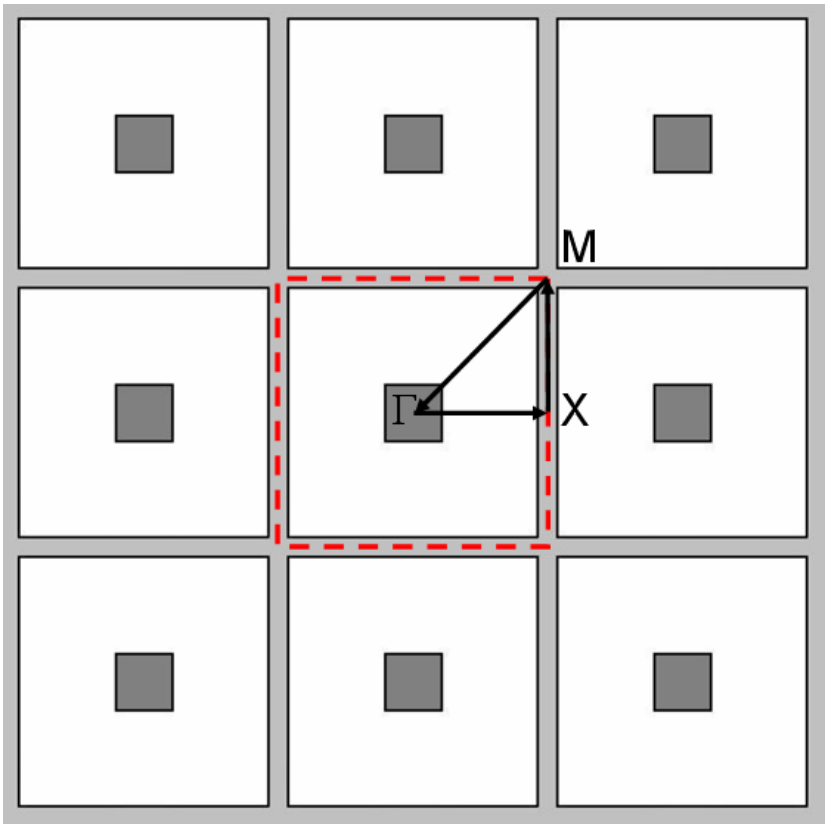

Fig. 4-3 Brillouin region and propagation vectors within the EBG unit cell.

Finally, the results are post processed and displayed in a dispersion diagram. The maximum frequency of TM propagation determines the lower bound on the bandgap while the minimum intersection of the TE propagation and the light line form the upper bound. The light line corresponds to the group velocity $\omega\sqrt{\mu\varepsilon}$ in the medium that bounds the phase velocity of the individual eigenmodes. Figure 4-4 contains a dispersion diagram of the TM and TE propagation from eigenmode analysis. The grey portion of the graph corresponds to the electronic band gap between the two propagating modes. A bandwidth of 4.42 GHz is predicted for this design.

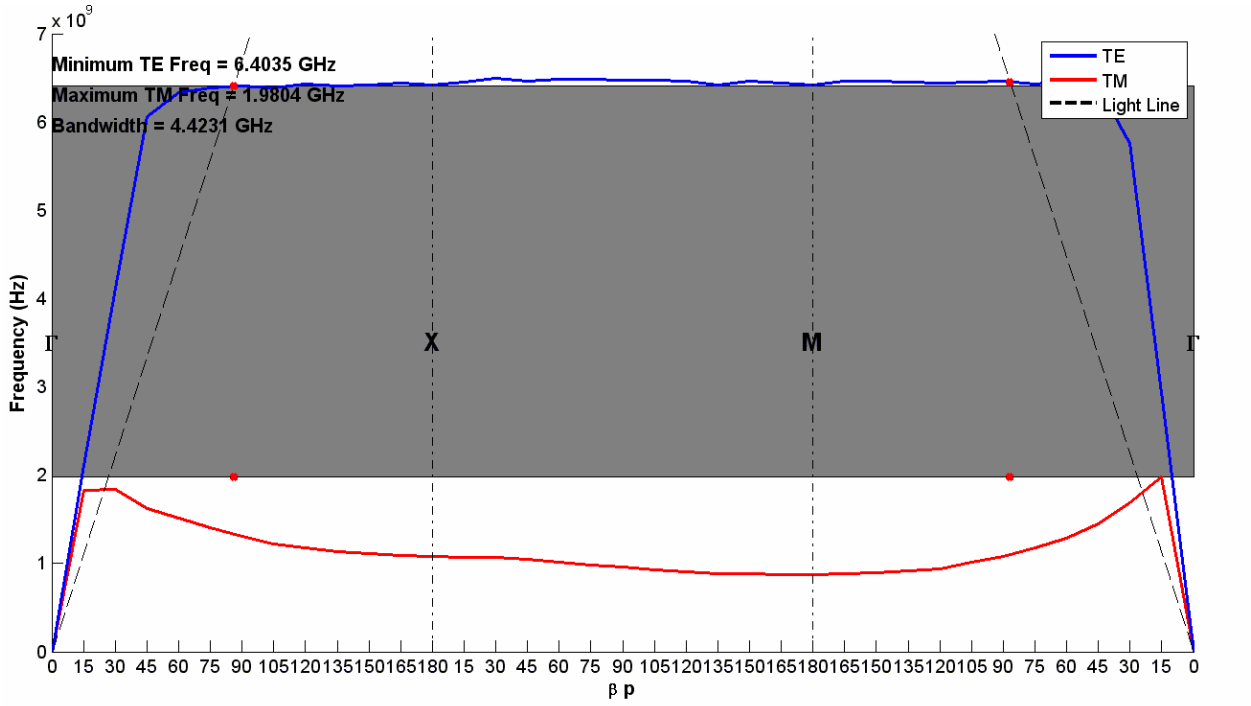

Fig. 4-4 Dispersion diagram for TE and TM propagation.

4.4 Design of High Impedance Surface

The design procedures for low frequency HIS require special considerations. The capacitance required to support the low frequency resonance is high. The increased capacitance can only be produced by greater element overlap. Extending the resonance to lower frequencies ultimately requires multiple layers of overlapping elements which adds additional thickness, weight, and cost. The resonance prediction of the effective surface impedance model shows that to decrease the frequency of the surface the capacitance and inductance must increase. The inductance can be increased by using a thicker substrate however this is undesirable. One alternative is to use a coplanar spiral inductor capable of resonance in structures as small as $\lambda/40$ for substrate reduction [16]. The exploration of this design is one potential method of reducing the thickness of the antenna structure.

4.5 Integration of High Impedance Ground Plane with X-band Slot Antenna

The design of the lower frequency HIS has inherent challenges related to both the manufacturing and test costs. Therefore, an EBG surface operating in X-band was preferred starting basis for experimentation due to limitation of the anechoic chamber, availability of the WR90 waveguide adapters, and physical size of the tested samples being smaller at high frequency. A fabricated HIS and antenna were produced for resonance at 10.5 GHz based on the surface equivalence model. The photo shown in Fig. 4-5 is a hexagonal EBG surface with dimensions labeled.

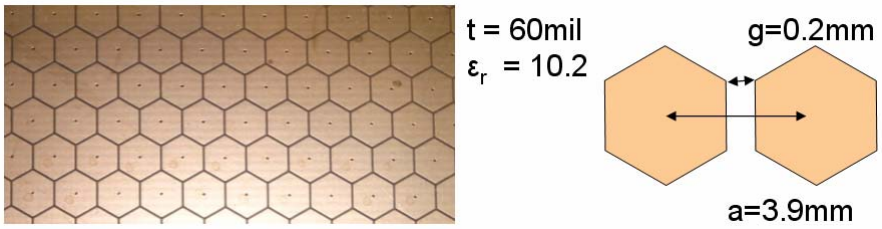

Fig. 4-5 Hexagonal EBG surface and dimensions.

The reflection of a wave with normal incidence is determined by loading a WR90 transmission line with a sample and observing the reflection from open, short, and both orientations of the hexagonal surface. Figure 4-6 shows the HIS sample as the termination of the waveguide.

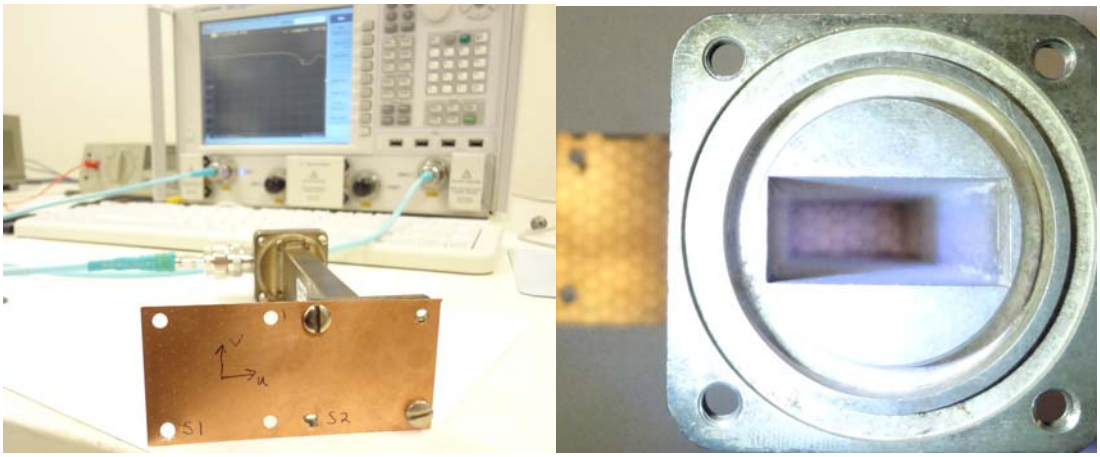

Fig. 4-6 Waveguide sample measurement setup.

Since the lattice is hexagonal the propagation should be measured in the three propagation directions of the Brillouin zone. For these measurements only the two principal Cartesian axes were considered and are described in Fig. 4-7. The E field of the WR90 waveguide was oriented in four measurement positions corresponding to $+\hat{u}$ and $-\hat{u}$ in the horizontal and $+\hat{v}$ and $-\hat{v}$ in the vertical to observe any changes in surface reflection properties.

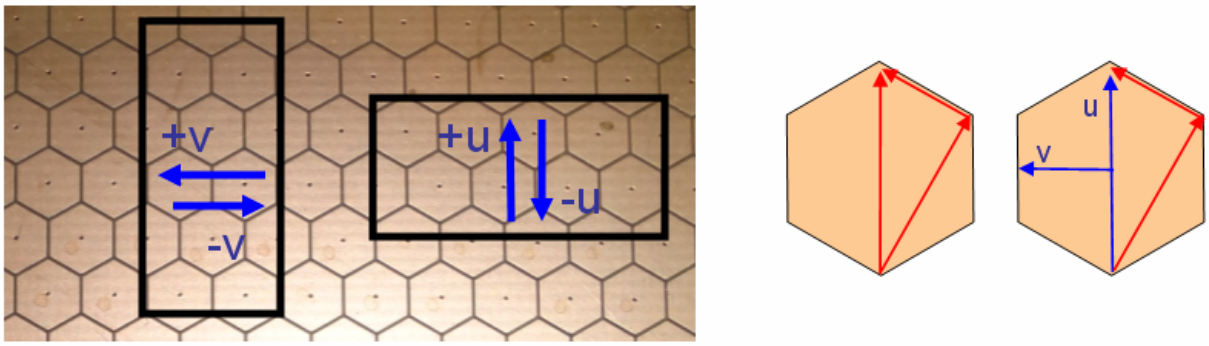

Fig. 4-7 Measurement axes of the reflection coefficient.

The magnitude of the reflected wave is shown in Fig. 4-8. The shorted waveguide shows a high reflection as expected. Likewise, the open condition has very little reflection. The figure also shows the reflection of the HIS responds to the $\hat{u}$ and $\hat{v}$ orientations differently and shifts the resonance as polarization vector is rotated. The presence of the HIS resonance is indicated by the low reflection seen between 11.0-11.5 GHz. The short condition was then used to determine the reflected phase of the HIS de-embedded to the surface. When the phase of the HIS is plotted in Fig. 4-9 it shows almost 0 degrees of reflected phase at 11.04 and 11.23 GHz which confirms the presence of the electronic bandgap in the surface. Furthermore, the lack of reflected energy at these frequencies demonstrates the EBG has achieved resonance.

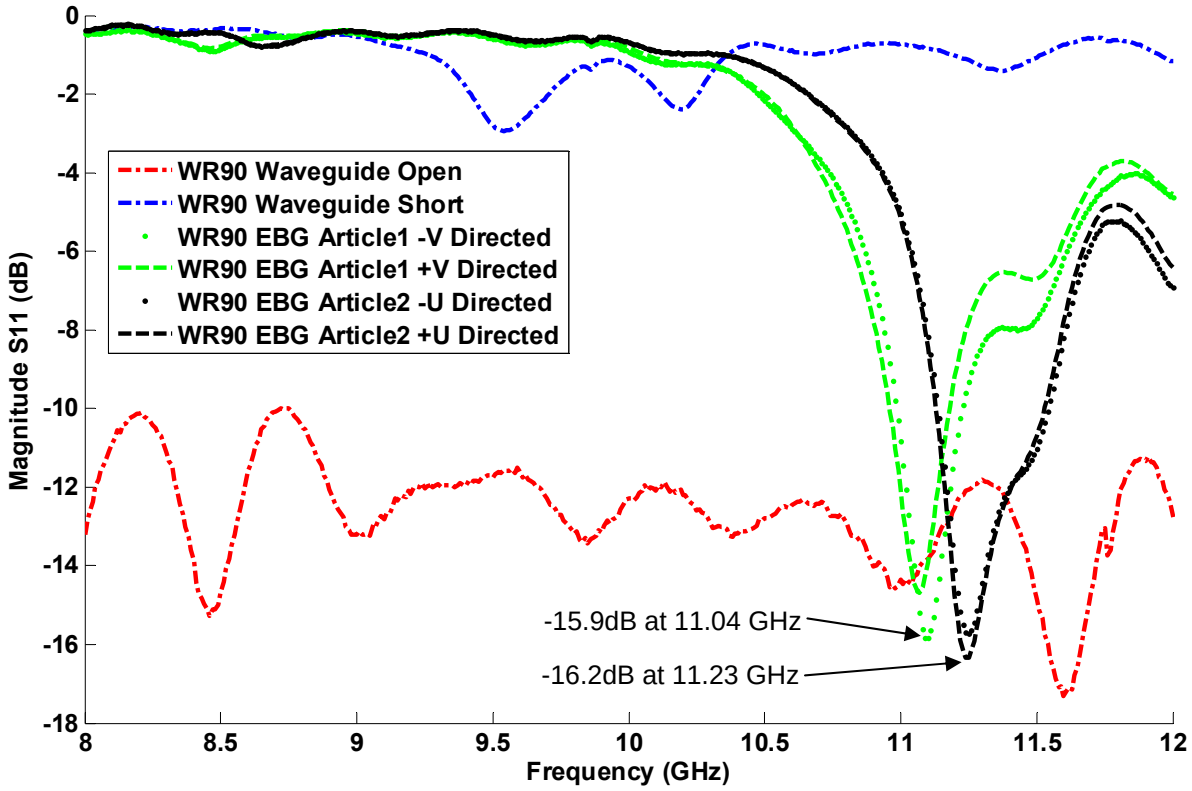

Fig. 4-8 Measured magnitude of S11 vs. frequency for the HIS terminations.

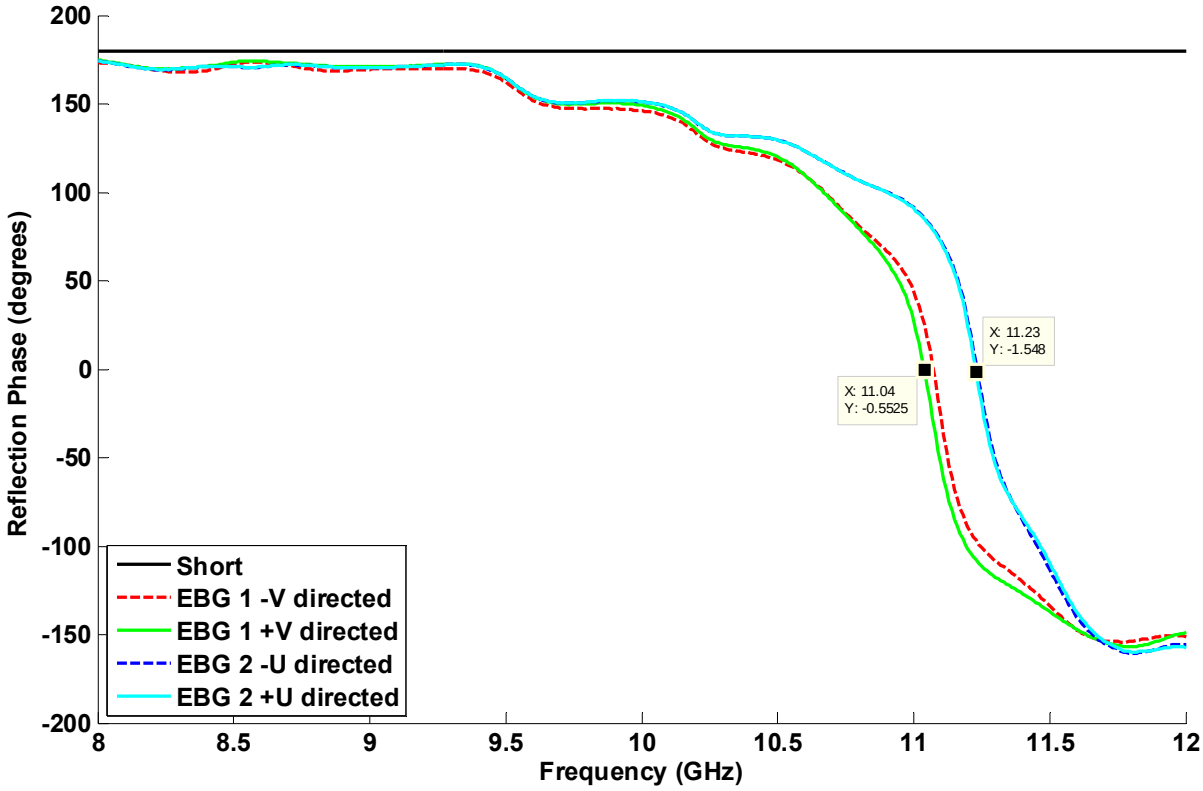

Fig. 4-9 Measurement of de-embedded phase of S11 vs. frequency for EBG terminations.

The loop antenna shown in Fig. 4-10 was fabricated concurrently with the EBG test sample in the previous test based on the predicted resonance of the HIS and prior to the waveguide termination experiment. The center frequency measured without HIS loading was 10.7GHz. The reflection coefficient was then measured for the antenna in air with no surroundings. Next, the antenna was loaded with the HIS surface from below to determine the effect as separation distance was reduced. The mechanical setup shown in Fig. 4-11 allowed the adjustment using dielectric screws.

Fig. 4-10 Slot loop antenna on microstrip substrate.

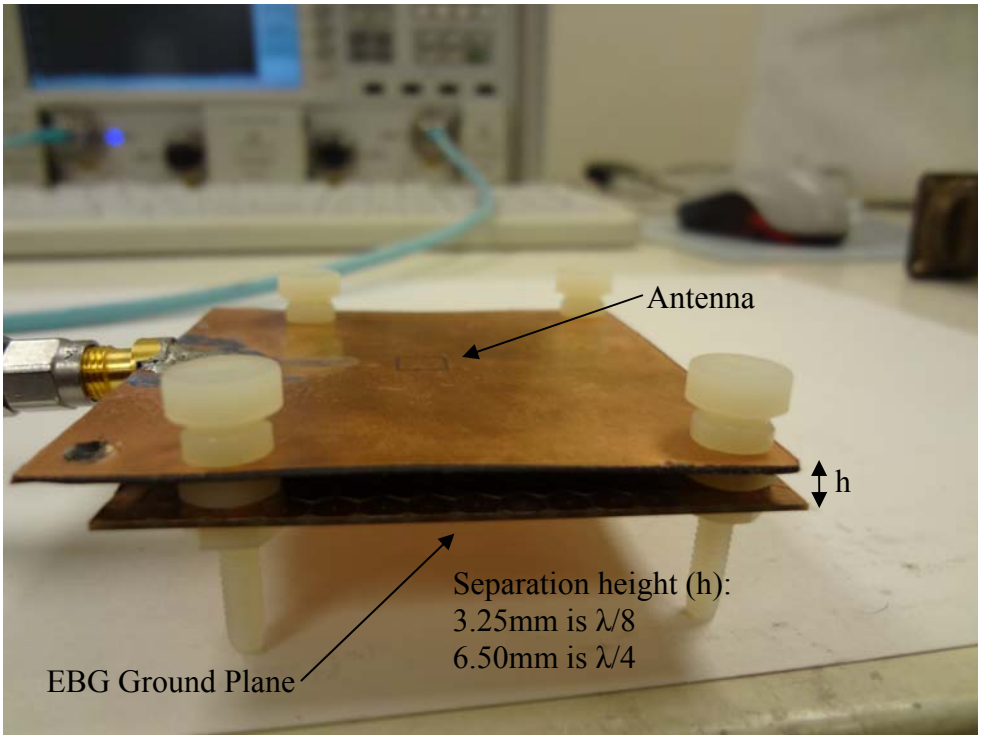

Fig. 4-11 Measurement setup to determine loading effects.

The effect of moving the EBG ground plane closer to the structure is illustrated in Fig. 4-12 which shows an increase in loop resonant frequency as the surface height is reduced. For the

0.07mm separation case a thin piece of paper was inserted to prevent a short with the microstrip line. The added paper will contribute a small amount to the capacitance, but the loading of the microstrip line with the HIS is causing the field disruption and input mismatch.

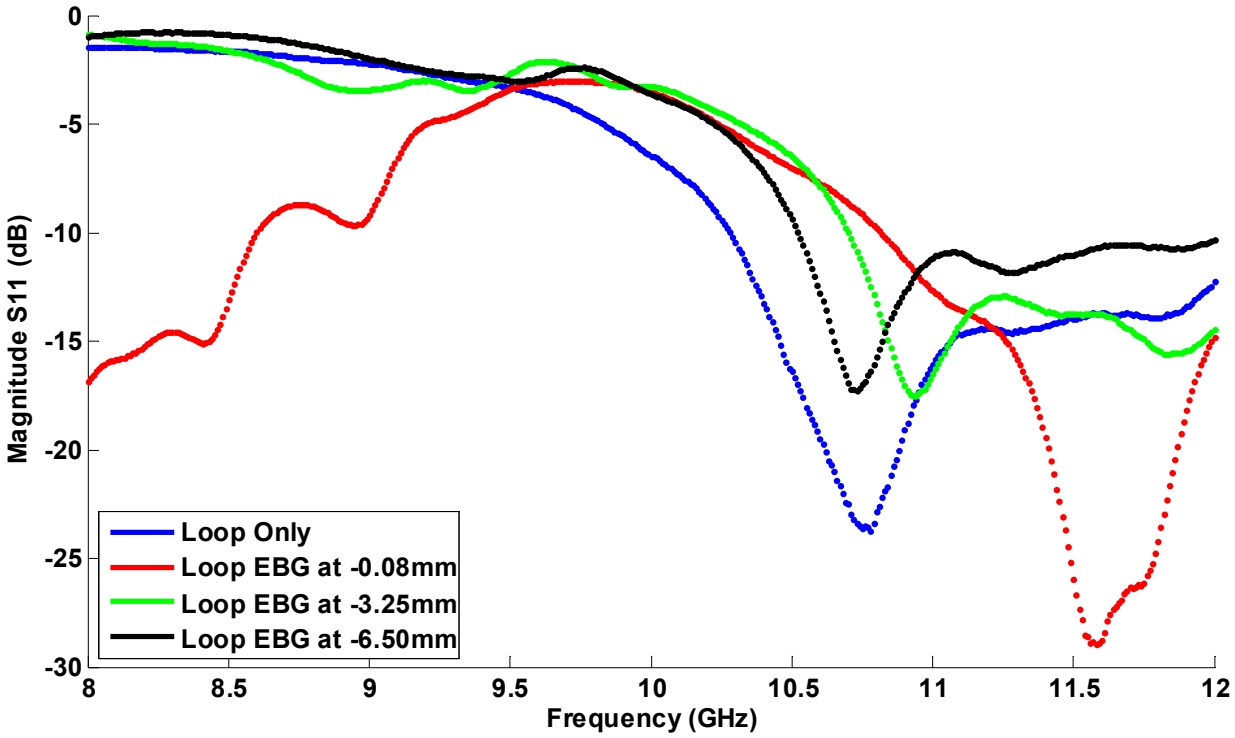

Fig. 4-12 Measurement of reflection versus frequency for loaded conditions.

Loading the slot loop antenna with the HIS shifts the resonance upward, so the antenna was redesigned to resonate at 11.3 GHz to fall within the EBG bandgap. The second antenna design iteration was measured and the results are shown in Fig. 4-13.

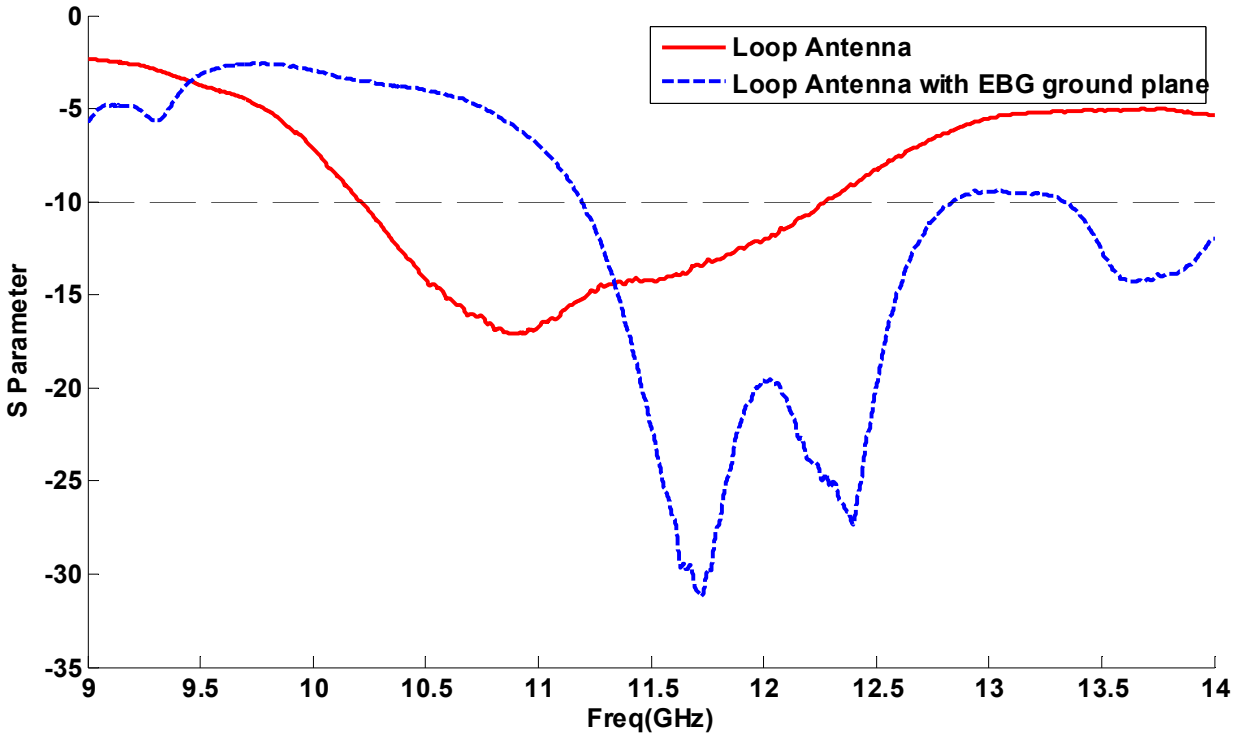

Fig. 4-13 Measured reflection versus frequency for HIS loaded antenna.

The following measurements were performed on Georgia Tech Research Institute's 1300' outdoor test range at the Cobb County Research Facility which is primarily used for measuring high gain antennas. The low gain of the antenna and multipath introduced from the environment and pedestal creates the measurement noise on the patterns. The measurement setup is shown in Fig. 4-14.

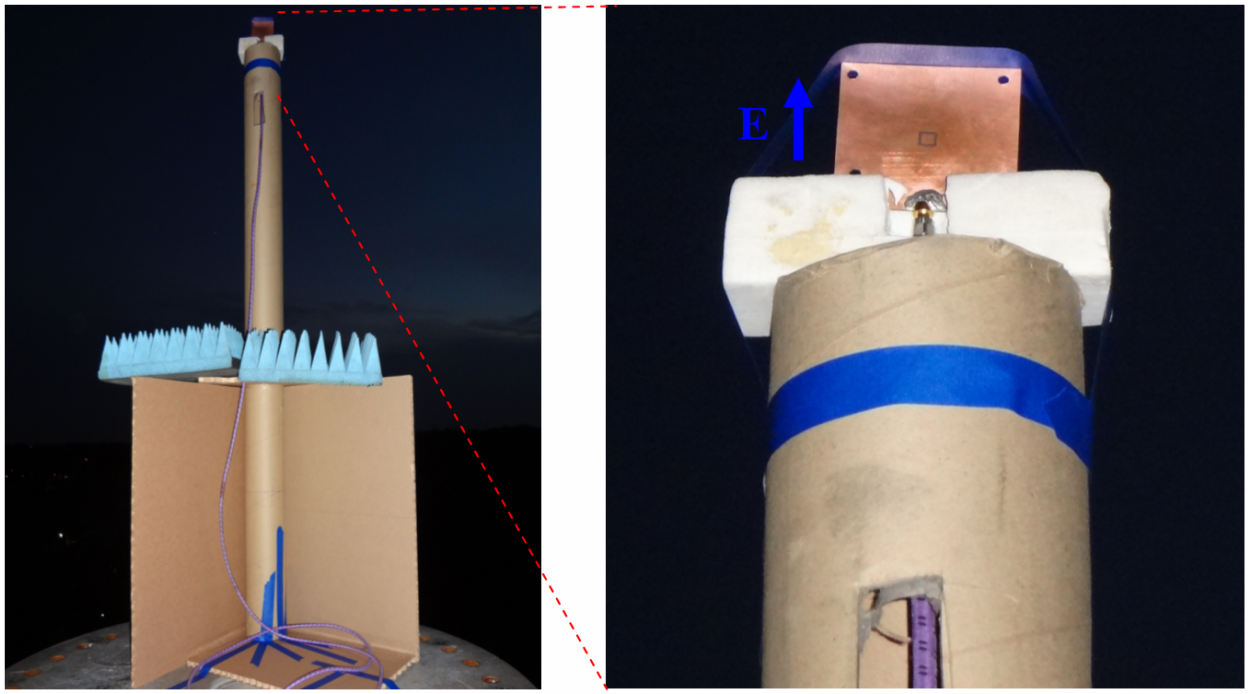

Fig. 4-14 Slot antenna with high impedance ground plane on test pedestal.

The H-plane pattern of the antenna was measured using a vertically polarized source and calibrated setup. The pattern labeled “Loop Only” in Fig. 4-15 indicates the dominant radiation from the slot occurs at -180° which corresponds to the bottom side of the loop and where the stub feed is located. The second case labeled as “Loop with EBG” introduces the EBG ground plane on the same side, covering the microstrip line, and reducing radiated gain in the -180° direction. It is evident that the EBG ground plane reduces the backlobe radiation from the loop with increased forward radiation. However, the efficiency of the antenna is reduced in part from the close proximity of the EBG ground plane to the antenna feed.

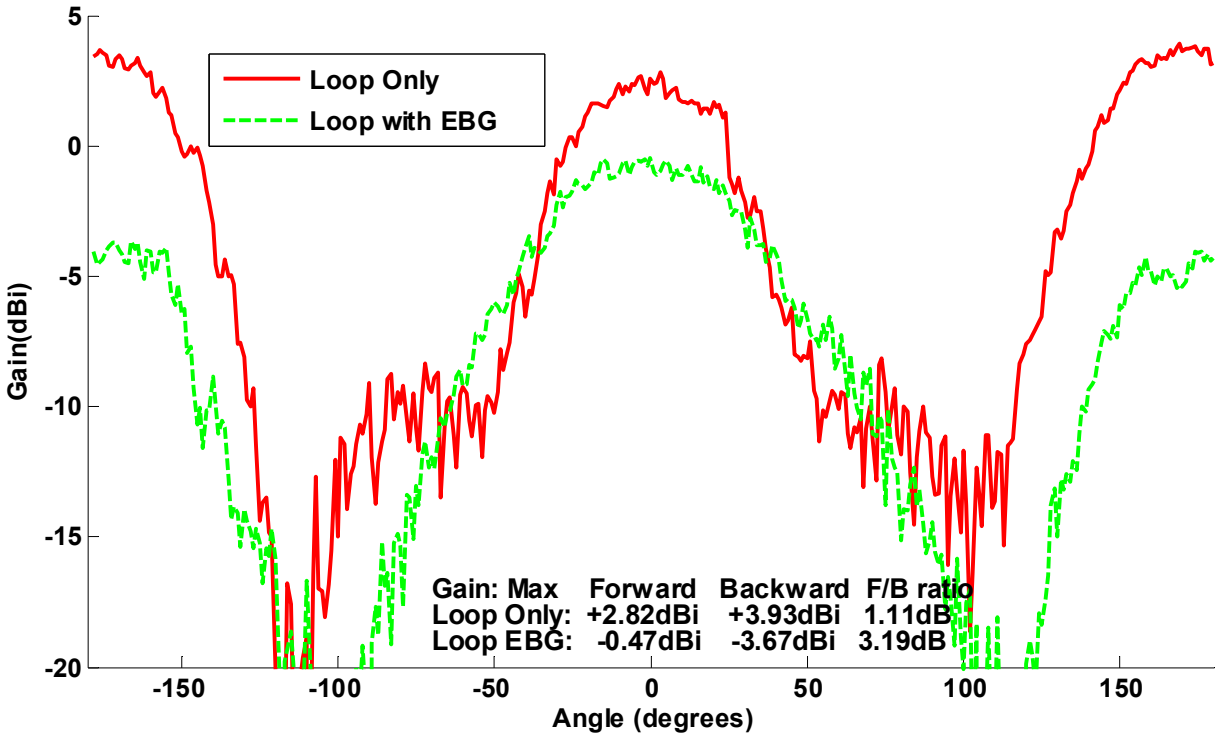

Fig. 4-15 H-Plane cut for antenna with and without EBG surface (azimuth) at 11.3GHz.

The close proximity of the EBG to the microstrip line and stub feed distort the fringing fields which increases the impedance resulting in transmission mismatch. Future antenna design analysis will address these concerns by placing the microstrip stub feed on the top half of the loop to avoid interactions with the HIS.

The conclusions drawn from this experiment show that the EBG can be designed for operation at X band. The addition of the EBG medium did not show an overall increase in forward gain compared to the loop case alone, but it did demonstrate the property of the EBG to reduce backlobe radiation by reflecting the energy forward as evidenced by the wider main beam. These techniques were then applied to scale the design to the lower frequencies in subsequent sections.

4.6 Low Frequency Artificial Ground Planes

The resonant behavior exhibited by the artificial magnetic surface is the result of capacitive and inductive elements present within the structure. According to the first order model in Eq. 4-2 the frequency can only be reduced if the capacitance or inductance is increased. The capacitance can be increased by expanding the overlapping area of the cells allowing greater fringing of electric field but will require larger unit cell dimensions. Consequently, the lower aspect ratio and increased size makes characterizing the material more difficult due to the larger proportion of the unit cell size relative to the antenna element. The desire to produce a HIS that functions at both 1 GHz and 2 GHz is a significant challenge with no known literature covering the topic. Therefore, this section will outline existing technologies potentially capable of dual band operation.

High impedance surfaces operating at low frequency have been designed for operation at 1 GHz but require thick low loss foam substrates to increase the inductance. One benefit of the additional thickness is increased bandwidth. A notable example can produce a ±90° reflection bandwidth of 665 MHz operating from 882 MHz to 1.547 GHz [18]. The design has the unit cell dimensions of 10.7mm x 10.7mm and is constructed on a foam dielectric with a thickness of 30.5mm. The cell gap dimension was not reported but the capacitance of 0.47pF was used to calculate the 0.01mm separation. HFSS was then used with the Floquet port solver and periodic boundary conditions to reproduce the reflected phase of the design. The result of the computational analysis is shown in Fig. 4-16 and labeled “Simulation.” The corresponding measured data of the design reported in [18] is also shown and labeled “Measurement.” Since the design shows an appreciable bandwidth, it could potentially be extended to cover both the 1 GHz and 2 GHz resonances. The HFSS Optimetrics tool was then used to optimize the foam

thickness, cell dimension, and gap with the goal of maximizing the bandwidth. The optimized design shows both the 1 GHz and 2 GHz responses reside within the ±90° operational bandwidth. The reflection phase for this wideband design is shown in Fig. 4-16 and is labeled "Optimization." The results show that the 1.1 GHz bandwidth would be sufficient to use as a magnetic ground plane but the design remains very thick. The λ/8 ground reflector used in Chapter 3, by comparison, required only 37.5mm height and uses a simple aluminum plate. Using the thick material in its place would increase the bulk of the design and only potentially reduce its height by 7mm or 20%. Furthermore, at the ends of the operating band the reflected phase is no longer zero which reduces their efficiency. In practice an EBG exhibiting a 2:1 bandwidth is only realizable at higher frequencies where the TM mode can be suppressed sufficiently and the first TE mode has a very high cutoff frequency.

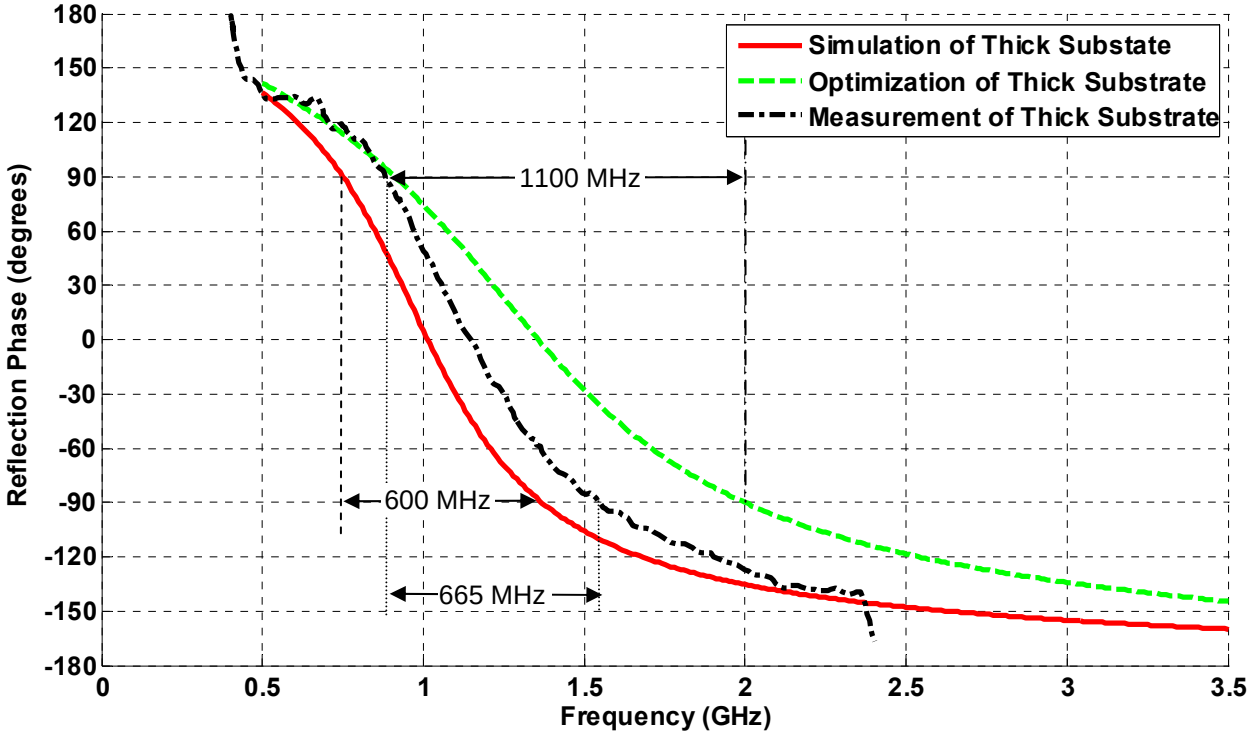

Fig. 4-16 Reflection phase versus frequency of surface with 30.5mm foam substrate [18].

Next, the focus was turned to reduction of the EBG substrate height. Simulations at various heights were performed to show the effect on the resonant frequency which coincides with the reflected phase of zero degrees. As expected the resonant frequency increased when the thickness decreased due to the loss of inductance. The full set of curves are shown in Fig. 4-17. The additional height is clearly necessary to produce the lower resonances. The 32mm substrate height case also shows the presence of a second resonance at 2.72 GHz. The presence of this resonance phenomenon can be exploited to produce a dual band EBG surface.

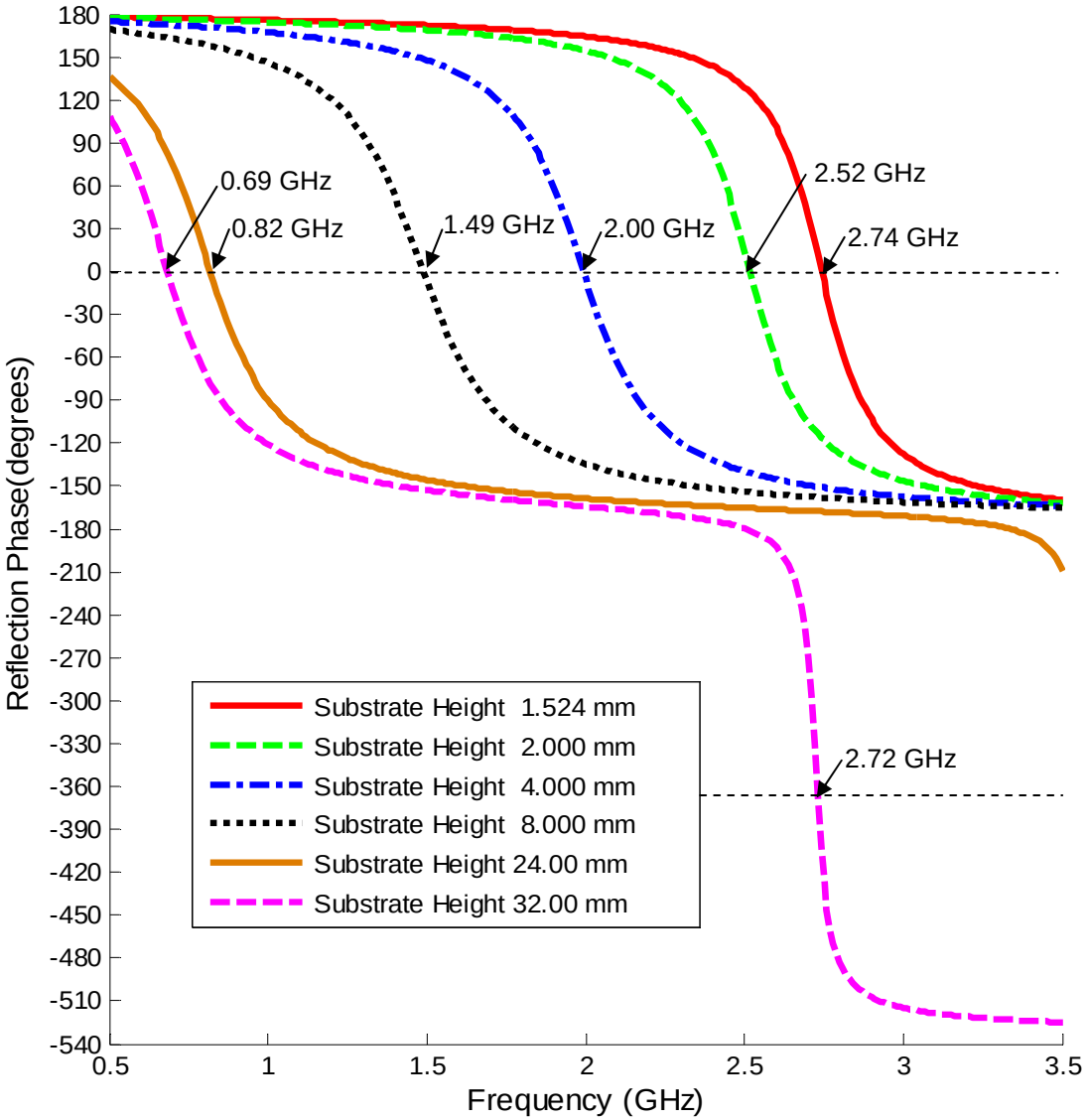

Fig. 4-17 Effect of ground plane height reduction on simulated resonant frequency.

4.7 Enhancement of Artificial Ground Planes

Planar capacitive and inductive geometries have several advantages that can be used to enhance the resonance of the HIS. The interdigitated capacitor shown in Fig. 4-18 provides greater surface overlap of the cell edge which increases the capacitance between the two structures. The finger width, length, and gap separation are variables that allow the capacitance to increase without expanding the unit cell dimensions [19,20]. This also can be used to minimize the cell size of the EBG such that an appreciable granularity (~λ/20) can be achieved. Coplanar spiral inductors are another element used to improve the design performance [16,21,22]. The element shown in Fig. 4-19 uses the spiral arm to increase the propagation path within the resonant circuit. This path length adds inductance between the capacitive cell edge and the via connecting into the ground plane. The addition of this spiral geometry can therefore be used to either lower the resonant frequency or reduce the substrate height by compensating for lost inductance. Since these coplanar technologies do not require the soldering of lumped elements onto the surface, the cost to manufacture is less and when used on thin flexible substrates can be used in a variety of conformal applications. The goal of the following exercise is to determine if the substrate height can be reduced for the 1 GHz HIS.

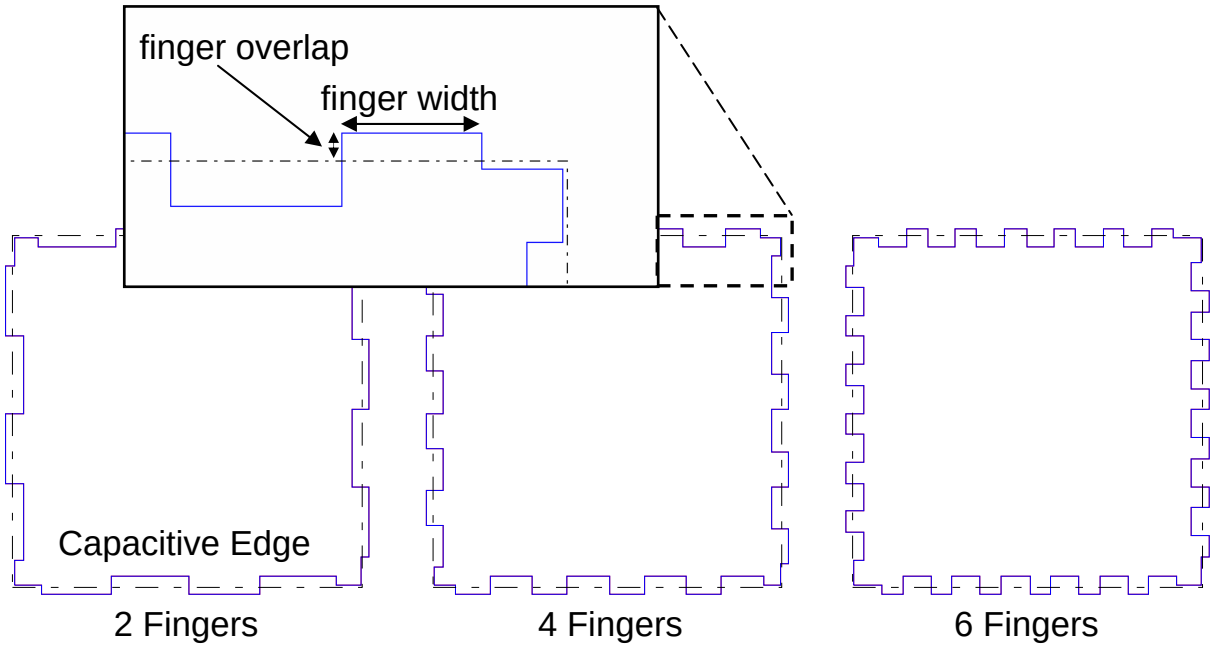

Fig. 4-18 Interdigital geometry for increasing capacitance.

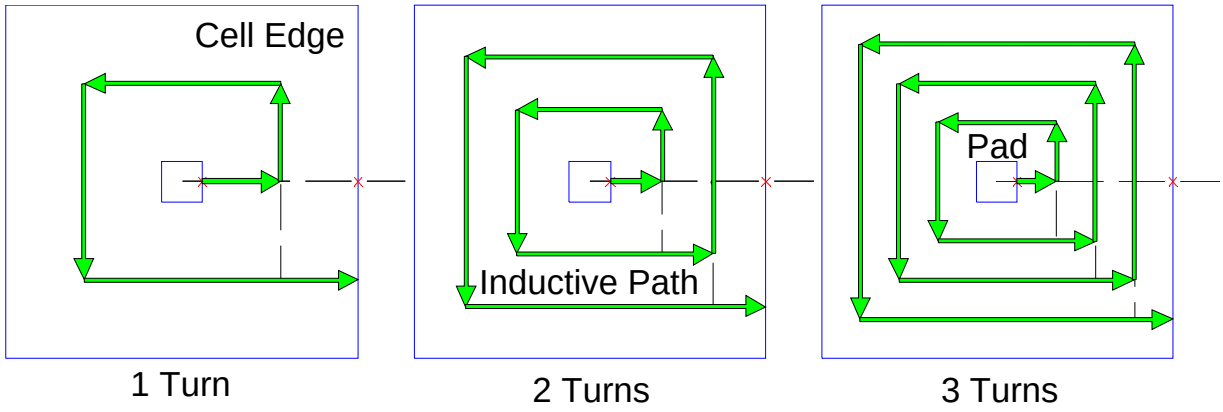

Fig. 4-19 Coplanar spiral geometry for increasing inductance.

The initial design reported in section 4.5 was created on the same Rogers Corp RO3035 material used for the antennas described in Chapter 3 using a 10.7mm unit cell dimension. The height of the substrate was reduced from 30.5mm to 1.524mm (60mils) and the gap size was increased to 4 mils which is the smallest gap that can be fabricated with available facility. The

four edges of the cell were then interdigitated with various numbers of fingers to determine the effect on the resonant frequency. The gap of 0.1016mm was retained and the finger width was set to 0.3mm with 2.2mm of finger overlap. Figure 4-20 summarizes the affect of increasing the number of fingers of the interdigitated capacitance (IDC). A frequency shift of almost 250 MHz is produced but was not substantial enough to create the desired 1 GHz resonance.

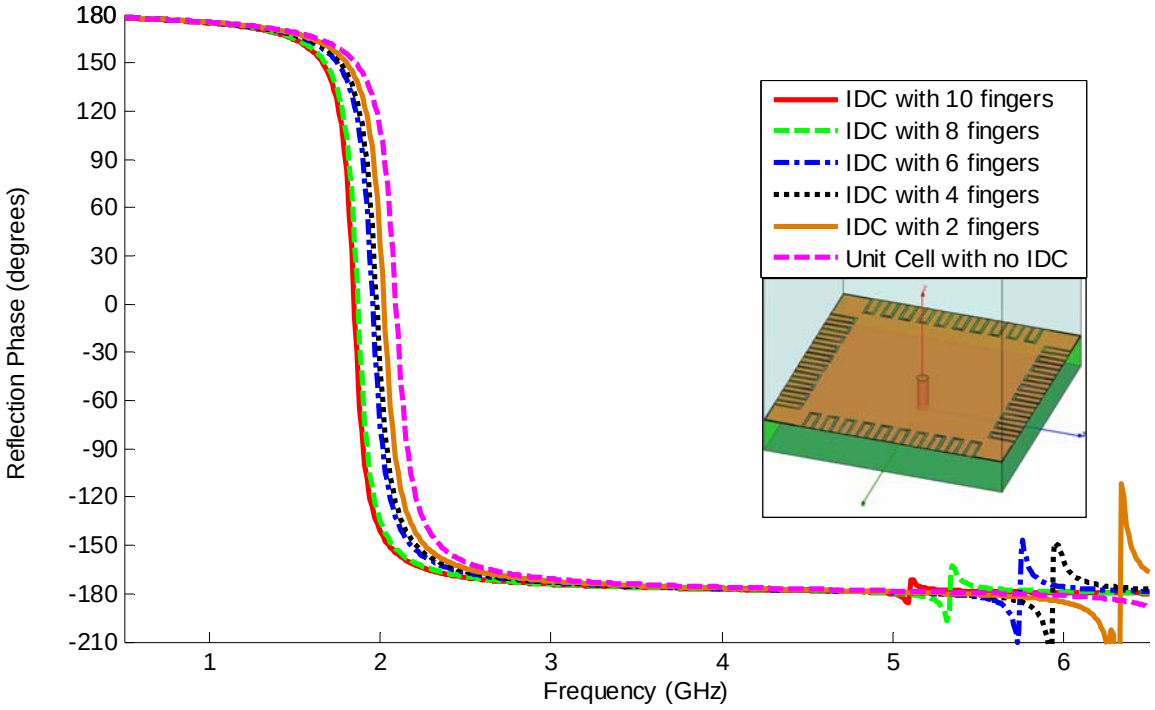

Fig. 4-20 Resonance shift of 10.7mm unit cell on 60mil RO 3035 material.

The coplanar spiral was then added to the inside of the design and manually tuned for 1 GHz response by varying the unit cell size, the interdigital capacitor parameters, and spiral geometry parameters. The best available design shown in Fig. 4-21 was for a cell dimension of 15mm with a 15 fingered interdigital capacitor and three turn inductive spiral. Unfortunately, the bandwidth of this design was small, thus the fabrication was not attempted. The complete design space containing 48 points is illustrated in Fig. 4-22 where the vertical axis represents the

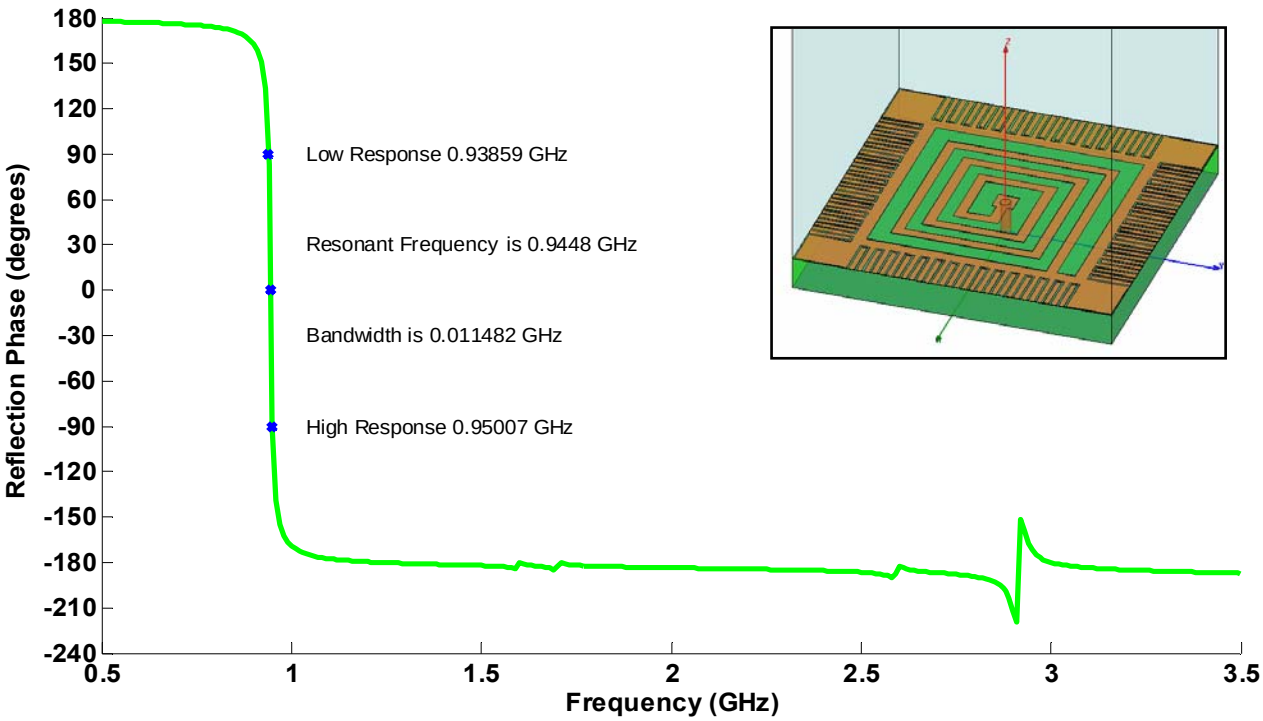

Fig 4-21 Reflection phase of the 1 GHz interdigitated EBG cell with coplanar spiral inductor.

bandwidth of the design and horizontal axis is the resonant frequency corresponding to a reflection phase of zero. The trend shows that as the resonant frequency decreases the operating bandwidth is narrowing.

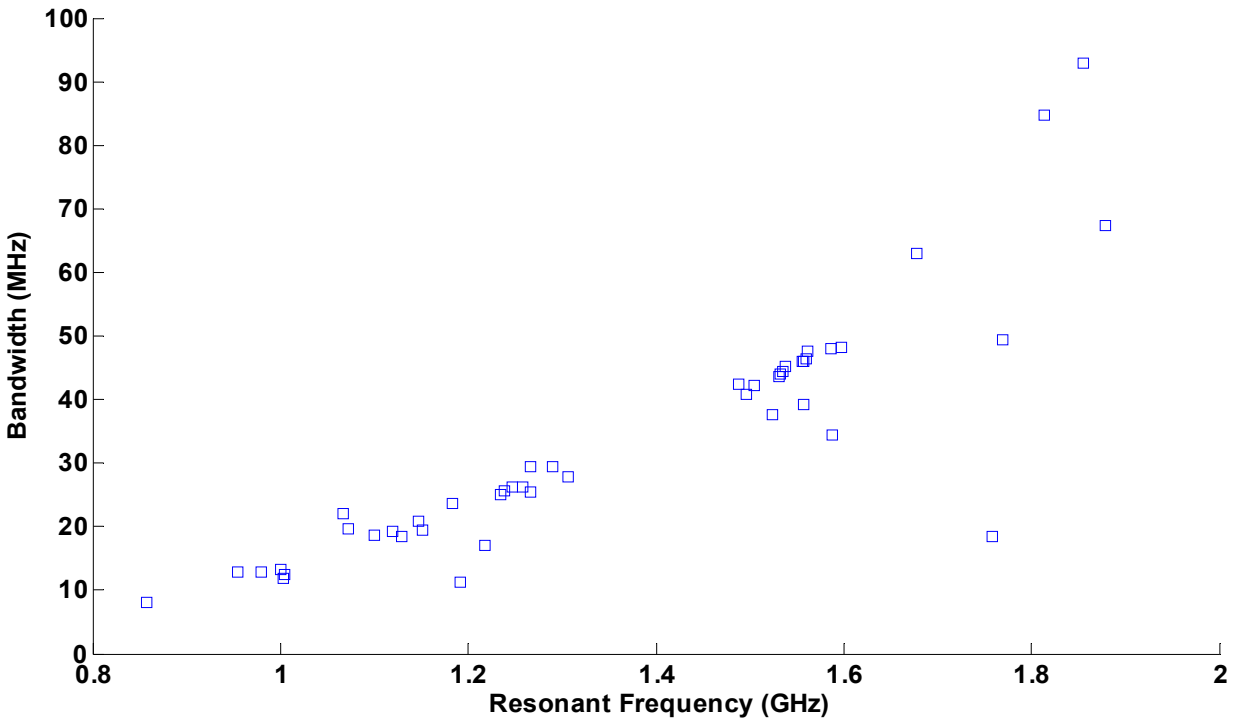

Fig. 4-22 Data constellation of the 1 GHz interdigitated EBG cell with coplanar spiral inductor.

The thin (60mil) substrate design was preferred because it utilizes the same RO3035 laminate used in manufacturing the antenna and could be easily created in the material stackup. However, the very narrow bandwidth made this impractical. Additionally, the desire to create an EBG with resonance at two distinct frequencies must be addressed. Therefore, a thicker Rogers Corp TMM10 material [23] measuring 6.35mm (250mils) was selected with a higher permittivity of 10.2 to extend the bandwidth. The design was then tuned for both resonances at 1 GHz and 2 GHz. Figure 4-23 shows a reduced data set in which the first resonance falls within ±50 MHz of the 1 GHz goal and the corresponding variation of the second resonance.

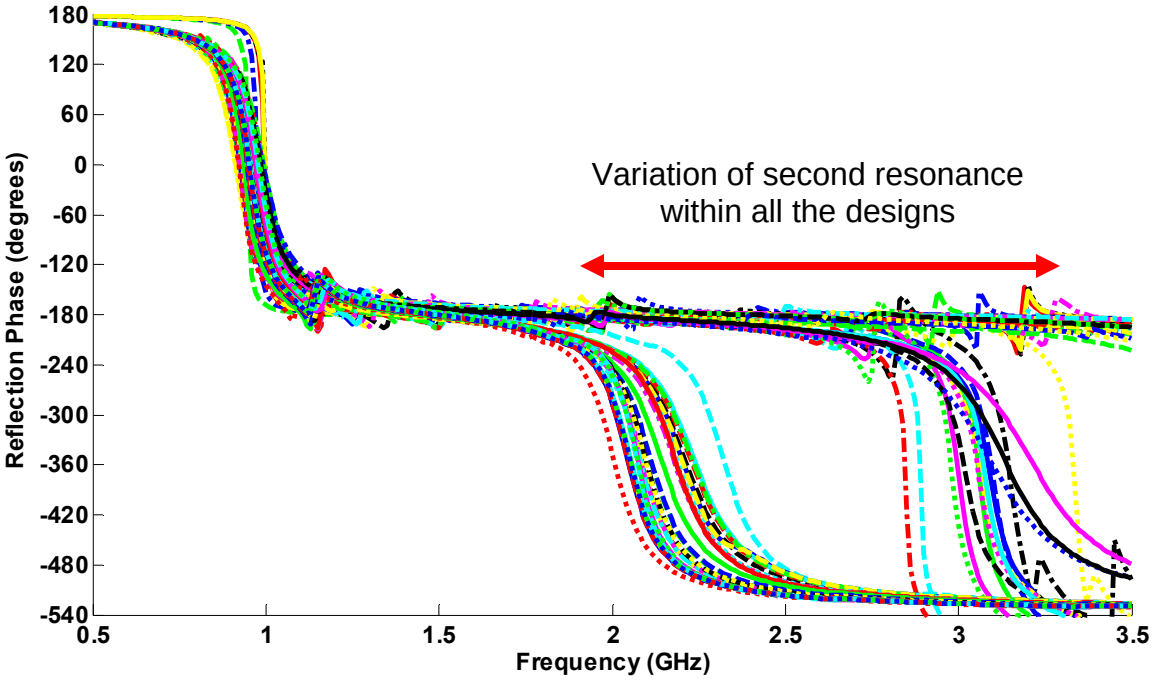

Fig. 4-23 Reflection phase of dual band EBG cell with both IDC and coplanar spiral inductor.

The reflection phase shown in Fig 4-24 corresponds to the best candidate within the data. The first resonance was slightly lower than 1 GHz at 0.95 GHz and the second resonance was slightly higher at 2.06 GHz. This design selection was the most realistic candidate for conventional fabrication after running more than 386 variations of the gap and trace widths. Figure 4-25 illustrates the 15.875mm unit cell with exploded view of the trace and two adjacent gaps each of which are 3 mils. For a true grasp of the scale of the trace and gap, their footprint is the thickness of two sheets of copy paper. Therefore, laser oblation technology was the only option for fabricating this design. The LPKF U3 Protolaser system was used to fabricate the sample shown in Fig. 4-26 [24]. Since the material samples were only available in 6" x 6" dimensions a full pattern was tiled on the surface of the 250mil board. One complication of using the LPKF laser system is that it cannot produce holes in the thicker material and therefore vias could not be easily made. Instead, stainless steel screws were used as a substitute after holes were drilled with a standard milling machine.

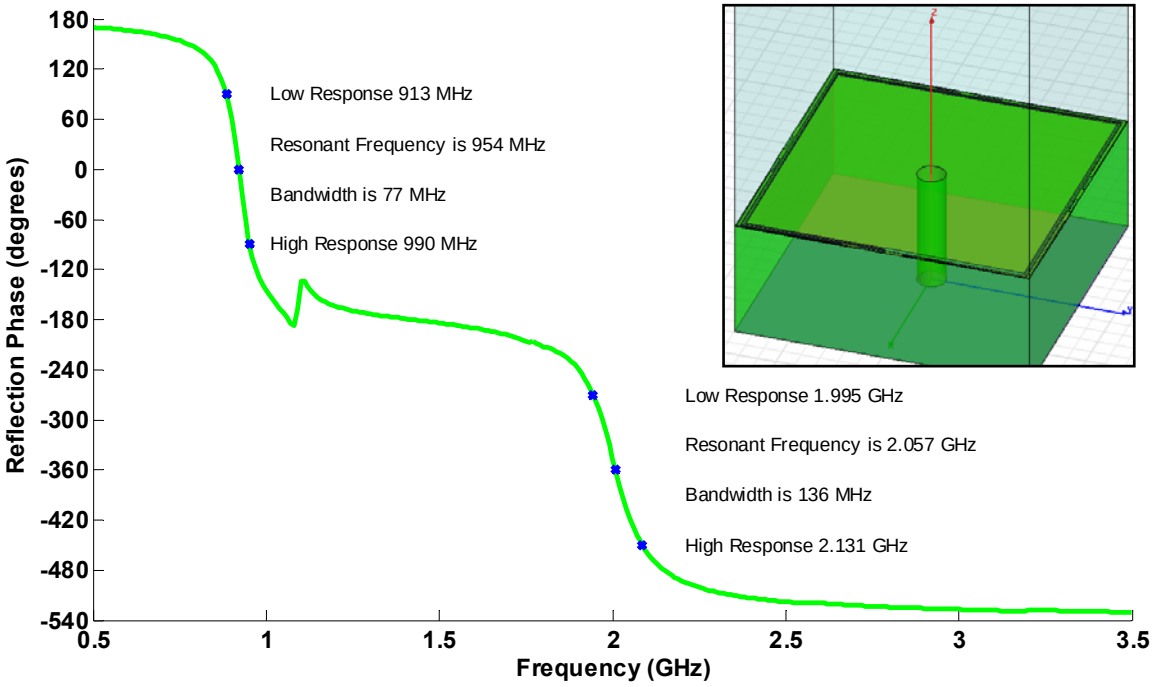

Fig. 4-24 Reflection phase of dual band EBG with two interdigitated fingers and one turn spiral.

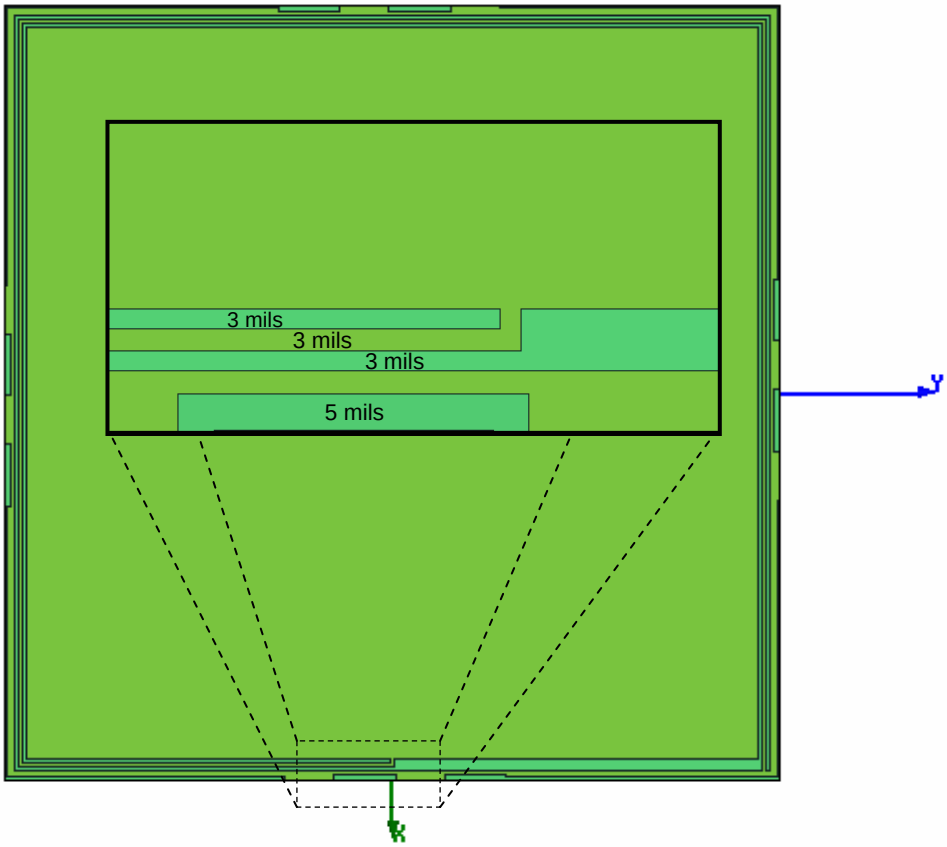

Fig. 4-25 Simulated dual band EBG cell with two interdigitated fingers and one turn spiral.

Fig. 4-26 Fabricated dual band EBG on 250mil Rogers Corp. TMM10 material.

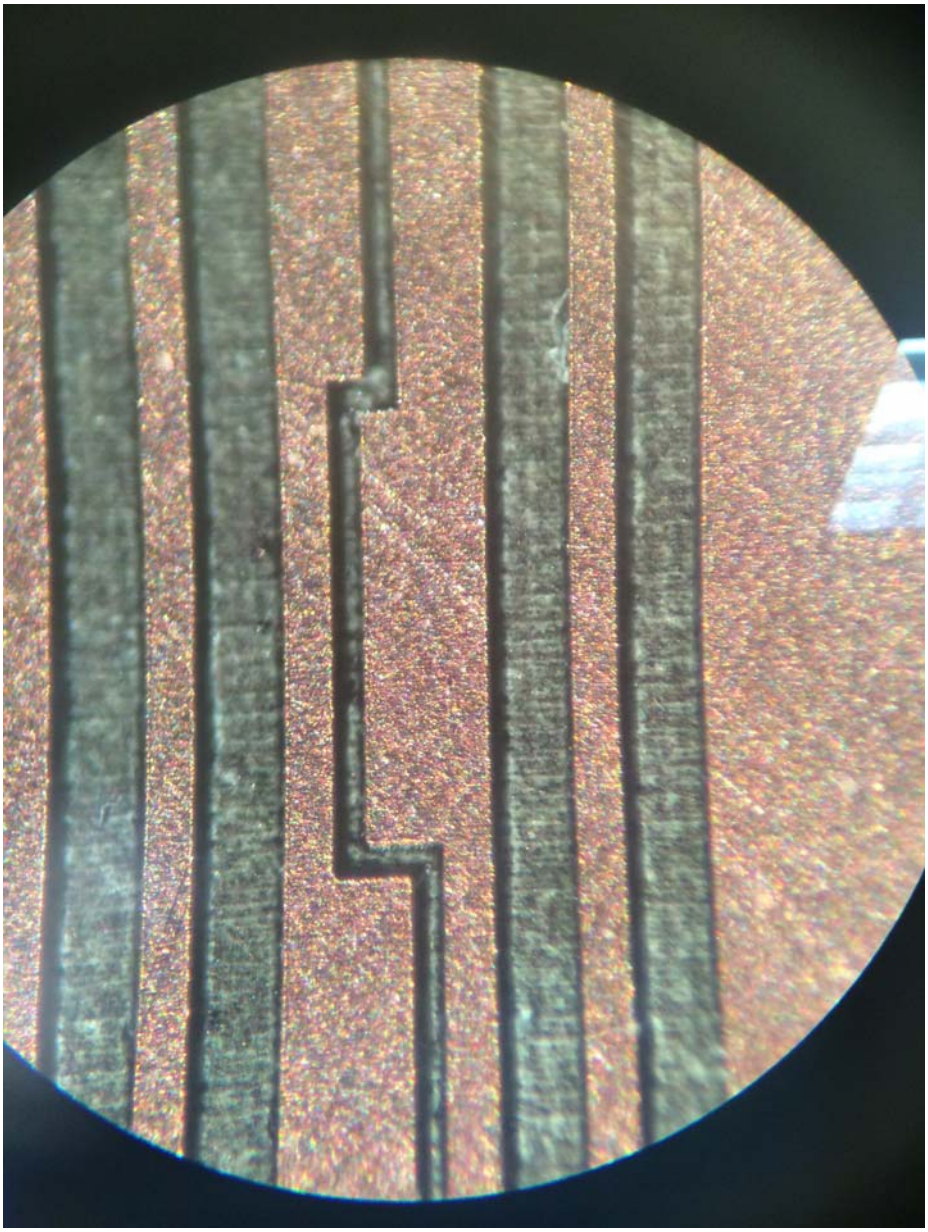

Fig. 4-27 Magnification of interdigitated edge and spiral trace at 70x.

The laser oblation process shows that it is capable of making very fine traces and corners as displayed in Fig. 4-27. Since the laser strikes normal to the material surface, concave surface edges commonly produced with chemical etching are not an issue. This technology therefore will

create the geometry simulated with greater fidelity and therefore better measurement correlation should be expected.

4.8 Low Frequency Artificial Ground Plane Measurement

The measurement of surface reflection at low frequency required special waveguide and other test adapters to perform the tests. The lowest response of the first resonance occurs at 0.91 GHz. Therefore, the WR770 waveguide shown in Fig. 4-28 was selected to perform the reflection measurement. This waveguide has a cutoff at 0.77 GHz and can operate up to 1.45 GHz before multimode propagation starts. The second resonance occurs at 2.06 GHz with the upper operating frequency of 2.13 GHz and will require a WR430 waveguide. Two test setups must be calibrated and performed independently to maintain phase accuracy.

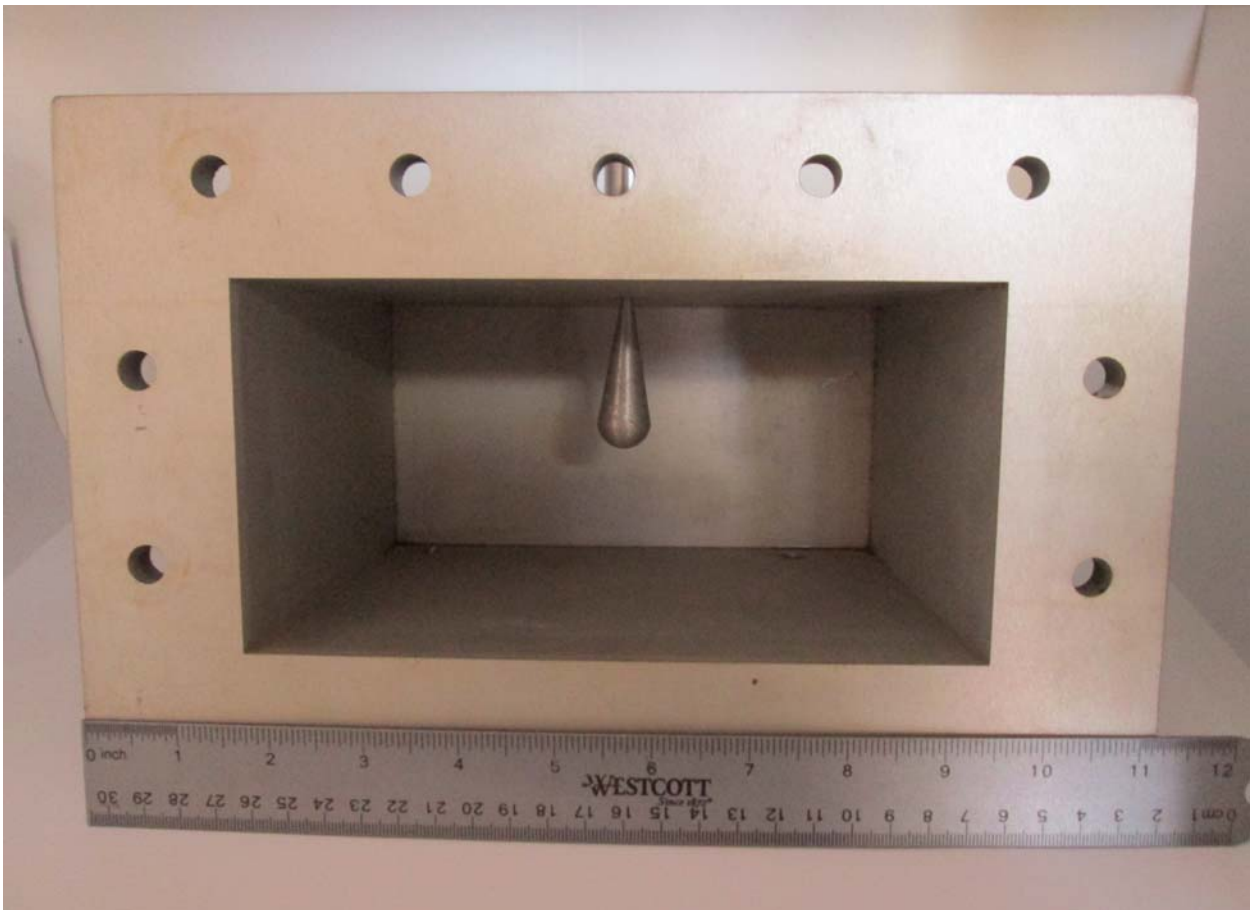

Fig. 4-28 WR770 waveguide adapter used to measure surface reflection.

The measured phase is first calibrated by creating a short at the waveguide face using a copper plate. Since the reflected phase of an electric conductor is always 180°, this measurement will be used to produce the reflection phase response at the material surface.

The data shown in Fig. 4-29 indicates that the bandwidth of the lower frequency is very narrow but much closer to 1 GHz than expected. The second resonance is shifted up by roughly 20 MHz but has a bandwidth consistent with simulation. The 6" x 6" was then incorporated with the dual band loop design to determine the effect of the HIS on radiated patterns and gain.

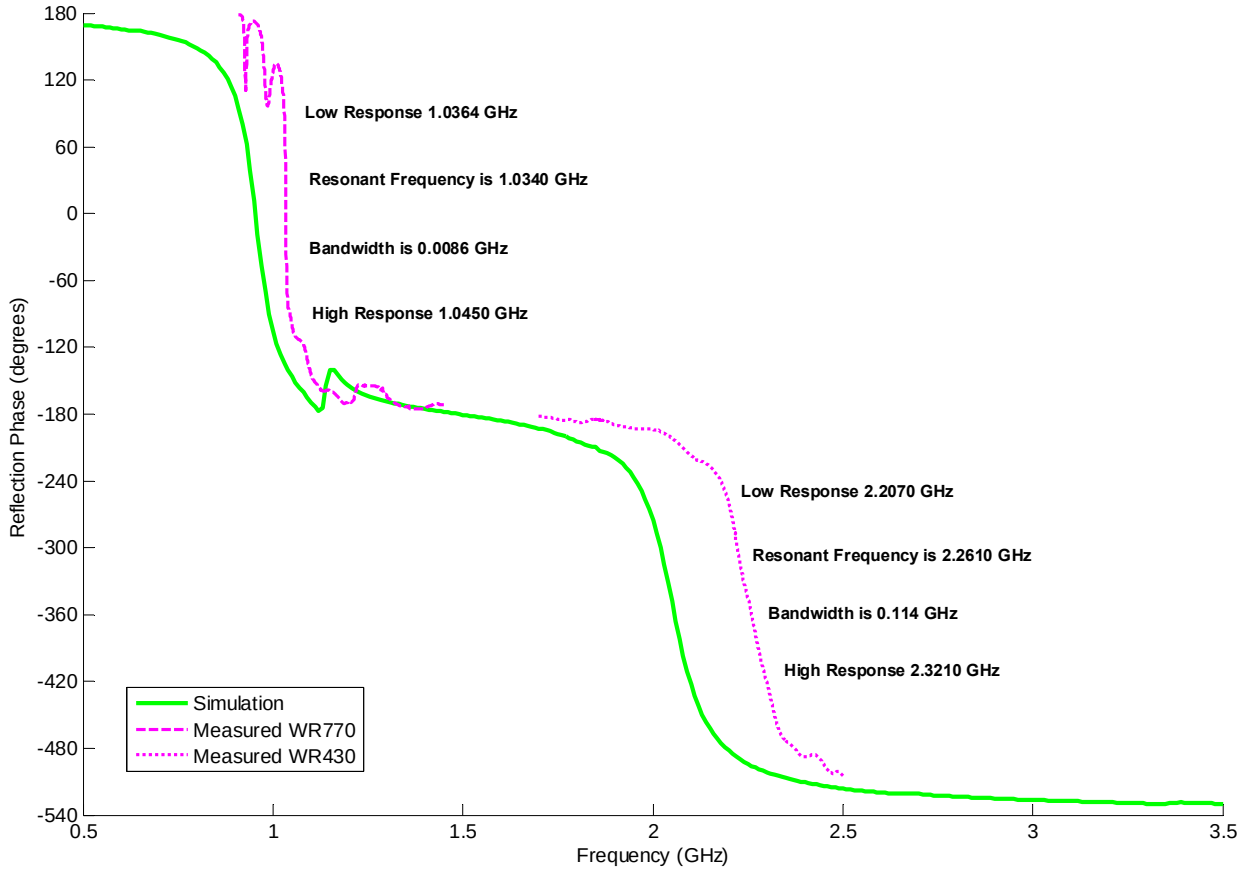

Fig 4-29 Comparison of simulation versus measured reflection phase.

4.9 Integration of Low Frequency Artificial Ground Plane with Loop Antennas

The radiation patterns for both azimuth and elevation are shown in Figs. 4-30 and 4-31 for the antenna backed with the EBG ground plane. The analysis of the patterns show a max gain of 5.69 dBi is achievable. The corresponding front-to-back ratio is greater than 20dB. The asymmetry of the azimuth pattern in the back half plane is consistent with previous measurements and attributed to the test cable and elbow protruding from the AUT.

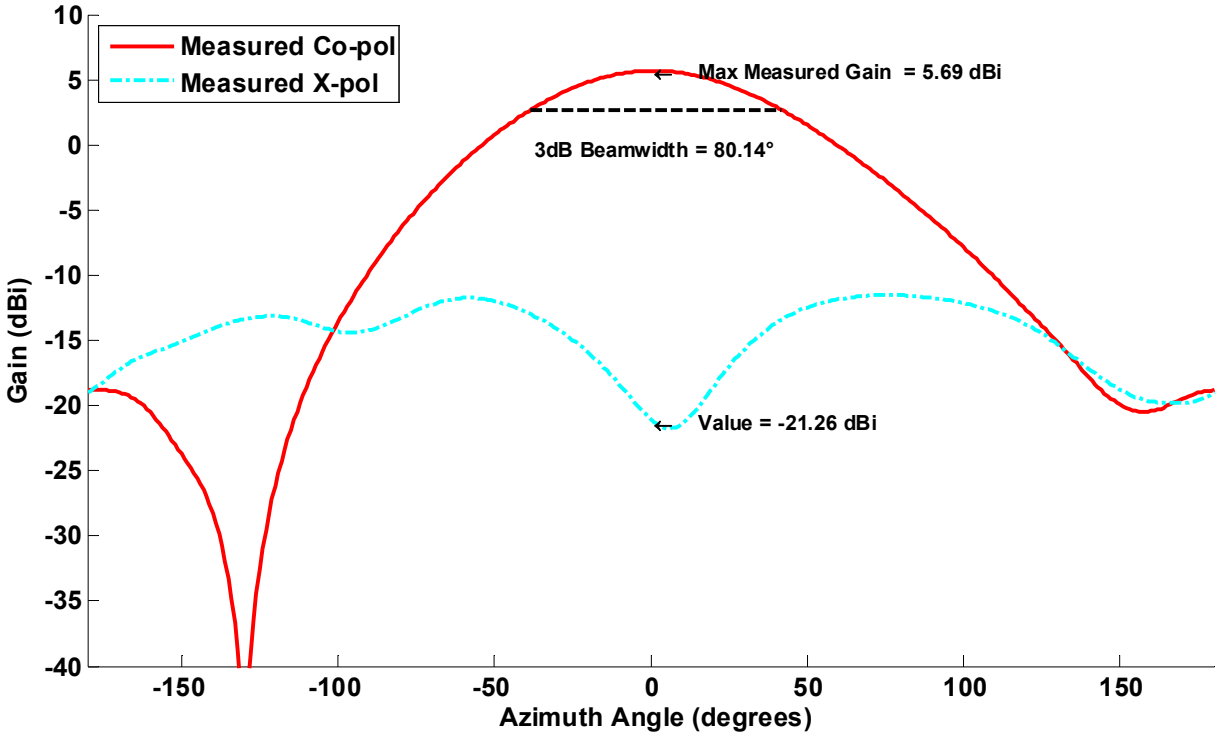

Fig. 4-30 Azimuth (E plane) pattern of horizontal polarized antenna over dual band HIS at 1GHz.

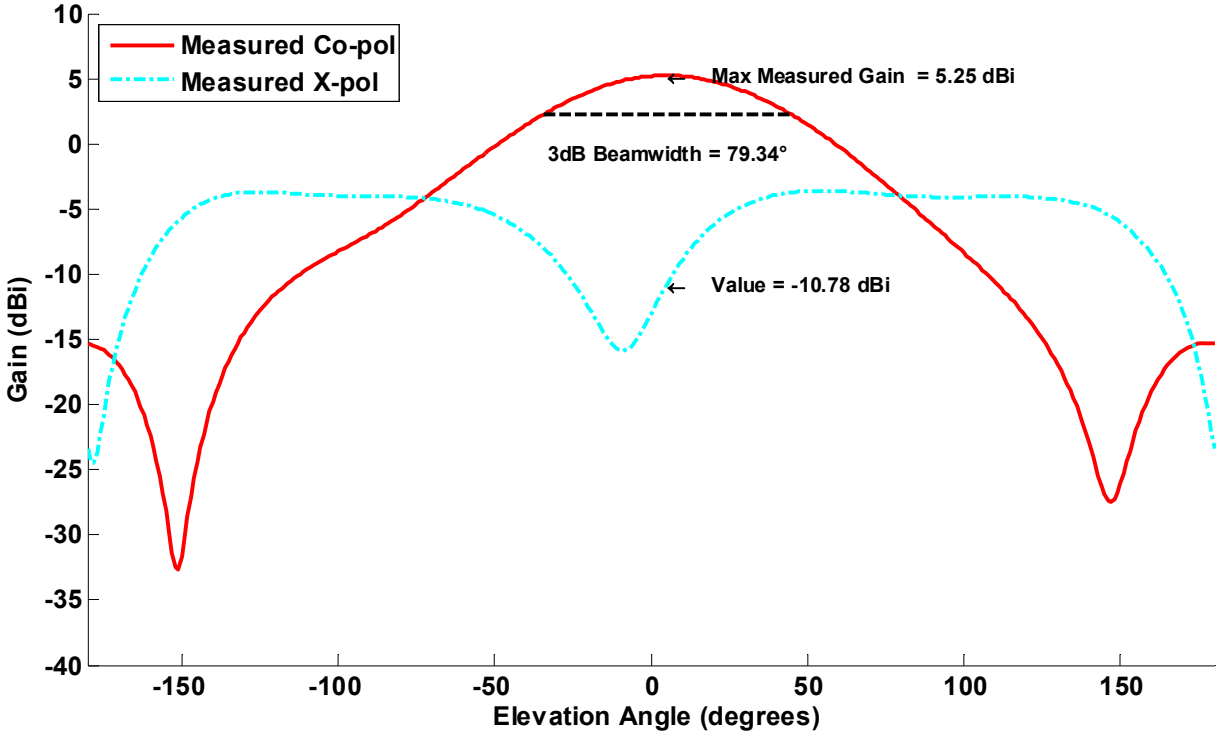

Fig. 4-31 Elevation (H plane) pattern of horizontal polarized antenna over dual band HIS at 1GHz.

A comparison plot for the three cases: antenna alone, antenna with ground reflector at h=1.470", and the antenna with the HIS are shown in Figs. 4-32 and 4-33. Each set of measurements were performed on the cylindrical near field. The elevation patterns were measured by rotating the antenna by 90° to collect full rotation. The azimuth patterns show the maximum gain is achieved with the aluminum plate placed 1.470" below the antenna. The antenna backed with HIS shows it can achieve greater gain than the loop alone and greatest reduction in backlobe radiation. Furthermore, the pattern shows the absence of diffraction typical of the electric ground planes for the antenna with and without reflector. The HIS structure supports radiation down below the horizon without the asymptote seen at ±90°.

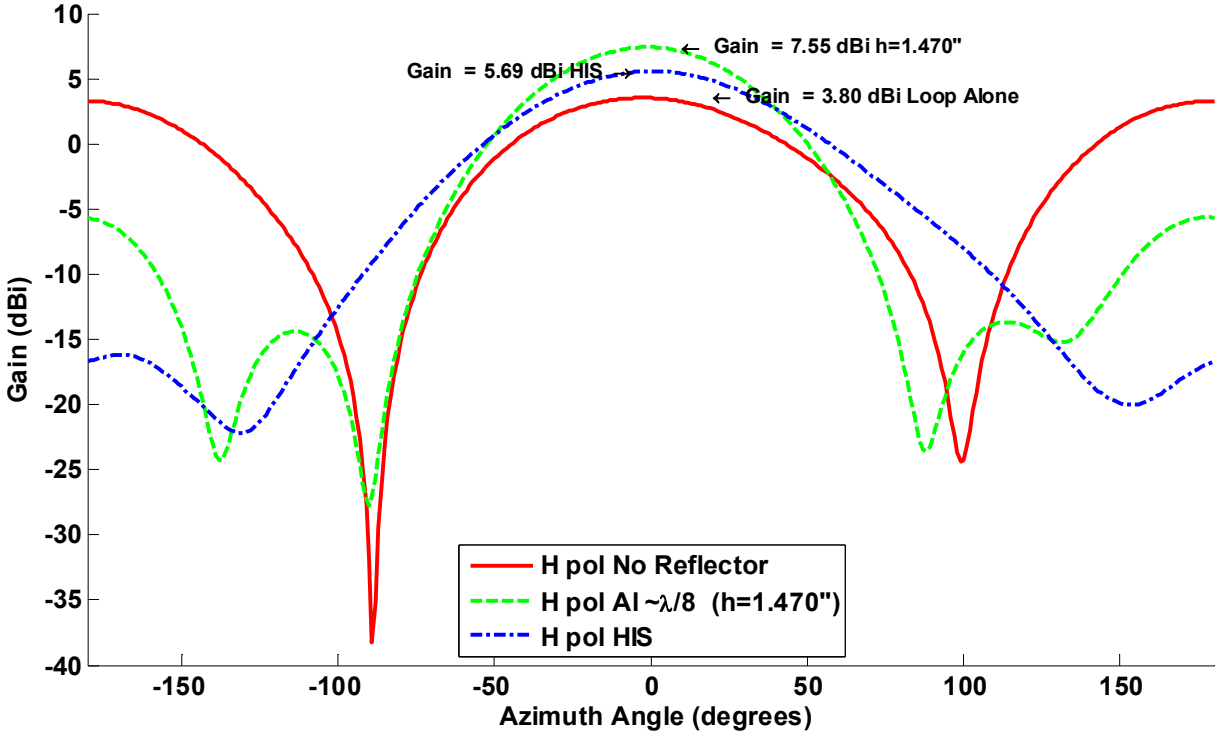

Fig. 4-32 Azimuth (E plane) pattern comparison of the 1GHz design performance.

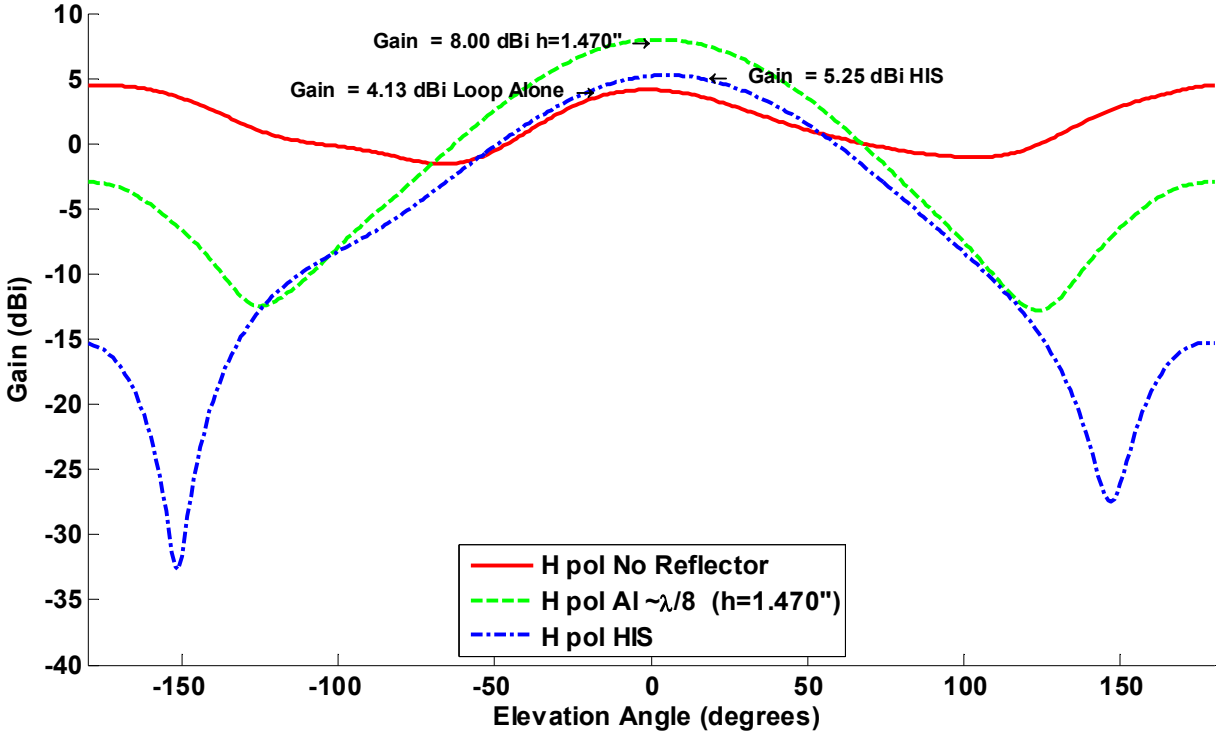

Fig. 4-33 Elevation (H plane) pattern comparison of the 1GHz design performance.

The 2 GHz array was measured on the cylindrical near field and the patterns were synthesized for full unity excitation. The radiation patterns for both azimuth and elevation are shown in Figs. 4-34 and 4-35 for the antenna backed with the EBG ground plane. The analysis of the patterns show a max gain of 9.06 dBi is achievable. The asymmetry of the elevation pattern in the negative angular region is consistent with previous measurements of the antenna with reflector and can be attributed to the truncation of the vertical raster and reflection introduced by the test pedestal and positioner.

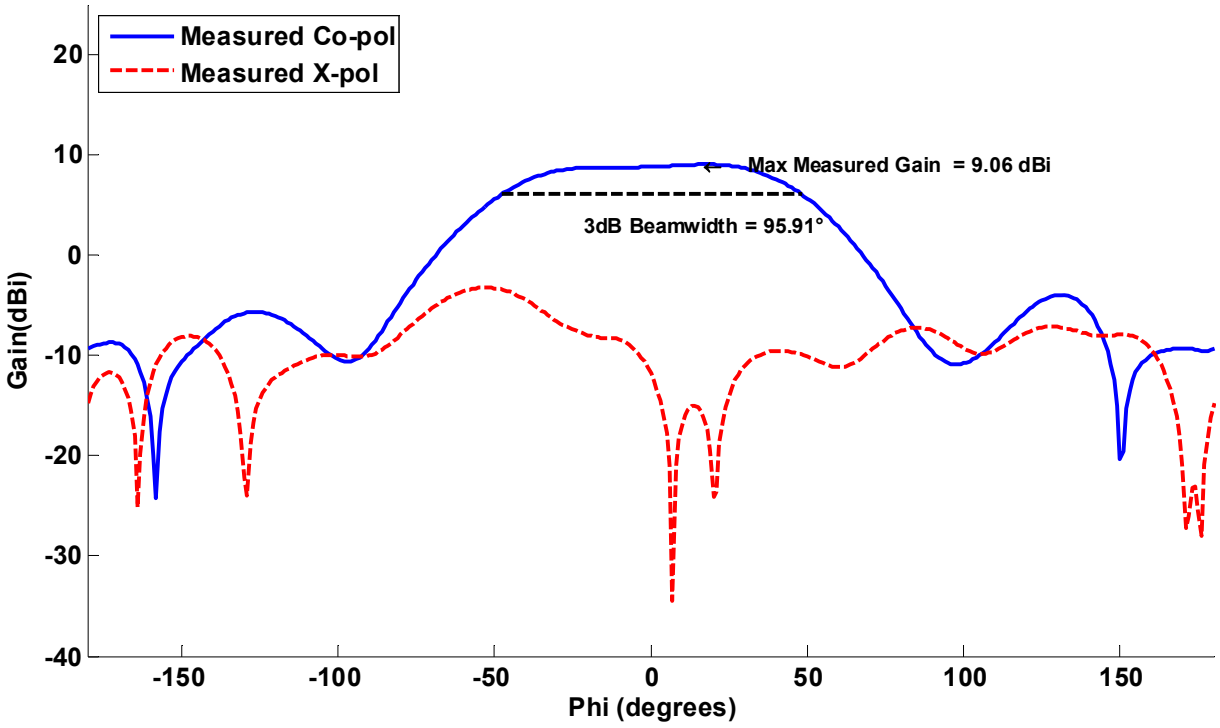

Fig. 4-34 Azimuth (E plane) pattern of the 2GHz array with uniform excitation.

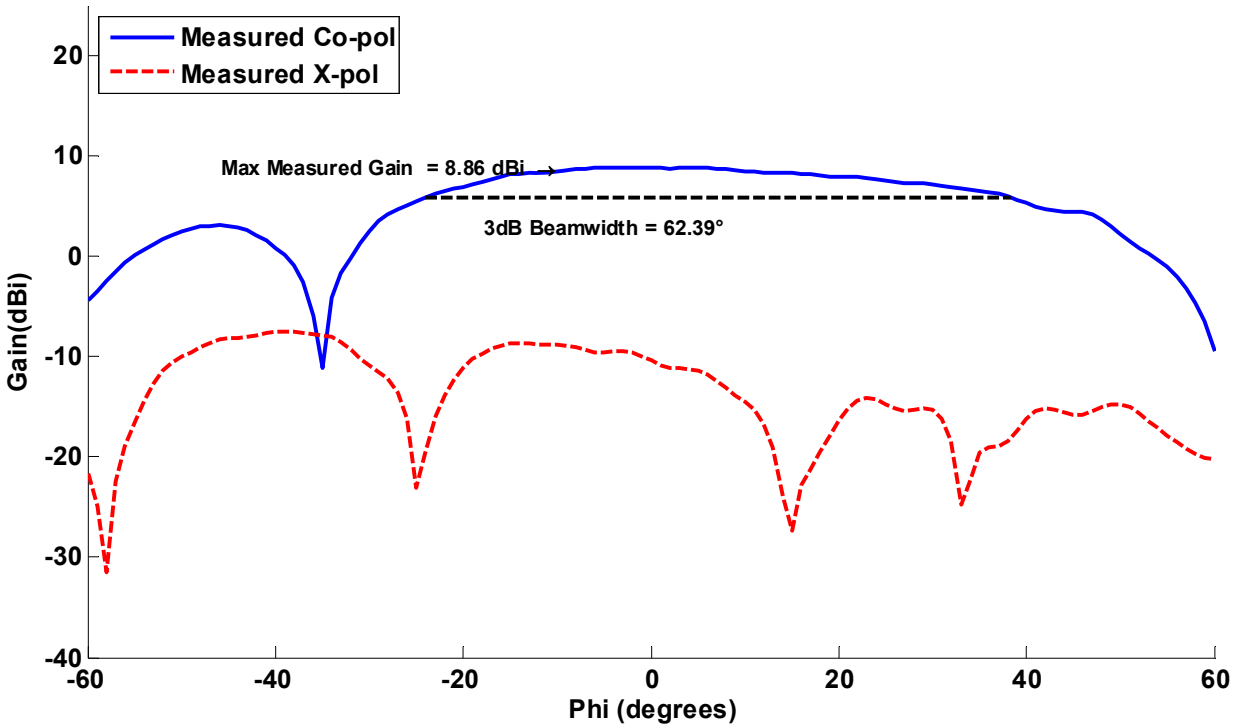

Fig. 4-35 Elevation (H plane) pattern of the 2GHz array with uniform excitation.

A comparison plot for the three cases: antenna alone, antenna with ground reflector at h=1.470", and the antenna with the HIS are shown in Figs. 4-36 and 4-37. Each set of measurements were performed on the cylindrical near field. The azimuth patterns show the maximum gain is achieved with the aluminum plate placed 1.470" below the antenna. The antenna backed with HIS shows it can achieve greater gain than the loop alone with no patterns nulls in the visible region.

The EBG cell design demonstrated dual resonance capability that when combined with the slot antenna geometry reduced the system height beyond that of even the reflecting plate. The HIS design also showed that the challenge of fabricating small features can be overcome by using laser oblation technologies. The measured performance showed an increase in gain was

achieved for both 1 and 2 GHz antennas and is consistent with the behavior of a dual band AMC.

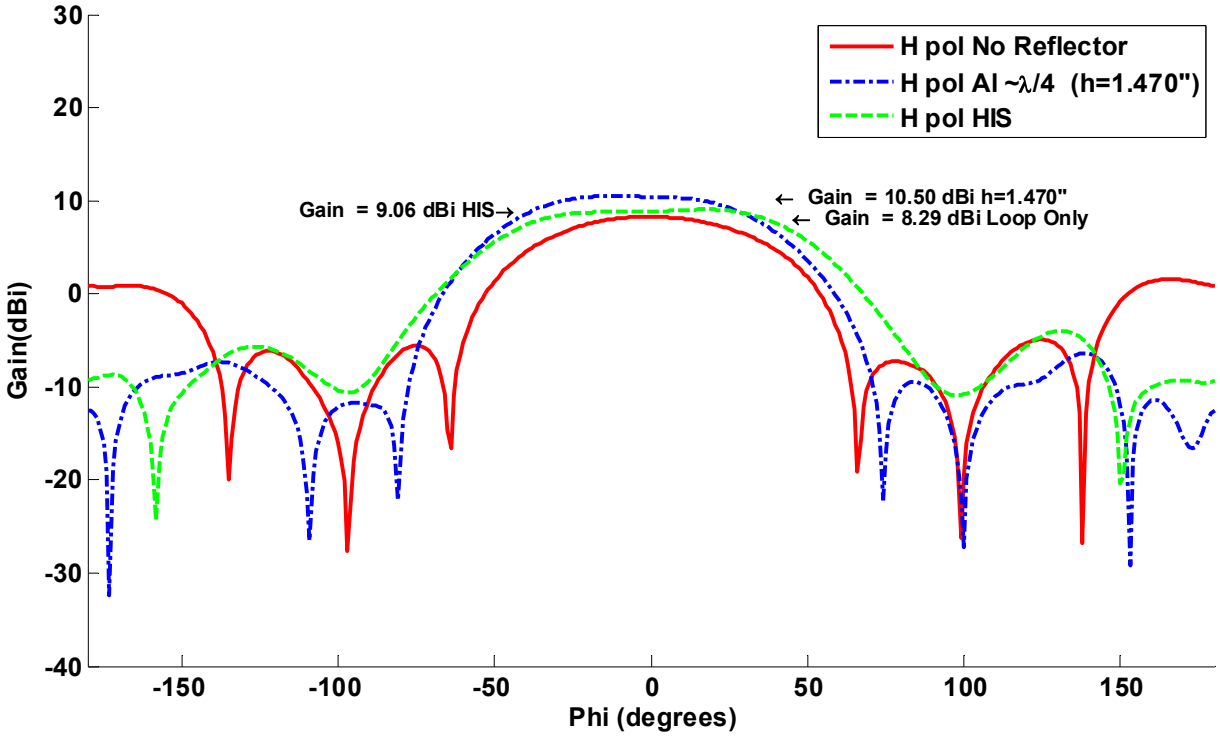

Fig. 4-36 Azimuth (E plane) pattern comparison of the 2GHz array performance.

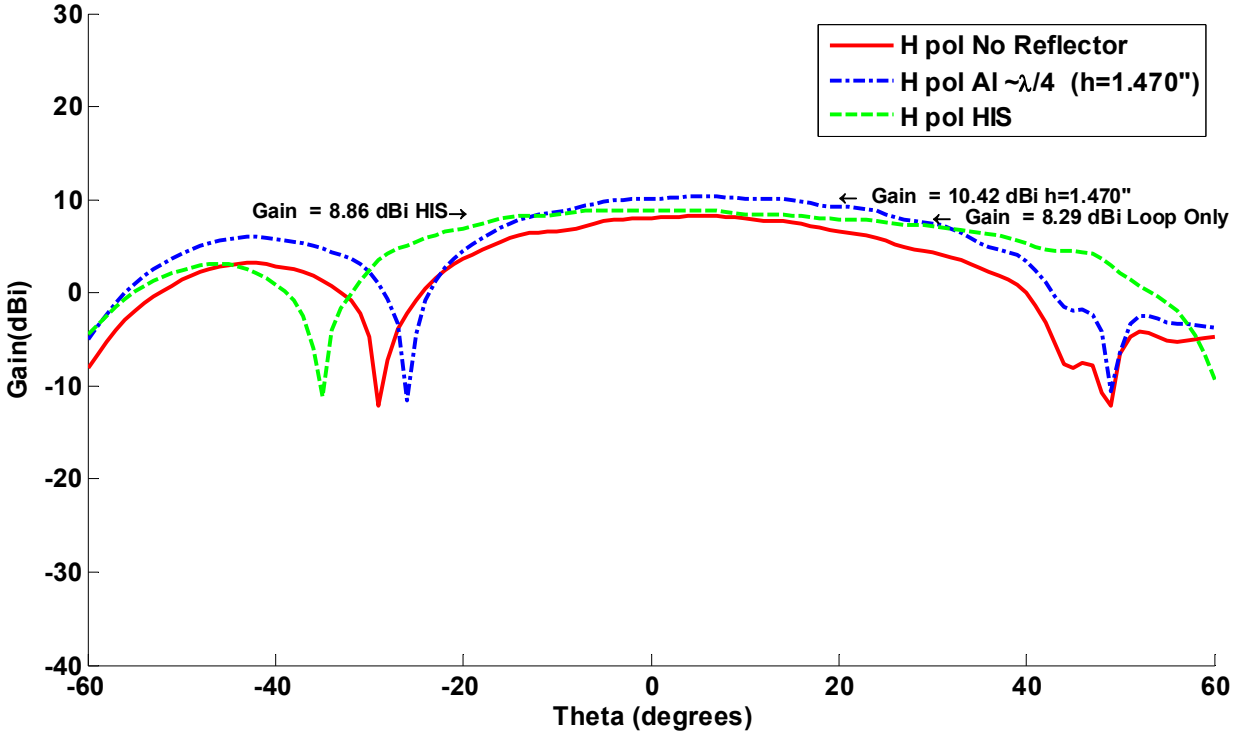

Fig. 4-37 Elevation (H plane) pattern comparison of the 2GHz array performance.

CHAPTER 5

INTEGRATION OF THE X-BAND ARRAY

Multifunctional antenna systems service a variety of defense and commercial sectors due to their compact profile, integrated form, and reduced size, weight, and power. Unlike the trends seen in modern electronic systems where component size can decrease while increasing efficiency, antenna efficiency is lost as the effective aperture is reduced. To overcome this physical reality, modern communication systems are moving to higher frequencies that require smaller antennas for example the 5.8 GHz band for the 802.11G standard. Alternatively, the design of legacy antenna replacements often requires the capability to operate in both existing and future bands yet reside within the same structural foot print. In either case if multiple single function systems can perform the needed task, the integration of multifunctional systems in most cases would be avoided due to complexity and cost. Engineers are therefore driven to reduce both the size and power of the system components through innovative techniques to achieve complete integration. This section demonstrates a technique for integrating a superficial array of X-band patch radiators for additional antenna functionality.

5.1 Antenna Selection

A variety of radiator selections are compatible with the imbedded slot loop design. The patch antenna represents a low-profile design which has hemispherical radiation ideal for an electronically scanned aperture. Furthermore, the dielectric superstrate covering the slot loop antenna can be used as the substrate for patch antenna. If the layout of the superficial array is carefully planned, both the lower frequency slot loop elements and patch array can exist with minimal performance impact. The design of the array must be formulated based on knowledge of the lowest frequency array since the element lattice will have to conform to the greatest common unit cell. The cell dimension is based off of the lattice spacing that is an integer divisor of the 1 GHz lattice. The lower frequency topology restricts most of the options because of the overlap caused, but a spacing of 1/12th the spacing of the 1 GHz array allows the array to be fully populated without any loop antenna blockage.

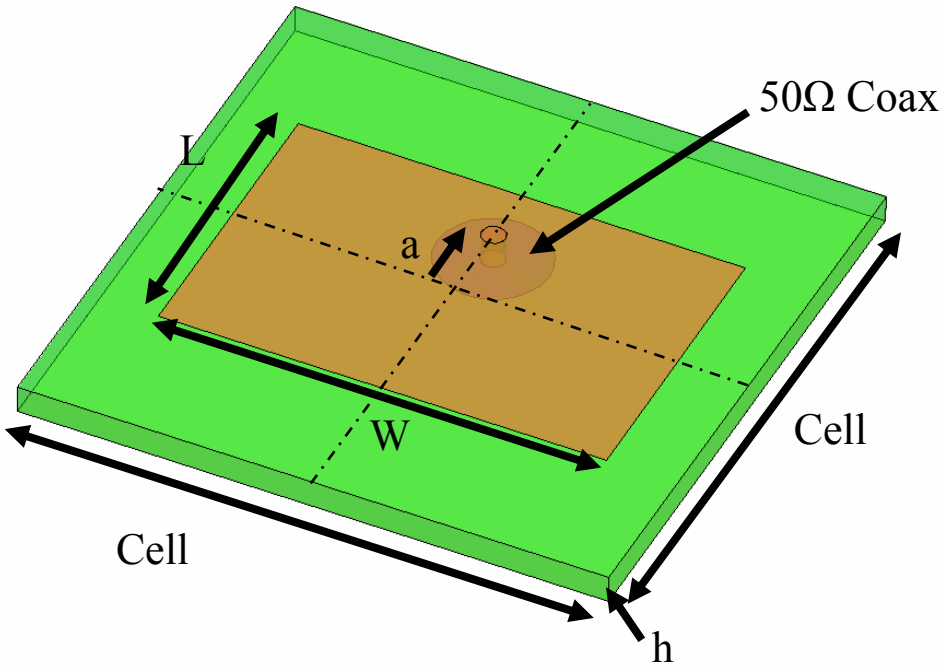

Fig. 5-1 Analysis of patch within a periodic domain.

The patch antenna shown in Fig. 5-1 was designed using HFSS, which contains a periodic boundary condition (PBC) option that can represent the fields of the cell interface as if the element was radiating within an infinite array. The cell size of

$$\frac{\lambda_{12GHz}}{2} = \frac{c_0}{2 \cdot f} = \frac{299792458}{24e+9} = 12.49mm \tag{5-1}$$

was set for the analysis with substrate thickness h=60mil of Rogers 3035 material (ε_r=3.5). The values of L=6.30mm, W=9.47mm, and a=2.50mm were chosen based on the optimization of a 500MHz bandwidth of the antenna around the design frequency of 12 GHz.

Figure 5-2 shows the reflection coefficient of the antenna in the infinite array environment above a conducting ground plane. As a result all the fields in the negative half space are zero so only the upper half hemisphere (theta = -90,90) is shown in Figs. 5-3 and 5-4. The observed cross polarization values of this element were below -40dB and therefore were omitted from the plots for clarity.

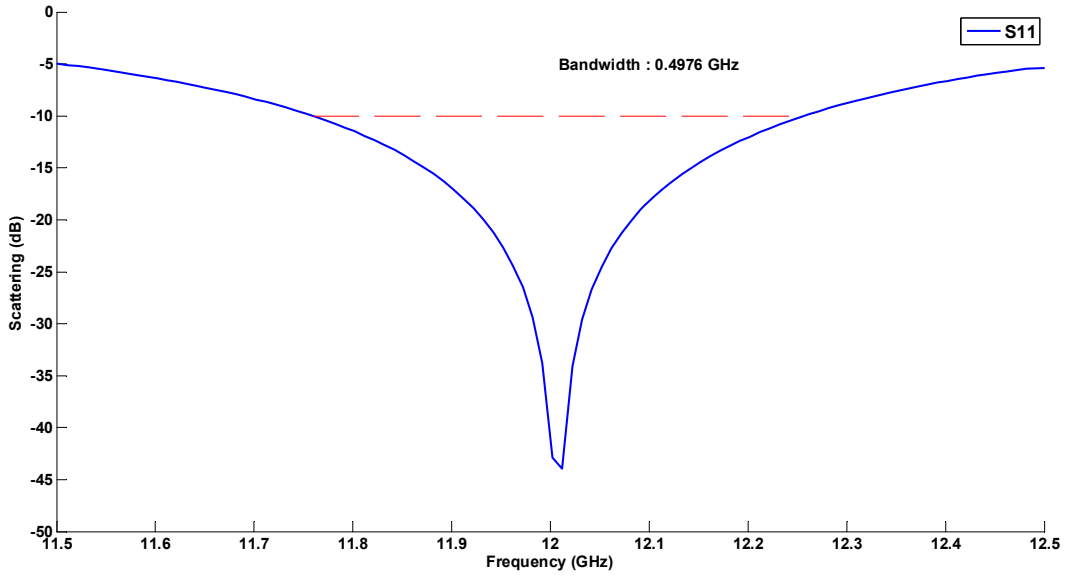

Fig. 5-2 Reflection coefficient at coaxial input for antenna in infinite lattice.

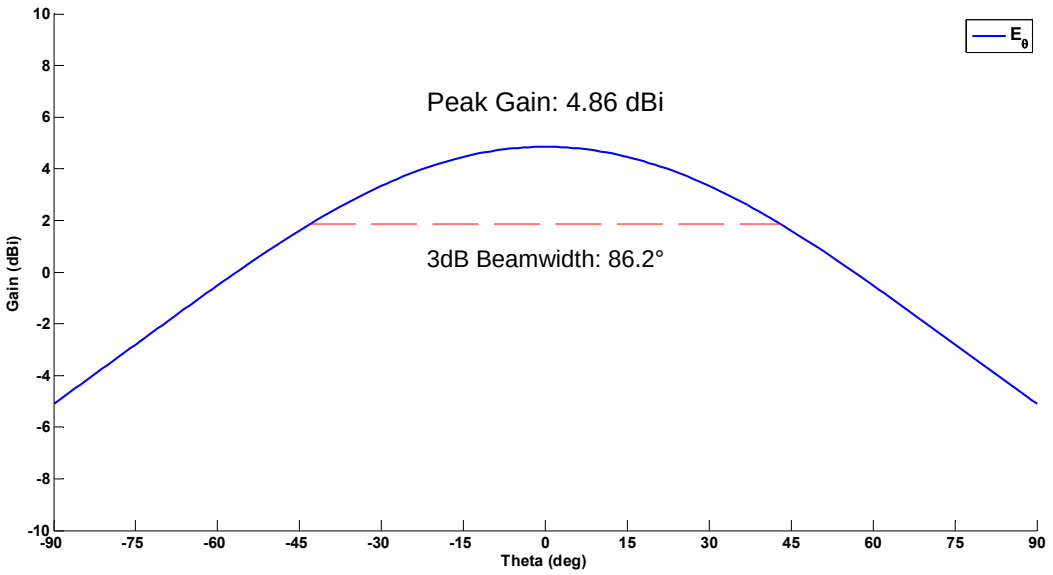

Fig. 5-3 E plane (phi=0) pattern cut.

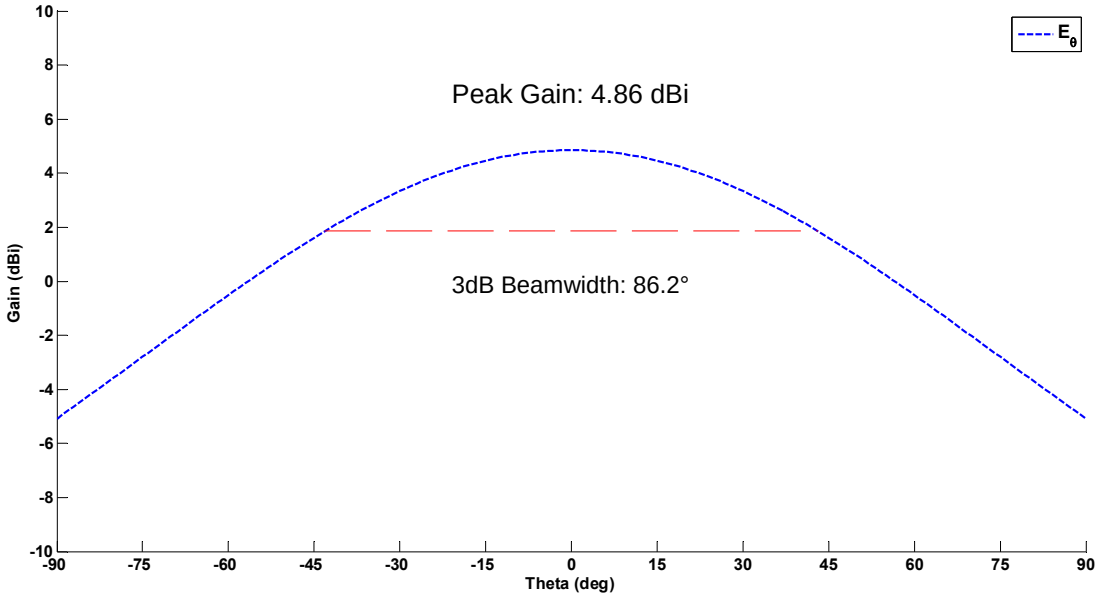

Fig. 5-4 H plane (phi=90) pattern cut.

The directivity of the λ/2 x λ/2 cell can be evaluated to determine the efficiency of the patch element. Since

$$D = \frac{4\pi A}{\lambda^2} \Rightarrow \frac{4\pi\left(\lambda^2/4\right)}{\lambda^2} = \pi \Rightarrow 10\log_{10}(\pi) = 4.97 dBi\,, \tag{5-2}$$

the simulated gain in the infinite environment along with the less than -40dB reflection indicates that the patch has near ideal behavior.

5.2 Feed Network

The feed network that interfaces the X-band array is shown in Fig. 5-5. This design is based on stripline technology with a 50Ω width of 1.69mm and 0.5oz copper thickness of 17um. The quarter wavelength stub is 1mm in width and 3.75mm long. The shielding fence is produced by an offset contour of 2mm from stripline trace with vias of radius 0.25mm. The coaxial probe outer radius is 0.26mm with a shield radius equal to 1.24mm using Teflon insulation. The 2 x 2 corporate network was analyzed using HFSS over the extent of the operating band. Since no beam steering is required, the network was optimized for minimal input reflection at all five ports with uniform transmission amplitude and phase to the 4 antenna feed ports. The transmission line impedance versus frequency is reported in Fig. 5-6. Figure 5-7 represents scattering parameters of the 5 port network.

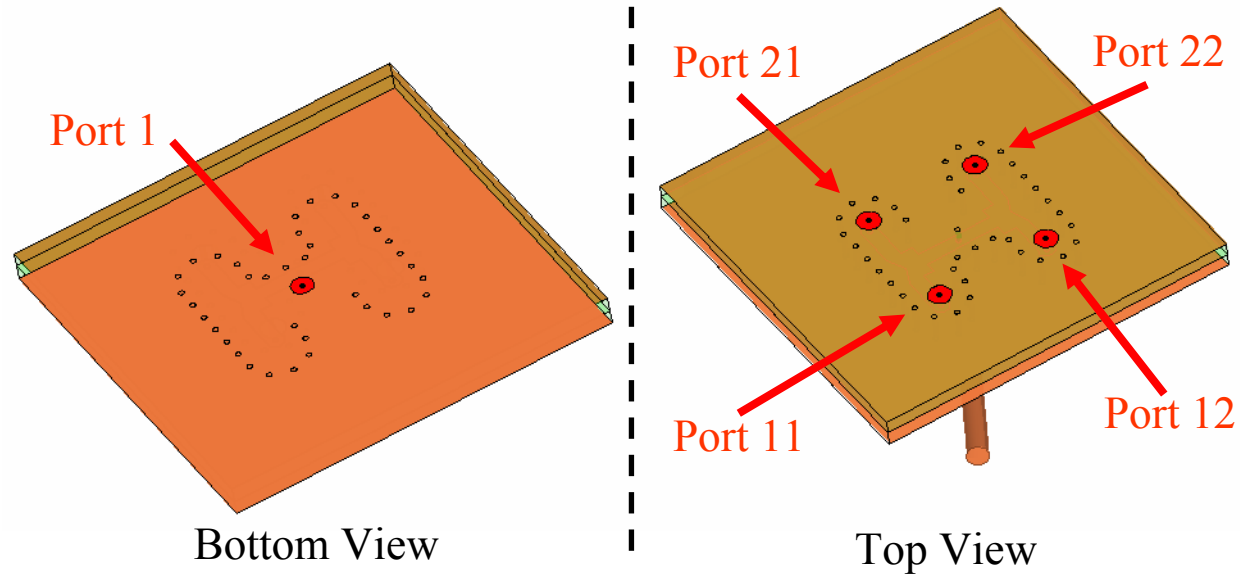

Fig. 5-5 Stripline corporate feed network for the nigh frequency array.

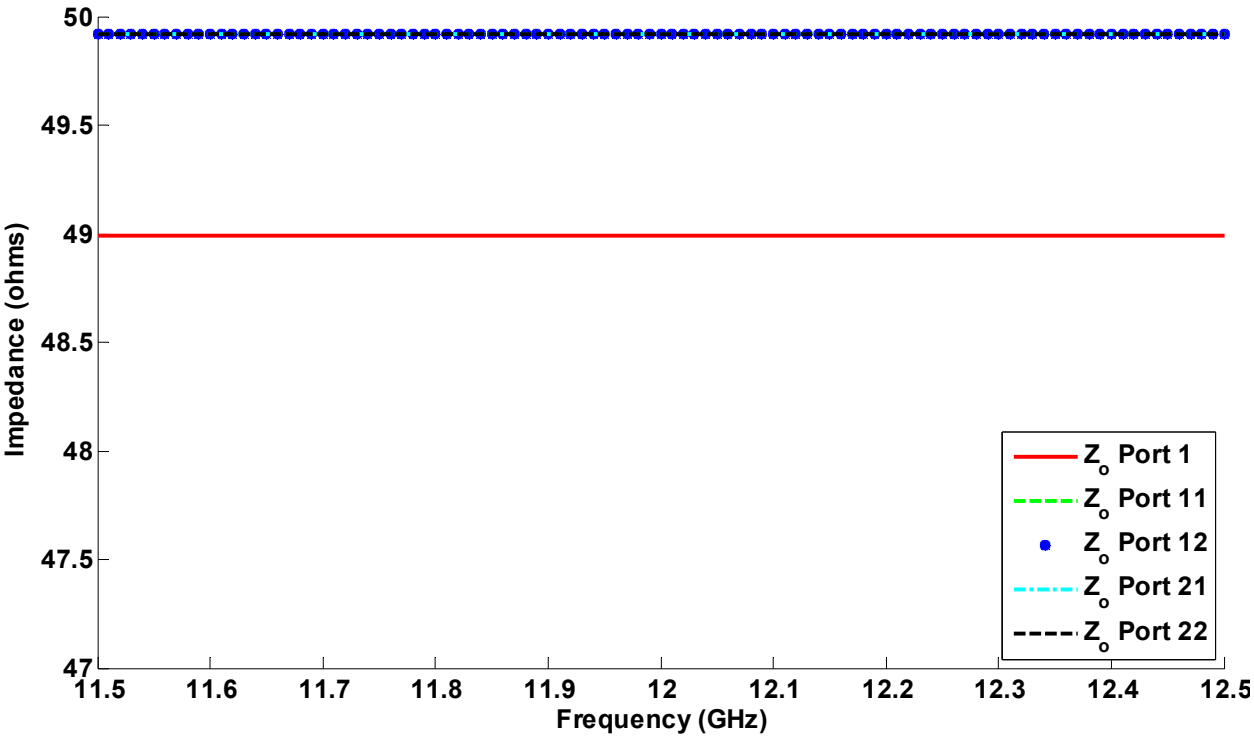

Fig. 5-6 Stripline corporate feed network for the 2 x 2 X-band patch array.

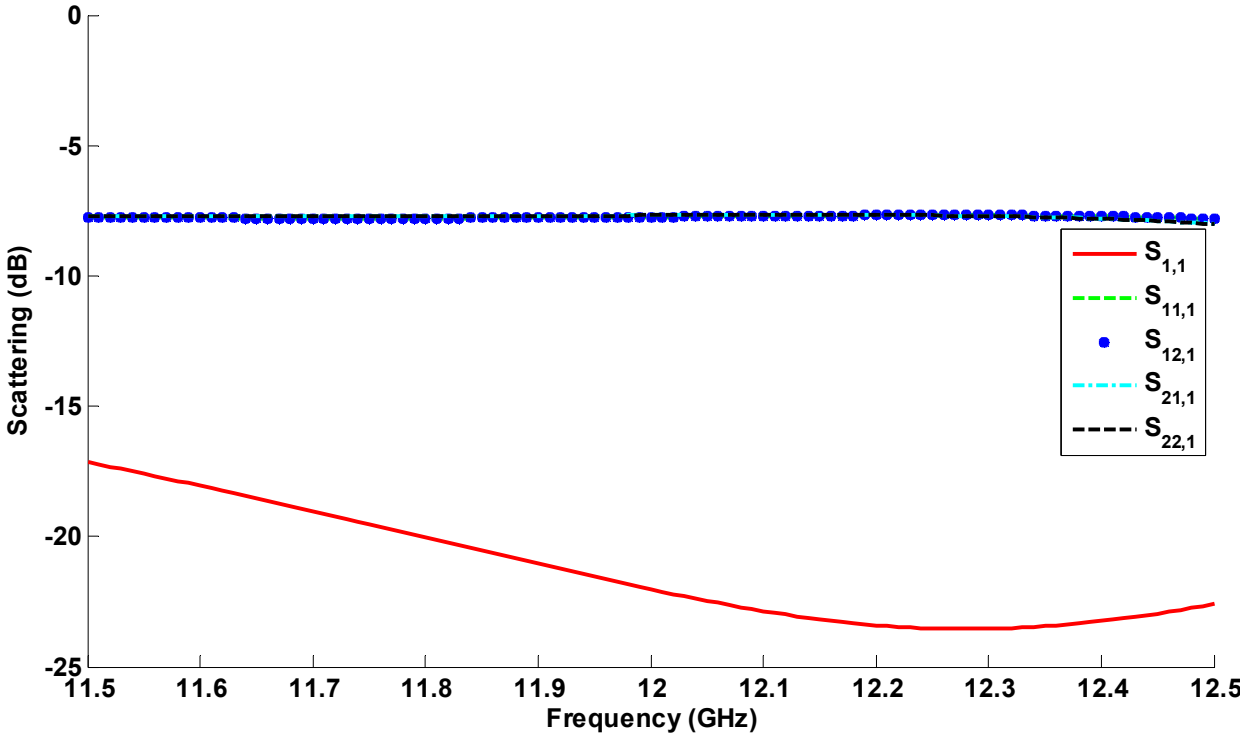

Fig. 5-7 Stripline corporate feed network for the 2 x 2 X-band patch array.

5.3 Near-Field Measurements

The simulation of the combined X-band array and associated feed network was intractable based on the resources available. Since great care was taken to maintain shielding between the adjacent 2 x 2 sub-cells, the only coupling expected will be from the antenna elements themselves. Therefore, only the patch array was simulated with individual coaxial port for each antenna [7]. The patch elements used in the design become more directive as the board thickness is reduced [25]. Moreover, the selection of the RO3035 material with permittivity of 3.5 will enhance the gain while reducing the size. It should be noted that the element gain is an additional factor in design process because the dielectric selected for its substrate was dictated by the loop iteration process in Fig. 2-11. If the gain is to be greater at boresight the material

permittivity should be lower. Alternatively, if a lower resonant frequency is required the expansion of patch design size must be monitored to avoid blockage of the low frequency slot loops.

The triband array incorporating two reflector backed loop antennas and X-band array was tested using a cylindrical near field setup illustrated in Fig. 5-8. The vertical scan travel of the system was 8' so the 6" x 6" AUT was placed at the mid-point of the linear travel. The positioner was then incrementally rotated in azimuth plane between raster scans. In near field testing the setup requires greater raster travel to compute patterns at low scan angles. Therefore, the maximum available raster length was used to capture the near field so the patterns could be projected to the lower elevations and avoid truncation ripple. Figure 5-9 illustrates the large scan travel required for lower angles.

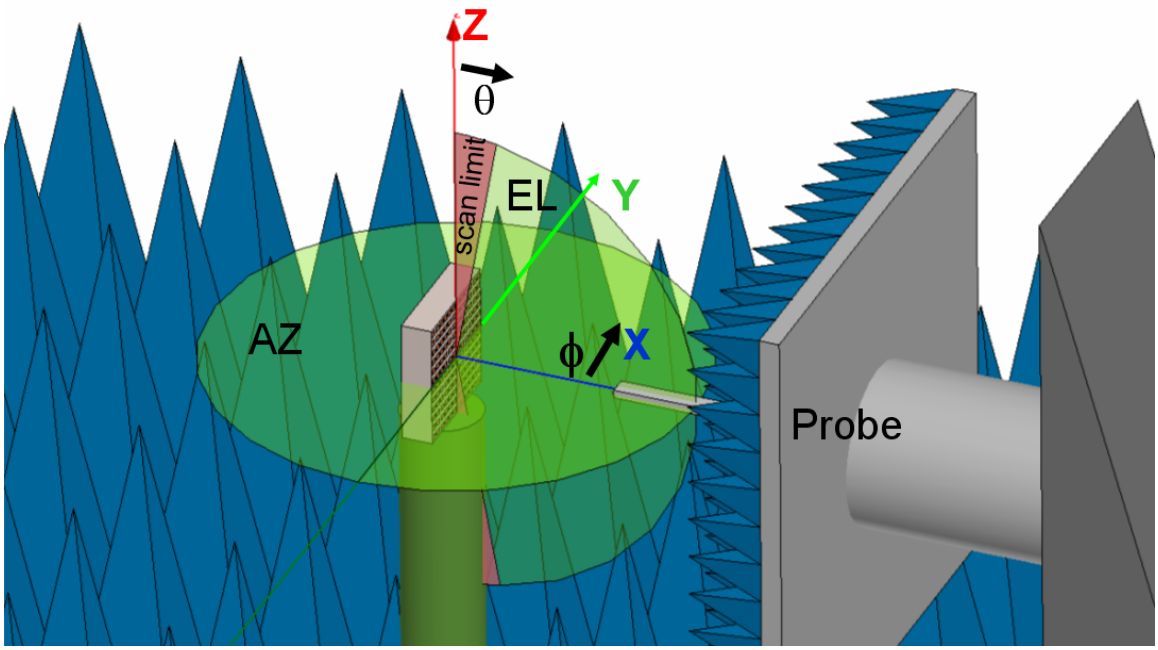

Fig. 5-8 Cylindrical near field setup.

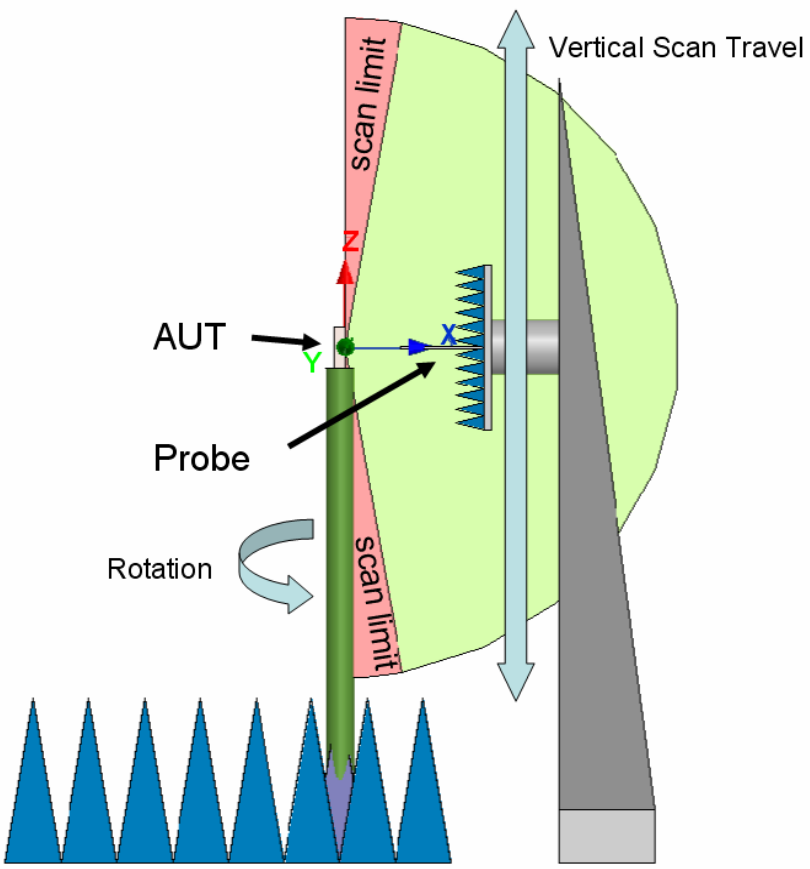

Fig. 5-9 Scan limitations of the cylindrical near field setup (side view).

The prototype X-band patch array contains no electronic beamformer only 36 individual coaxial ports to feed the 144 elements. The measurement of the full array was not practical since each of the 2 x 2 cell must be measured individually. To reduce the measurement time and cost, the edge elements shown in Fig. 5-10 were terminated with 50Ω loads. Typically these antennas are used as dummy elements since they improve array patterns. The row column labeling convention is also described in Fig. 5-10 for collected data. The 16 sets of azimuth and elevation data were more than could be realistically presented so a sample element (1,1) was chosen to review the individual gain pattern. The principal plane cuts at 12.0 GHz are shown in Figs. 5-11 and 5-12.

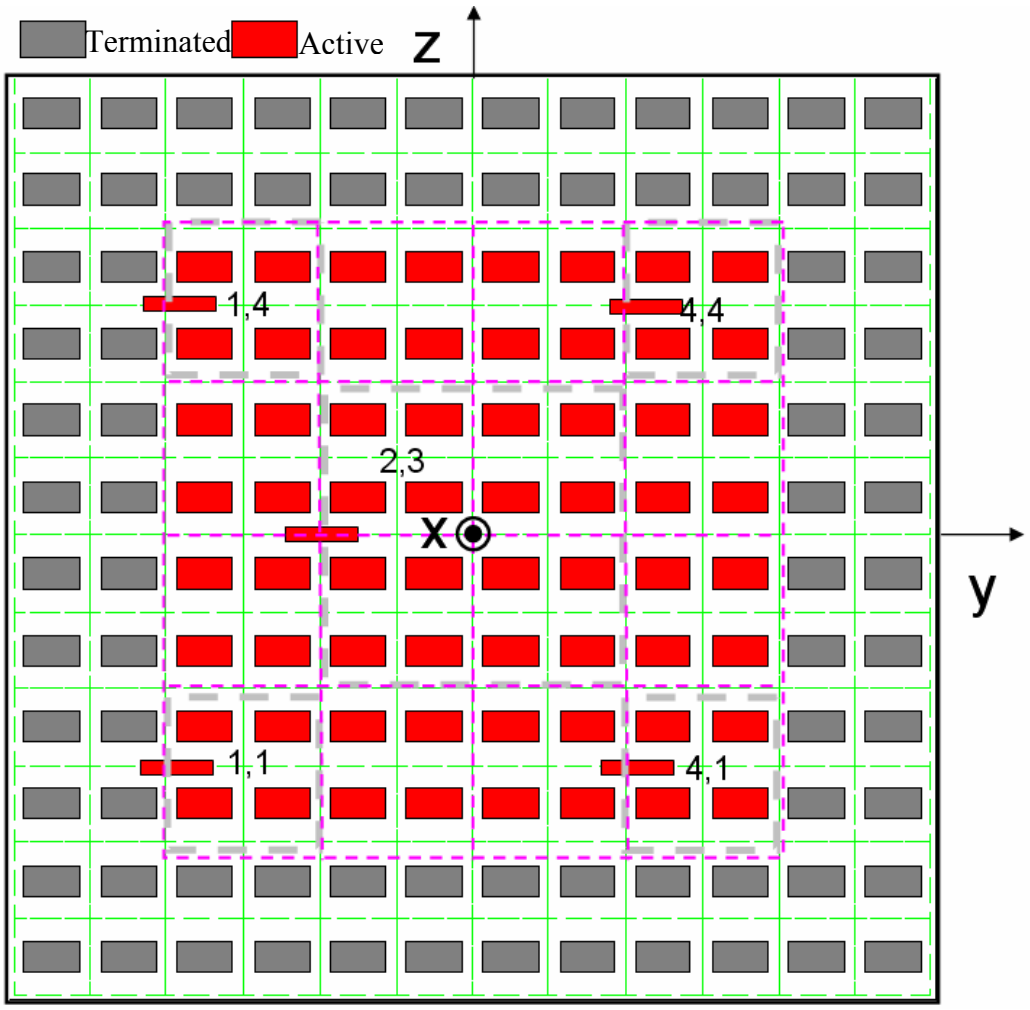

Fig. 5-10 X-band patch array with non-active elements shown with labeling convention.

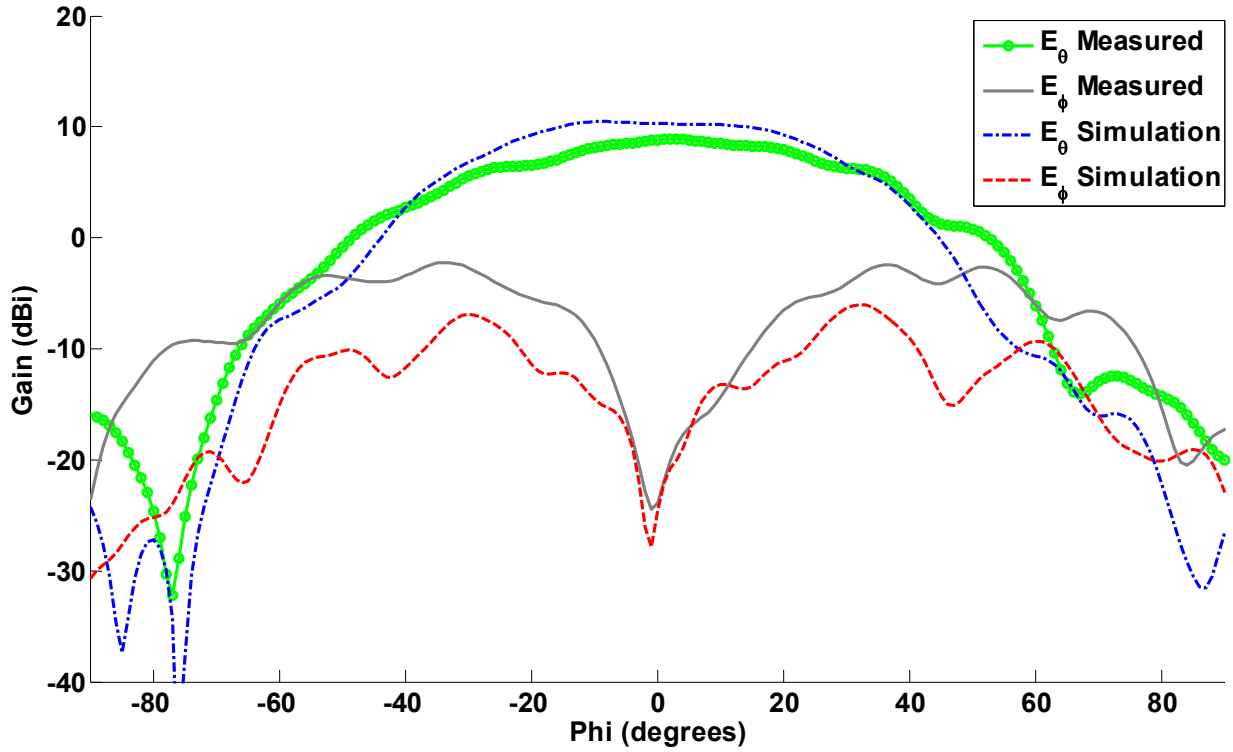

Fig. 5-11 Azimuth (H plane) pattern of vertically polarized X-band patch sub-array (1,1) .

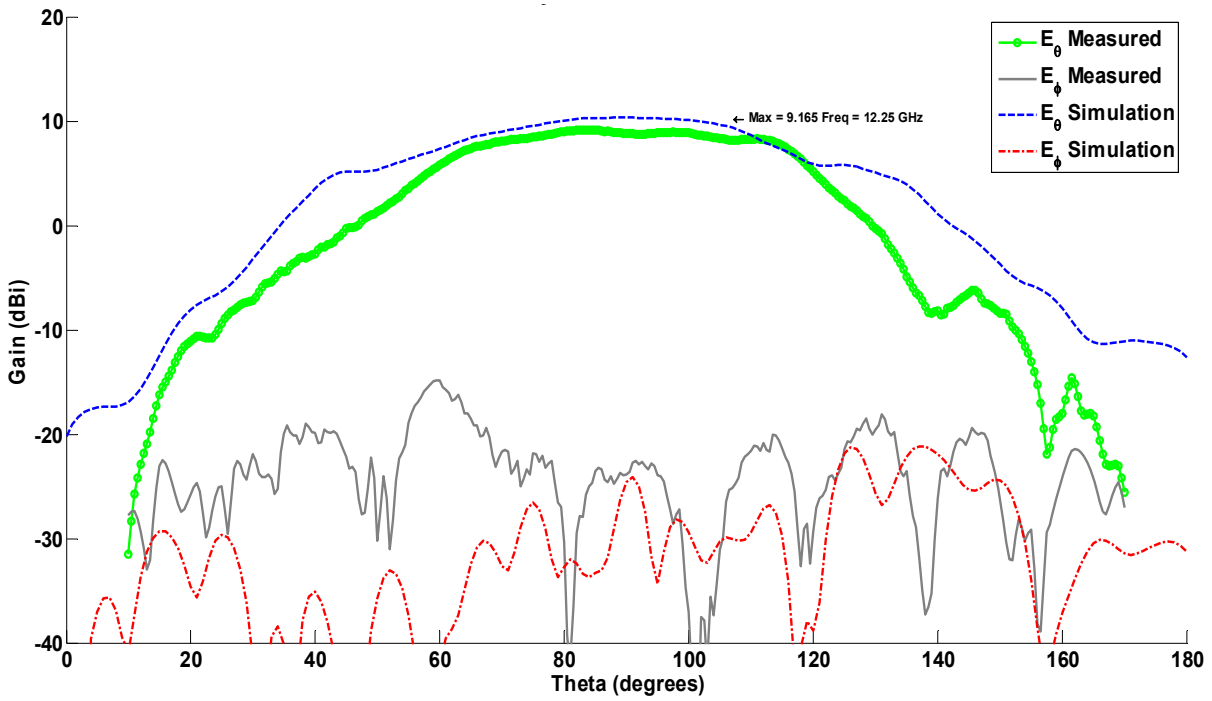

Fig. 5-12 Elevation (E plane) pattern of vertically polarized X-band patch sub-array (1,1) .

Figures 5-13 and 5-14 are contour plot for the single element as well as the array with full illumination at 12 GHz. The results indicate the array is capable of directive radiation without needing the edge elements. The principal pattern cuts for the array with unity exitation are shown in Figs. 5-15 and 5-16.

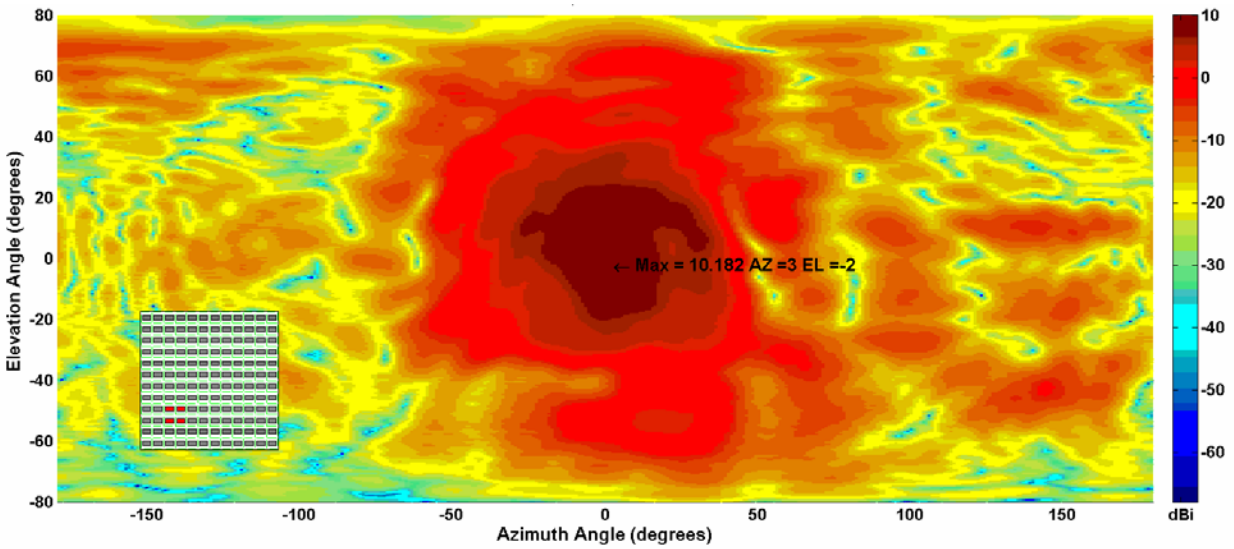

Fig. 5-13 Measured co-polarized gain of a single sub-array 1,1 at 12 GHz.

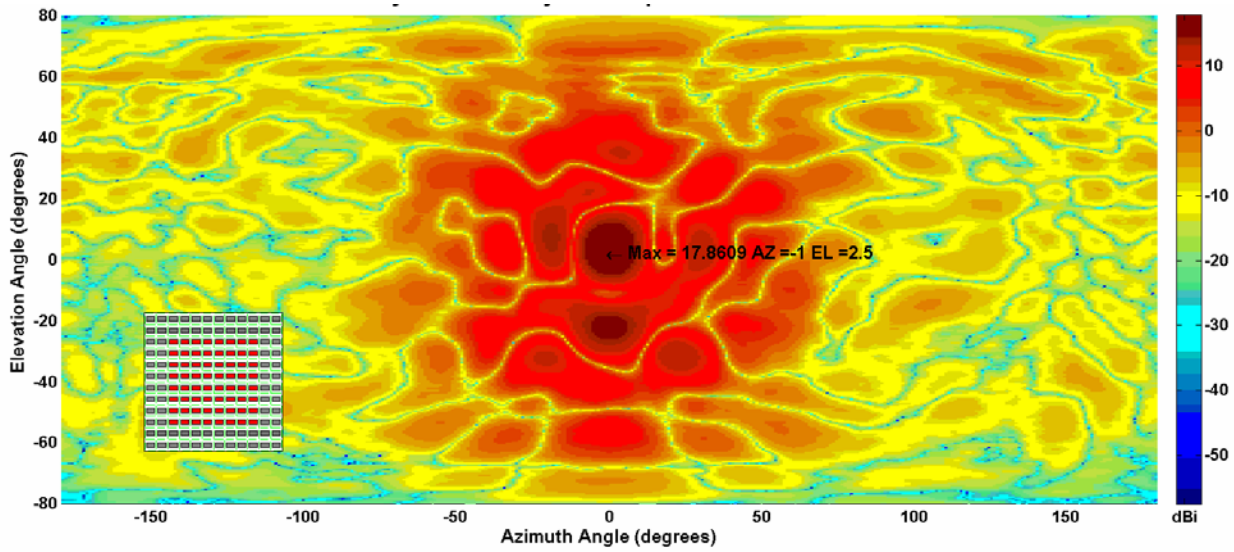

Fig. 5-14 Synthesized co-polarized gain of the 64 element array with unity feed at 12 GHz.

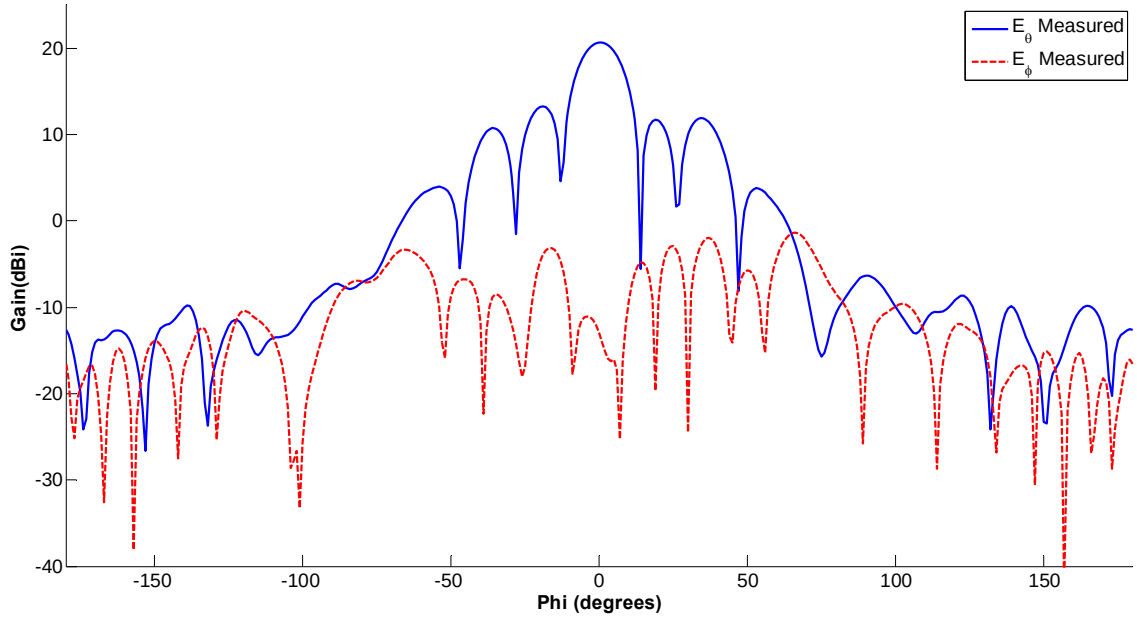

Fig. 5-15 Measured (H plane) gain of the 64 element array with unity feed.

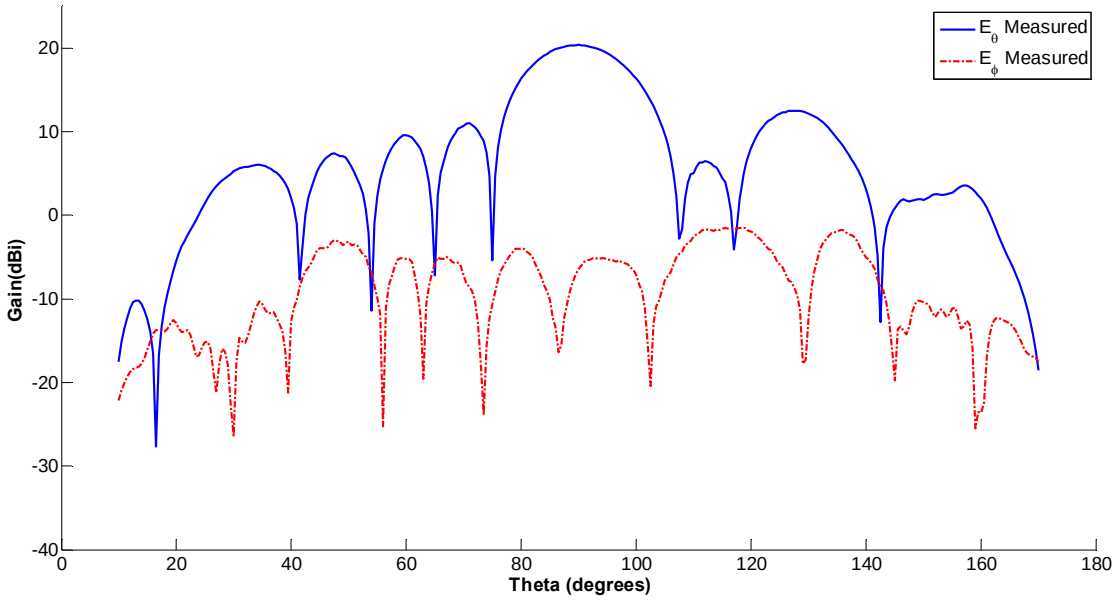

Fig. 5-16 Measured (E plane) gain of the 64 element array with unity feed.

The measured results of the superficial patch array agree very well with simulation data. Furthermore, the slot loop antennas embedded within the ground plane did not prevent the array from achieving high gain. The feed network connections that originate from below the array allow the design to be more compact than those requiring edge feeding so multiple concatenated cells could be used to increase the gain. The goal of the X-band integrated antenna was successful and demonstrated the utility of the design practice outlined in this work.

CHAPTER 6

CONCLUSIONS AND FUTURE WORK

A novel technique was proposed that enabled the design of a low profile and conformal aperture supporting a tri-band array. The antennas utilized the surface area to combine three bands into a common aperture. The process was explained with details required for expanding to alternative designs. The loop antenna arrays were improved by using both a reflecting ground plane as well as an artificial magnetic conductor to increase the forward gain. The AMC created is capable of dual resonances that when combined with the slot antenna geometry reduced the system height beyond that of even the reflecting plate. The AMC design also showed that the challenge of fabricating small features can be overcome by using laser oblation technologies. The integration of the X-band array demonstrated that when unused aperture is available it can be exploited to increase the overall utility of the system.

Future efforts surrounding this work include the design of an AMC with increased bandwidth at lower frequency and its integration with the tri-band technology to maximize gain of the loop elements. These exercises were beyond the scope of this dissertation since greater specificity and funds would be needed prior to design.

LIST OF REFERENCES

1. F-W. Yao and S-S. Zhong, “Broadband and high-gain microstrip slot antenna,” *Microw. Opt.Technol. Lett*, vol. 48, no. 11, pp. 2210-2212, Nov. 2006.
2. T. G. Ma and S. K. Jeng, “Planar miniature tapered-slot-fed annular slot antennas for ultra-wideband radios,” *IEEE Trans. Antennas Propag*., vol. 53, pp. 1194-1202, Mar. 2005.
3. T.-Y. Yun, C. Wang, P. Zepeda, C. T. Rodenbeck, M. R. Coutant, M. Li, and K. Chang, “A 1-21 GHz low-cost, multi-frequency and full-duplex phased array antenna system,” *IEEE Trans. Antennas Propag*., vol. 50, no. 5, pp. 641-650, May 2002.
4. X. Qu, S.S. Zhong, Y.M. Zhang, and W. Wang, “Design of an S/X dual-band dual-polarised microstrip antenna array for SAR applications,” *IET Microw. Antennas Propag.*, vol. 1, no. 2, pp. 513-517, April 2007.
5. R. L. Li , K. Naishadham , T. Wu, L.Yang, and M. M. Tentzeris, “Interleaved dual-band printed antenna element for phased array applications,” in *Proceedings Antenna Applications Symposium*, Allerton Park, IL, pp. 406-417, Sept. 2009.
6. R. Hasse, K. Naishadham, W. Hunsicker, M. M. Tentzeris, and T. Wu, “Full Wave analysis of a dual-frequency printed slot antenna with microstrip feed,” 2010 *IEEE International Symposium on Antennas and Propagation*, Toronto, Ontario, Canada, 2010.
7. W. Hunsicker, K. Naishadham, and R. Hasse, "Integration of an X-band microstrip patch array and beamformer for a multifunction antenna array," *Phased Array Systems and Technology (ARRAY), 2010 IEEE International Symposium on* , pp. 898-905, 12-15 Oct. 2010
8. D. Sievenpiper, Z. Lijun, R. F. J. Broas, N. G. Alexopolous, and E. Yablonovitch, “High-impedance electromagnetic surfaces with a forbidden frequency band," *IEEE Transactions on Microwave Theory and Techniques*, vol. 47, no. 11, pp. 2059-2074, 1999.

9. D. Sievenpiper, “High-impedance electromagnetic surfaces," Ph.D. Dissertation, Department of Electrical Engineering, University of California at Los Angeles, CA, 1999.
10. F. Yang and Y. Rahmat-Samii, “Refection phase characterizations of the EBG ground plane for low profile wire antenna applications," *IEEE Transactions on Antennas and Propagation*, vol. 51, no. 10, pp. 2691-2703, 2003.
11. R. E. Collin and F. J. Zucker, “*Antenna Theory- Part 1,*” pp. 560-563, McGraw-Hill Book Company, 1969.
12. W. L. Stutzman and G. A. Thiele, *Antenna Theory and Design*, 2e, pp. 205-210, John Wiley & Sons, 1998.
13. NSI 2000 Operation Manual, Torrance, CA, Nearfield Systems Inc.
14. Ansys High Frequency Structure Simulator v.14, 2013
15. D. Sievenpiper, “A Review of the Theory, Fabrication, and Applications of High-Impedance Ground Planes”, in *Metamaterials: Physics and Engineering Explorations*, edited by Nader Engheta and Richard Ziolkowski, pp. 287-311,Wiley, 2006
16. L. Yang, M. Fan, and Z. Feng, "A Spiral Electromagnetic Bandgap (EBG) Structure and its Application in Microstrip Antenna Arrays," *Proc. APMC*, vol. 5, pp. 418-422, China, 2005.
17. L.Brillouin, *Wave Propagation in Periodic Structures*, McGraw-Hill, New York, 1946.
18. S. Clavijo, R. E. Diaz, and W. E. McKinzie,"Design methodology for Sievenpiper high-impedance surfaces: an artificial magnetic conductor for positive gain electrically small antennas," *Antennas and Propagation, IEEE Transactions on* , vol. 51, no. 10, pp. 2678- 2690, Oct. 2003.
19. J. L. Hobdell, "Optimization of Interdigital Capacitors," *Microwave Theory and Techniques, IEEE Transactions on* , vol. 27, no. 9, pp. 788-791, Sep. 1979.
20. X. Y. She and Y. L. Chow, "Interdigital microstrip capacitor as a four-port network," *Microwaves, Antennas and Propagation, IEE Proceedings H* , vol. 133, no. 3, pp. 191-197, June 1986.

21. Y. Kim, F. Yang, and A. Z. Elsherbeni, "Compact artificial magnetic conductor designs using planar square spiral geometries," *Progress In Electromagnetics Research*, vol. 77, pp. 43-54, 2007.
22. J. Du, C. Y. Wu, W. J. Zhu, and Q. Liu, "Ultrathin low cost EBG structure for insulating UHF RFID tag from metal objects," *Signal Processing, Communications and Computing (ICSPCC), 2011 IEEE International Conference on* , vol. 1, no. 4, pp. 14-16, Sept. 2011.
23. http://www.RogersCorp.com
24. http://www.LPKFUSA.com
25. R. Bancroft, "*Microstrip and Printed Antenna Design,"* pp. 28-37, Noble Publishing, 2004.

VITA

WALKER F. HUNSICKER

EDUCATION

Ph.D., Engineering Science, University of Mississippi, to be awarded May 2015
Concentration: Electromagnetics
Dissertation: Analysis and Design of Low Profile Multiband Multifunctional Antenna Arrays

M.S., Engineering Science, University of Mississippi, December 2007
Concentration: Electromagnetics
Dissertation: An Analysis and Design of Wideband Vivaldi Antennas

B.S., Electrical Engineering, University of Mississippi, May 2000

TEACHING EXPERIENCE

Instructor, 2008
University of Tennessee at Chattanooga National Center for Computational Engineering(SimCenter)
Course: Theory of Fields

PROFESSIONAL EXPERIENCE

Senior Research Engineer, 2009-2014
Georgia Tech Research Institute (GTRI) - Sensors and Electromagnetic Applications Laboratory Atlanta, GA

Senior Engineer, 2004-2009
Radiance Technologies Inc. Oxford, MS

Electronics Engineering (Intern), 2002
Naval Air Warfare Center Aircraft Division – 4.5.5 RF Sensor Systems
Patuxent River Naval Air Station, MD

PUBLICATIONS and PRESENTATIONS

W. Hunsicker, "EM Effects Study Final Report," Final Technical Report, GTRI, 2011.

W. Hunsicker, K. Naishadham, and R. Hasse, "Integration of an X-band microstrip patch array and beamformer for a multifunction antenna array," *Phased Array Systems and Technology (ARRAY), 2010 IEEE International Symposium on*, pg. 898-905, 2010.

Co-presented a talk on "Multifunctional Antenna Arrays" at IDGA Military Antennas Conference 2010.

W. Hunsicker, "SBIR - Dielectrically Enhanced Resonator Array Final Report," Radiance Technologies Inc., 2007.

W. Hunsicker, "An Analysis and Design of Wideband Vivaldi Antennas," Master's Thesis, University of Mississippi, 2007.